Development of a dynamic multi-bed Pressure Swing Adsorption process for high purity hydrogen production from Coke Oven Gas

A mathematical modeling approach

Balan Ramani

Master of Science Thesis

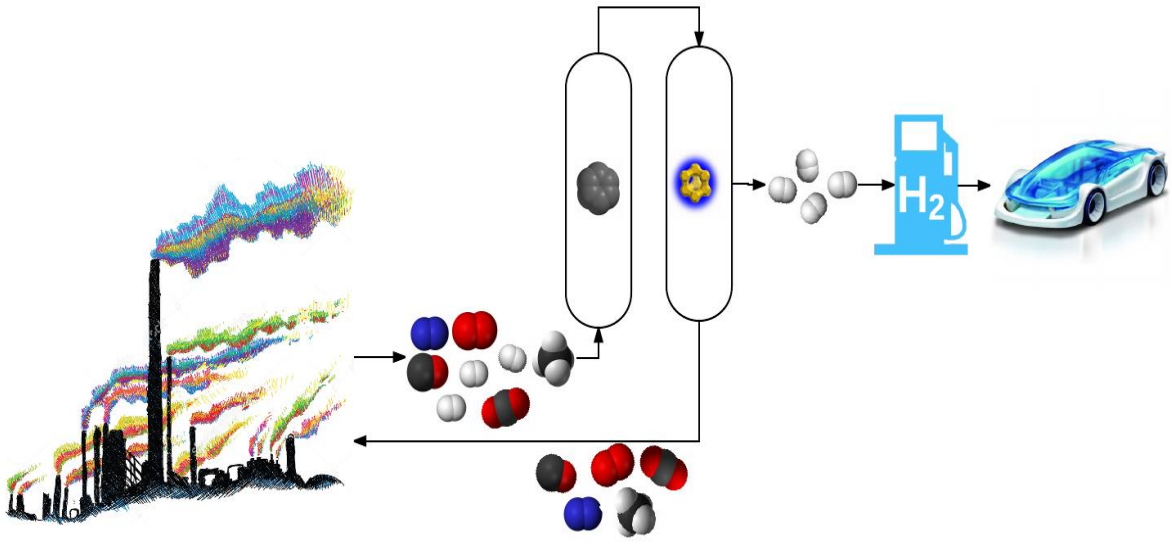

TU Delft

Process & Energy

TATA STEEL

Development of a dynamic multi-bed Pressure Swing Adsorption process for high purity hydrogen production from Coke Oven Gas

A mathematical modeling approach

By

Balan Ramani

in partial fulfilment of the requirements for the degree of

Master of Science
in Mechanical Engineering

at the Delft University of Technology,
to be defended publicly on Tuesday August 30, 2016 at 1:00 PM.

Supervisors:	Prof. dr. W. Buijs,	TU Delft
	drs. ir. G. Jägers,	Tata Steel
Thesis committee:	Prof. dr. B.J Boersma,	TU Delft
	Prof. dr. W. Buijs,	TU Delft
	Prof. dr. F. Mulder,	TU Delft
	drs. ir. G. Jägers,	Tata Steel

Abstract

Coal is certain to play a major role in the world's energy future due to its low cost and widespread distribution around the world. At the same time, being the largest contributor to global CO_2 emissions from energy use, coal faces significant environmental challenges in terms of air pollution and global warming. The study focuses on developing a pressure swing adsorption (PSA) technology that will allow for continued operation of coal, while improving its energy-efficiency by better utilisation of its by-product coke oven gas from steel industries. A generic, fast and robust simulation tool for simulating a variety of pressure swing adsorption processes considering both equilibrium and kinetic effects using a detailed non-isothermal and non-isobaric model is developed using MATLAB in the study. The adsorption equilibrium data required for the model are first calculated from experimental results using the non-linear regression data fitting method. Activated carbon and zeolite LiX adsorbents are modelled using Spartan molecular modeling software and simulated for estimation of the adsorption equilibrium data. The isosteric heat of adsorption values estimated from the simulation of molecular models matched well with the values calculated from experimental results showing the potential of molecular modeling tool in estimating the adsorption equilibrium data in a simple, fast and cost-effective way. A series of rigorous parametric studies and breakthrough tests are performed using the developed mathematical model for better understanding of the effects of different factors on the PSA process performance. With the better understanding obtained from the above-mentioned parametric studies, the model is optimised by performing several simulation tests to achieve the best possible process performance in terms of purity and recovery of the H_2 product, productivity of the adsorbents and energy consumption for compression of gases. The optimised 14-step multi-bed PSA cycle developed in this study allows for an improved energy efficiency of coal usage by better utilisation of its by-product coke oven gas by converting it into valuable high purity (>99.999%) hydrogen fuel for mobility applications with a recovery of over 75%.

Keywords: coal, steel industry, coke oven gas, gas separation, hydrogen purification, adsorption equilibrium, heat of adsorption, molecular modeling, activated carbon, zeolite, dynamic mathematical modeling, pressure swing adsorption, breakthrough curves, parameter studies, model optimisation.

Acknowledgement

This research work would not have happened without the support from my supervisors Prof. dr. Wim Buijs and drs. ir. Gerard Jägers who allowed me to frame my own thesis research. The research was exceptionally challenging not only due to the complexity of the subject but also due to the work on computational surface chemistry as a mechanical engineer. But with the vast knowledge and experience of Prof. Buijs on molecular chemistry, he taught me the concepts needed for my research in a simple and understandable way from a mechanical engineer's perspective, thereby making me comfortable and not feeling the complexity of the work involved in molecular modeling.

I would like to thank Gerard for all the constant support he offered during my period of work at Tata Steel besides his busy work schedule. He always showed great willingness to help me whenever I faced an issue with my work, whether it be purchasing a new software like Spartan molecular modeling tool or a high performance computer required for my research or in finding the right contact person within the company to solve my problem. Also working with Gerard, I had the opportunity to attend many meetings related to my research work and interact with people from high-level positions of different companies which helped to develop my professional skills.

Next, I would like to express my gratitude to Dr. Jurriaan Boon who was my previous research internship supervisor at the Energy Research Centre of the Netherlands (ECN), Petten. It was from him I actually gained the passion and preliminary knowledge for developing complex mathematical models as for the dynamic pressure swing adsorption process developed in this study.

Of course a big thanks to all my work colleagues at the Energy Efficiency department of Tata Steel for their support and for all the interesting conversations I had with them during the research period.

Finally I would like to thank my family and friends for encouraging and motivating me during the hard times of research work.

Balan Ramani

Delft, August 2016

Contents

List of Figures

List of Tables

Nomenclature

A	Cross-sectional area of the column [m^2]
c	Fluid phase concentration [$mol.m^{-3}$]
C_{pg}	Specific heat capacity of gas phase [$J.mol^{-1}.K^{-1}$]
C_{ps}	Specific heat capacity of adsorbent [$J.kg^{-1}.K^{-1}$]
C_{pw}	Specific heat capacity of wall [$J.kg^{-1}.K^{-1}$]
D_{ax}	Axial mass dispersion co-efficient [$m^2.s^{-1}$]
D_m	Molecular diffusivity [$m^2.s^{-1}$]
D_k	Knudsen diffusivity [$m^2.s^{-1}$]
D_e	Effective diffusivity [$m^2.s^{-1}$]
E	Compressor energy consumption [J]
f	State variable [-]
f_m	Flow rate [$mol.s^{-1}$]
h	Heat transfer co-efficient [$J.m^{-2}.K^{-1}.s^{-1}$]
H	Enthalpy [$kJ.mol^{-1}$]
k	Mass transfer co-efficient [s^{-1}]
k_B	Boltzmann constant [$J.K^{-1}$]
L	Column length [m]
MW	Molecular weight [$kg.mol^{-1}$]
N	Number of discretization volumes
P	Pressure [Pa]
Pr	Prandtl number
q	Solid phase concentration [$mol.m^{-3}$]
r	Column radius [m]
r_p	Particle radius [m]
r_{pore}	Pore radius [m]
R	Universal gas constant (=8.314) [$J.mol^{-1}.K^{-1}$]
Re	Reynolds number
S	Entropy [$kJ.mol^{-1}K^{-1}$]
Sc	Schmidt number
t	Time [s]
T	Temperature [K]
v	Interstitial velocity [$m.s^{-1}$]
V	Volume of cell [m^3]
y	Gas phase composition [-]
z	Axial co-ordinate [m]

Greek symbols

ε	Bed porosity [-]
ε_p	Particle porosity [-]
ρ_g	Gas phase density [mol.m^{-3}]
ρ_s	Adsorbent density [kg.m^{-3}]
ρ_w	Wall density [kg.m^{-3}]
λ_{ax}	Axial thermal dispersion co-efficient [J.m^{-1}.K^{-1}.s^{-1}]
λ_g	Thermal conductivity of gas [J.m^{-1}.K^{-1}.s^{-1}]
λ_w	Thermal conductivity of wall [J.m^{-1}.K^{-1}.s^{-1}]
μ	Viscosity of fluid [Pa.s]
σ, ξ	Lennard Jones potential energy function [-]
Ω	Collision integral [-]
τ'	Tortuosity [-]
δ	small change (=10^{-10})
τ	Dimensionless time [-]
γ	Adiabatic constant [-]
η	Compressor efficiency [-]

Acronyms

13X	Zeolite 13X
AC	Activated carbon
BEV	Battery Electric Vehicle
Btu	British thermal unit
CCS	Carbon Capture and Storage
CCU	Carbon Capture and Utilisation
COG	Coke oven gas
CSS	Cyclic steady state
FAU	Faujasite
FCEV	Fuel Cell Electric Vehicle
GHG	Greenhouse gases
IZA	International Zeolite Association
LDF	Linear driving force
MMFF	Merck Molecular Force Field
OECD	Organisation for Economic Co-operation and Development
PEM	Proton exchange membrane
PSA	Pressure Swing Adsorption
SMR	Steam Methane Reforming

Subscripts

0	Non-dimensional reference value
a	Ambient
acc	Accumulated
ads	Adsorption
BD	Blowdown
Evac	Evacuation
H	High
i	Component
in	Inside
I	Intermediate/Evacuation
j	Cell index
L	Low
out	Outside
PEQ	Pressure Equalisation
Rep	Repress
w	Wall

Superscripts

*	Equilibrium condition
¯	Dimensionless term

Chapter 1

Introduction

1.1 Coal usage and its future role

Coal is a crucial fuel in this uncertain world of future constraint on CO_2 emissions. Coal is abundant and relatively cheap — $1–2 per million Btu, compared to $6–12 per million Btu for natural gas and oil [1]. Coal is often the fuel of choice for electricity generation and perhaps for extensive synthetic liquids production in the future in many parts of the world. Its low cost and wide availability make it especially attractive in major developing economies for meeting their pressing energy needs.

Table 1.1 World Consumption of Primary Energy and Coal (1990-2030) [1]

	Total Primary Energy (Quadrillion Btu)			Total Coal (Million Short Tons)		
	OECD	**Non-OECD**	**Total**	**OECD**	**Non-OECD**	**Total**
1990	197	150	347	2550	2720	5270
2003	234	186	421	2480	2960	5440
2010	256	254	510	2680	4280	6960
2015	270	294	563	2770	5020	7790
2020	282	332	613	2940	5700	8640
2025	295	371	665	3180	6380	9560
2030	309	413	722	3440	7120	10560

Source: DOE/EIA IEO (2006): Tables A1 & A6

On the other hand, coal faces significant environmental challenges in terms of air pollution and global warming. Indeed coal is the largest contributor to global CO_2 emissions from energy use (46%) as seen in **Figure 1.1**, and its share is projected to increase [2].

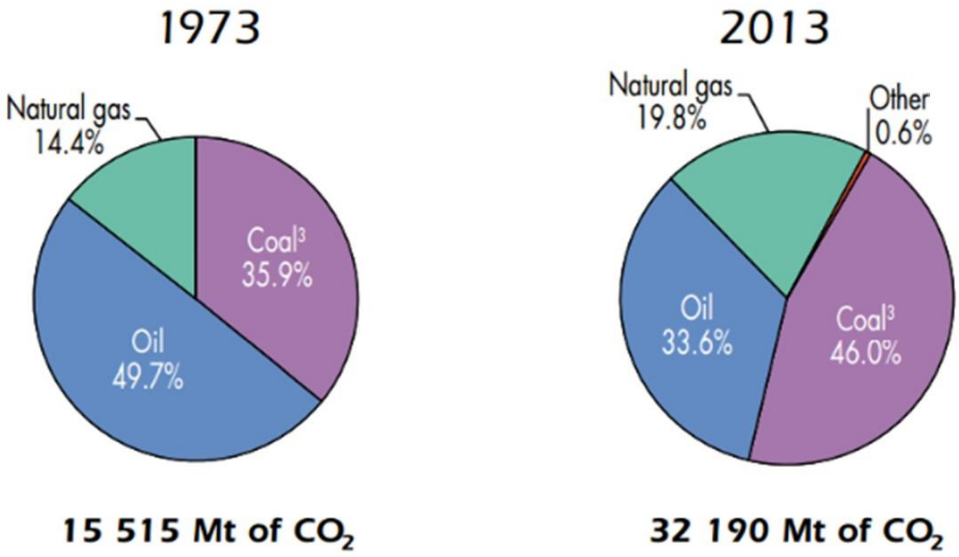

Figure 1.1 1973 and 2013 fuel shares of CO_2 emissions from fuel combustion [2]

The solution to overcome global warming and environmental pollution issues lies not in a single technology but in more effective use of existing fuels and technologies, as well as wider adoption of alternative energy sources.

There are five broad options [1] arranged in the order of their significance in reducing carbon emissions from the combustion of fossil fuels, which is the major contributor to the anthropogenic greenhouse effect:

1. Increased use of renewable energy such as wind, solar and biomass;
2. Expanded electricity production from nuclear energy;
3. Switching to less carbon-intensive fossil fuels; and
4. Improvements in the efficiency of energy use
5. Continued combustion of fossil fuels, especially coal, combined with CO_2 capture and utilization (CCU).

The current techno-economic status of renewable energy options, the large number of fossil fuel based power plants in operation and the availability of cheap and abundant coal make large scale deployment of renewable energy options prohibitively expensive in the near future.

Next to renewable energy, nuclear energy is considered to be one of the most environmentally friendly source of energy as it produces fewer greenhouse gases as opposed to traditional fossil fuel sources. But the disposal of radioactive waste and the safety of operation is still a big concern with nuclear energy use.

Increased use of less carbon intensive fuels like natural gas is considered to be the next option. But the natural gas and oil resources are limited and are not evenly distributed around the world. Also, the natural gas and oil reserves are expected to deplete after 2042 as opposed to coal reserves which are expected to last atleast for the next 100 years to come [3].

Therefore, coal is certain to play a major role in the world's energy future for two reasons [1]. First, it is the lowest-cost fossil source for base-load electricity generation. And second, as shown in **Figure 1.2**, in contrast to oil and natural gas, coal resources are widely distributed around the world spreading between developed and developing countries.

Hence, focus should be on developing technologies that will allow continued operation of fossil fuels like coal, while improving their energy efficiency by better utilization of their by-products and on reducing their environmental impact by CO_2 capture and utilization.

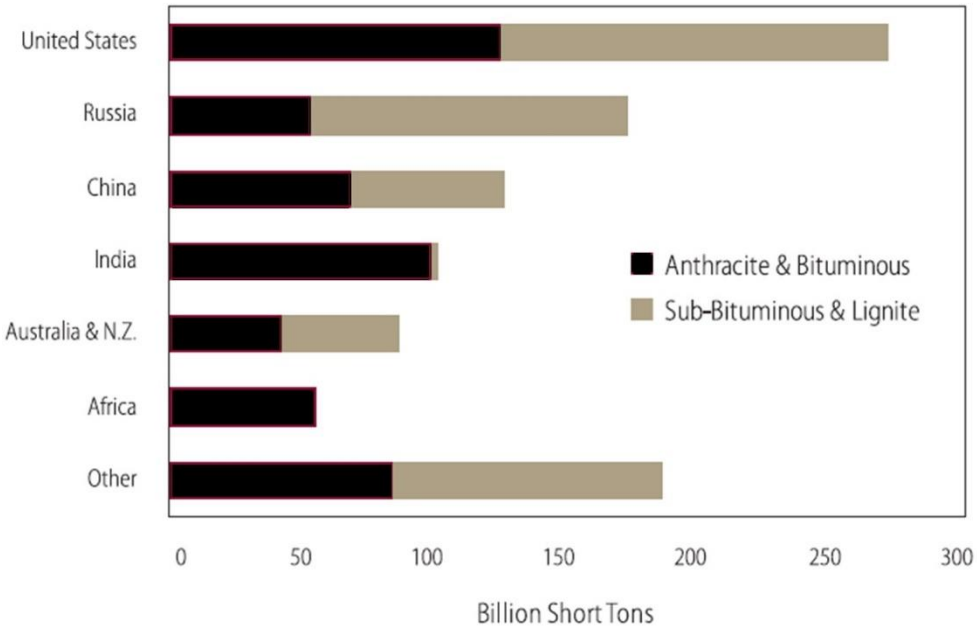

Figure 1.2 Global recoverable Coal Reserves [1]

1.2 Role of coal in steel industries

Steel industries are the largest energy consuming manufacturing sector in the world and coal being the cheapest form of fossil fuel, is their main source of energy. Hence, the CO_2 emissions associated with the steel industries are also very high and accounts for about 5-7% of the total anthropogenic CO_2 emissions [4]. Considering the fact that steel production is expected to increase especially in the developing countries, a significant increase in coal consumption and as well as CO_2 emissions are also expected to follow up. The steel industries have been committed to sustainability since 1960's and now the steel manufacturing processes in many developed countries have reached considerably high levels of efficiency in terms of carbon use [4]. Global warming concerns have created the urge to look for alternate ways to improve energy efficiency and reduce greenhouse gases (GHG) emissions of the steel industries.

1.2.1 Coke making process

Coal pyrolysis is a process in which coal is thermodynamically decomposed by heat in an atmosphere without oxygen. This process occurs at 1273-1373 K in a coke oven battery. During coal pyrolysis, the volatile components leave the charcoal leaving carbon and ash behind. The resulting solid is referred to as coke and consists mainly of carbon matter. The purpose of this process is to purify the coal, to strengthen it so it will not fall apart in the blast furnace and to ensure it is porous enough for the blast furnace air to pass through it. The schematic overview of the coke making process is shown in **Figure 1.3**. The volatile components leaving the coke is the coke oven gas (COG).

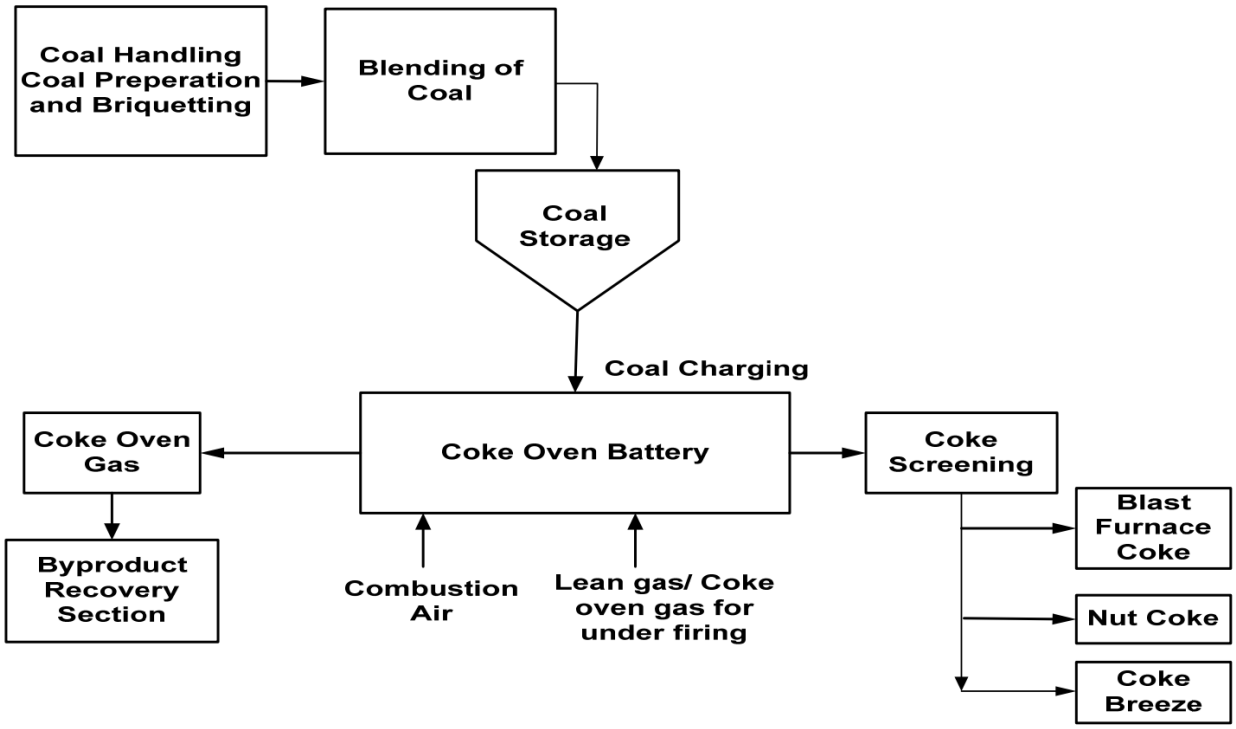

Figure 1.3 Schematic of coke making process [5]

1.2.2 Potential of Coke Oven Gas

Coke oven gas is a point of high interest to enhance energy efficiency and reduce greenhouse gases emissions of the steel industry. Blast furnace cannot operate without coke which implies coke oven gas production will continue to increase in the future with the increase in steel production.

Coke oven gas leaving the coke oven battery has a very complex composition. The gas is first cooled down to separate tar, then passed through a series of scrubbing units to remove NH_3, H_2S and BTX (Benzene, Toluene and Xylene). After the treatment process, the cleaned COG typically comprises of the following gas components: H_2 (~55-60%), CH_4 (~23-27%), CO (~5-8%), N_2 (~3-6%), CO_2 (<2%), O_2 (<1%) along with other hydrocarbons in small proportions [4].

COG has a caloric value of 18 MJ/m^3 approximately and accounts for 18% of the energy output of coke plant. COG is mainly used for its heating value in the internal operations of steel making process and in some cases (e.g. Tata Steel Ijmuiden) also for electricity production to meet internal power demands. The surplus gas is burnt off in torches and even in some cases directly emitted to the air [4], [6]. Current COG usage methods are energy inefficient and has a significant environmental impact in terms of large GHG emissions.

COG containing ~55-60% of H_2 is a high potential source of hydrogen which is regarded as a future clean energy source. In the future, centralized CO_2 emissions from the industries can be controlled using carbon capture technologies. But, it is difficult to control the decentralized CO_2 emissions from automobiles. Hence, the mobility system needs to adopt Battery Electric Vehicles (BEVs) or Fuel Cell Electric Vehicles (FCEVs) which do not rely on fossil fuels or biofuels and provide the long term prospect of truly zero-emission. FCEVs have shorter refuelling time and much longer driving range as compared to BEVs making them more attractive for long distance mobility applications. This emerging hydrogen mobility market might provide the opportunity for a possible new and efficient usage of COG.

1.2.3 Hydrogen Purity

High purity hydrogen needs to be separated from other components of coke oven gas before being used as fuel for FCEVs. The impurities level of product hydrogen for fuel cell applications are very strict. The maximum allowable level of impurities are shown in **Table 1.2**.

Table 1.2 Allowable impurities level (in ppm) in H_2 product [7]

Component	ISO/DIS 14687-2 specification (ppm)
Total hydrocarbons	2
Oxygen	5
Nitrogen	100
Carbon dioxide	2
Carbon monoxide	0.2
Total Sulphur compounds	0.004

1.2.4 Hydrogen Separation Technologies

Several gas treatment technologies exist and are already indispensable in many chemical industries. The sub-sections below provide a brief review of three main technologies – cryogenic distillation, absorption and membrane technology. The focus of this research work, adsorption process will be discussed in detail in the following section [8].

1.2.4.1 Cryogenic Distillation

Cryogenic distillation is the most common and widely used gas separation technique. It operates at low temperatures, below 150 ^{o}C which is the typical boiling point of gases. It differentiates itself from other technologies by having no need for a physical separating agent between different phases, thereby eliminating the regeneration step. It can produce high purity products but is energy intensive and requires high maintenance cost. Being a mature technology, development for cost reduction is limited. It is unsuitable for coke gas treatment since an enormous amount of energy is required to condense the coke gases [8].

1.2.4.2 Absorption

Absorption is the phenomenon in which mass transfer takes place between the gas phase and a non-volatile liquid phase. The equilibrium staged process offers numerous advantages. The design of its unit operation is simple and provides flexibility in continuous operation. But, the high capital cost of fresh solvent, substantial operating cost from its energy intensive regeneration steps as well as the large throughput of the solvent involved makes it unfavourable when compared with competing technologies. Several investigations are been directed towards finding more energy efficient ways of regenerating used solvents, process modifications and development of superior solvents [8].

1.2.4.3 Membrane Technology

It is a relatively new technology with huge potential for growth. Its advantages include simple modular design, ease of operation, long lifetime and continuous operation. The main difficulties faced in its development are the conflict between membrane selectivity and permeability, reliability issues caused by hydrocarbon condensation and also high capital costs involved in research and implementation. Large scale applications are still uncommon and mostly incorporated with absorbents or adsorbents to improve existing process. It is a poor candidate for hydrogen separation from coke gas which require very high product purity. This is due to the limitations in producing high purity products either permeate or non-permeate in a single stage; a multi-stage design would make the process economically not feasible due to increased operating cost from extra compression steps [8].

1.2.5 Adsorption

Adsorption together with chromatography and ion exchange form a unique set of separation techniques that are characterised as fluid-solid heterogeneous, unsteady state operations. Although the phenomenon was first scientifically recorded in the late 19th century, adsorption had only limited applications in air purification until the early 1960s. Development over the next 40 years have established adsorption as the leading process in the removal of toxins from wastewater and gas. The future goal of this technology would be to extend its capability for more types of separation processes and to economically compete with established techniques such as distillation and absorption [8].

1.2.5.1 Principle

Adsorption uses highly porous solids as the mass separating agent, generally in the form of a fixed bed. Some species are preferentially adsorbed onto the solid surface while the less strongly adsorbed species are allowed to pass through the column. The adsorbed species are called adsorbate while the porous solids are called adsorbents. Mass transfer from fluid to solid phase is generally equilibrium controlled; other adsorption mechanism is the kinetic effect which is usually less dominant. The equilibrium effect dictates that mass transfer is driven by the difference between the fluid concentration and solid loading. The kinetic effect depends on the difference in diffusion rates of different molecules [8].

1.2.5.2 Adsorbents

The state of adsorption technology arguably depends on that of adsorbents. Most adsorbents are manufactured (such as activated carbons), but a few, such as some zeolites, occur naturally. Each material has its own characteristics such as porosity, pore structure and nature of its adsorbing surfaces.

Pore sizes in adsorbents may be distributed throughout the solid. Pore sizes are classified generally into 3 ranges:

- Macropores have diameters in excess of 50 nm
- Mesopores have diameters in the range of 2 – 50 nm
- Micropores have diameters smaller than 2 nm

Many adsorbent materials, such as carbons, silica gels and alumina, are amorphous and contain complex networks of inter-connected micropores, mesopores and macropores. In contrast, pores in zeolite adsorbents have precise dimensions.

Activated Carbon: It is highly porous having a large surface area to volume ratio. Its non-polar or slightly polar surface allows it to strongly adsorb organic compounds. Regeneration of activated carbon requires less energy compared to other adsorbents due to the lower heat of adsorption. Heat of adsorption is the strength with which the adsorbate is bonded to the adsorbent.

Carbon Molecular Sieves (CMS): CMS are manufactured from the same starting material as activated carbon, but additional treatment with hydrocarbon cracking gives it unique properties

of tightly controlled and more uniform pore structure than that of activated carbon. Kinetic effects excludes larger molecules while surface interactions are similar to that of activated carbon. CMS are significantly more expensive than that of activated carbon due to the extra manufacturing step.

Zeolites: Zeolites are crystalline aluminosilicates whose pores have exact dimensions. Thus zeolites can be designed for separation based on kinetic effect allowing only certain shapes of molecules to diffuse through them although the equilibrium effect is more dominant in their current applications.

Silica gel: Silica gel is an amorphous solid made of colloidal silica (SiO_2). It is hydrophilic in nature and has a large surface area to volume ratio. Heat of adsorption of water on silica gel is low which helps during regeneration. It can be damaged by liquid water during gas separation.

Activated alumina: It has excellent water adsorption properties and is more durable than silica gel in the presence of liquid water. But, prolonged usage leads to contamination thereby reducing its adsorptive capacity [8].

1.2.5.3 Regeneration methods

One of the key feature for adsorption technology is the ability to regenerate the spent adsorbent quickly using as less purge (desorbent) as possible. Concepts such as thermal swing adsorption (TSA), pressure/vacuum swing adsorption (PSA/VSA) and simulated moving bed (SMB) are useful in optimising energy use and enhancing product purity [8]. SMB is currently limited to liquid separations.

TSA is the oldest and most developed adsorption technique. It works on the principle that the adsorptive capacity of adsorbents increase at low feed temperatures leading to adsorption and decrease at high temperatures resulting in desorption. However the cycle time of a typical TSA process may range from several hours for bulk separation to several days for purification process since the adsorbent beds cannot be heated and cooled quickly. Another problem associated with TSA process is the reduction in the capacity or lifetime of the adsorbent when it is subjected to repeated thermal cycling [8].

PSA/VSA processes work on the same principle that adsorption occurs at high pressure and regeneration occurs at low pressure. They are generally equilibrium controlled processes wherein different amount of adsorbate is adsorbed at different pressures during the cycle. Most of the PSA processes operate under adiabatic conditions where compressors provide the pressure required to achieve the separation. PSA can achieve high purity separation as compared to membrane technology. Activated carbon can be used with PSA for separation of toxins from the feed gas due to their high adsorptive capacity, fast kinetics and relative ease of regeneration. A PSA cycle can be very fast with a cycle time of generally few minutes. This leads to high productivity and small adsorbent beds reducing the capital cost. But, VSA generally has a long desorption step thereby reducing productivity. The design and operation of PSA cycles are very flexible allowing for quick adaptation to changes in feed composition and market demands [8].

1.2.6 Pressure Swing Adsorption (PSA) for H_2 Separation from COG

PSA technology is based on the physical binding of gas molecules to adsorbent surfaces. The binding force mainly depends on the nature of gas component, type of adsorbent material, partial pressure of the gas component in the mixture and operating temperature. The separation of gases is based on their difference in binding force to the adsorbent surface. Hydrogen being a highly volatile component with low polarity is weakly adsorbed as opposed to molecules such as CO, CO_2, N_2, CH_4 and other hydrocarbons present in coke oven gas as represented in **Figure 1.4**. Hence the impurities present in COG can be adsorbed, thereby recovering high purity hydrogen. Since no heating or cooling is required, PSA cycles are short and hence the duration of PSA process steps are generally in the range of minutes [9].

Figure 1.4 Qualitative ranking of the adsorption forces [9]

The great flexibility of PSA process is normally associated to the complexity of the process and is one of the major issues to introduce the technology in several fields of industry. On the other hand, the greater flexibility of the PSA process constitutes to its main advantage and is the reason why it has found applications in diverse fields.

One of the key research goals for pressure swing adsorption process is to improve its energy demand. Other ways to bring down operating costs are to develop adsorbents with high selectivity and better regeneration capabilities. Capital cost reduction can be achieved through more compact design of adsorption equipment. Hence, faster development of PSA technology for different applications can happen by having a good interaction between materials science and process engineering [10].

The main objectives of the study include:

- developing a generic simulation tool using MATLAB for simulating a variety of dynamic pressure swing adsorption processes considering both equilibrium and kinetic effects using a detailed non-isothermal and non-isobaric model
- calculating the adsorption equilibrium data required for the model from experimental results using non-linear regression data fitting method
- modeling and simulation of activated carbon and zeolite LiX adsorbents with different coke oven gas components using Spartan molecular modeling software for estimation of adsorption equilibrium data i.e. isosteric heat of adsorption values and comparison with values calculated from experimental results
- performing parametric studies and dynamic column breakthrough simulations using the developed mathematical model for better understanding of the effects of different factors on the performance of PSA process
- using the developed model for optimisation of a 14-step multi-bed PSA cycle for producing high purity (>99.999%) hydrogen fuel from coke oven gas with the best possible recovery for fuel cell vehicles (FCVs) application

Chapter 2

Adsorption Equilibria and Molecular Modeling

2.1 Selection of adsorbents

The industrial hydrogen purification by a PSA process involves adsorption bed made up of a series of layers of different adsorbents with different affinities for each impurity. Most of the literature studies about hydrogen production use activated carbon and zeolite 5A as adsorbents.

Hydrogen for fuel cell vehicles (FCVs) application require very high purity (>99.95 %) and should eliminate carbon monoxide (CO) even in ppm levels (<0.2 ppm) in order to avoid CO poisoning [11]. The higher competition of carbon dioxide with carbon monoxide in zeolite 5A adsorbent leads to a lower carbon monoxide adsorption capacity and therefore a higher carbon monoxide concentration in the hydrogen product. In order to overcome this problem, a better suitable adsorbent like zeolite 13X could be used in place of zeolite 5A.

But, the adsorption studies for hydrogen purification using zeolite 13X are less known than that of zeolite 5A. The literature study [12] shows that replacing zeolite 5A layer with zeolite 13X increases the hydrogen purity and recovery under the same operating conditions. Hence in this study, lithium-exchanged zeolite X (LiX) along with activated carbon are used as adsorbents for development of PSA process for hydrogen purification from coke oven gas.

2.2 Pre-Treatment of COG

The dry raw coke oven gas (COG) is a complex mixture containing numerous components, typically including

Table 2.1 Typical composition of raw dry COG [13]

Major Components	**Appx. Volume %**
Hydrogen (H_2)	48-55
Methane (CH_4)	28-30
Carbon monoxide (CO)	5.0-7.5
Carbon dioxide (CO_2)	1.5-2.5
Nitrogen (N_2)	1.0-3.0
Oxygen (O_2)	0-0.5
Minor Components	
High paraffins and unsaturated hydrocarbons	
Ammonia (NH_3)	
Hydrogen sulphide (H_2S)	
Carbonyl sulphide (COS)	
Hydrogen cyanide (HCN)	
Ammonium chloride	
Benzene, Toluene, Xylene, Naphthalene and other aromatics	
Tar components	

Of these, it is fine to feed the major components to the PSA system while the minor components should be removed before input to PSA. In general, the presence of these minor components in the COG feed affect the performance of the PSA process as they are strongly adsorbed to the adsorbent surface making it difficult to remove them from the adsorption bed.

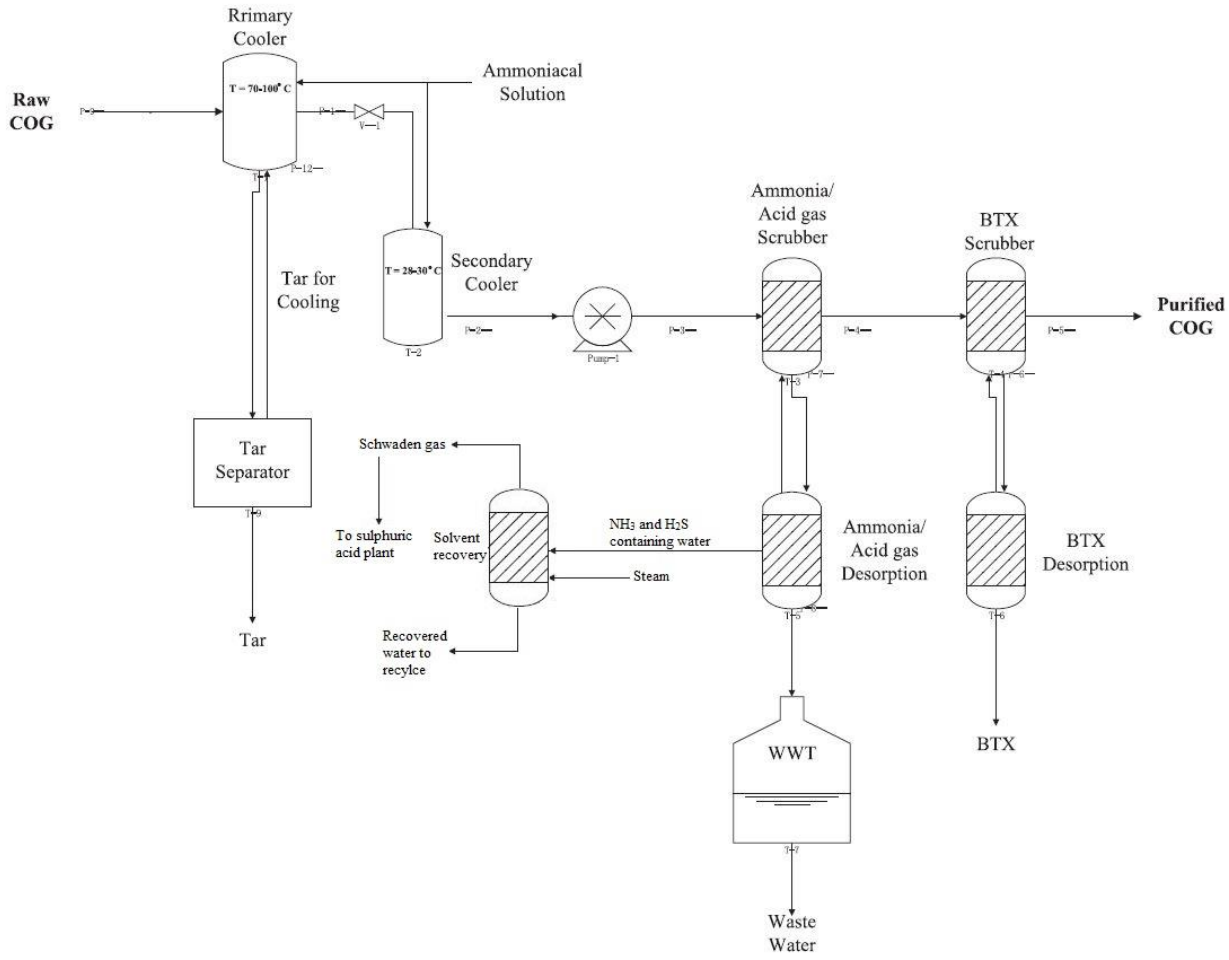

Figure 2.1 Schematic diagram of a typical COG treatment process modified from [6]

A conventional coke treatment process is shown in **Figure 2.1**. Water and tar contents are transferred into a crude tar recovery unit and then COG is cooled to around 27 ^{o}C. NH_3 and H_2S are scrubbed in a scrubbing unit. Benzene, Toluene, Xylene (BTX) is removed and recovered for further utilization. The water used in scrubbing unit are recycled before being re-pumped into the scrubber. Finally, NH_3 and H_2S mixture from the scrubbing unit commonly known as Schwaden gas is inputted as feed to the sulphuric acid plant. The resulting coke oven gas after the treatment process is free from minor components and contains only the major components H_2, CH_4, CO, CO_2, N_2 and O_2.

In case any minor components are still present in trace amount in the COG even after the treatment process, an additional adsorption column is placed before the actual PSA installation, in order to ensure complete removal of minor components from COG before being fed to the H_2 sequestration PSA system.

2.3 Adsorption Equilibrium model

For the adsorption of pure gases, various single component models have been proposed to describe the adsorption loadings at different pressures and temperatures. Langmuir-Freundlich isotherm model is widely used to describe the physical adsorption of gases. The model is based on the kinetic principle that the rate of adsorption is equal to the rate of desorption from the surface. The mathematical form [14] of the isotherm model is

$$q^* = \frac{q_{sat}\, b\, P}{1 + b\, P} \tag{2.1}$$

where

q^* -adsorbed phase equilibrium concentration of gas species, mol kg^{-1}

q_{sat} -saturation limit of adsorbed phase concentration of gas species, mol kg^{-1}

b -adsorption equilibrium constant, bar^{-1}

P -pressure, bar

Experimental adsorption isotherm data (q vs P) for pure gas species measured at different isotherm temperatures were taken from literature [15]. By performing non-linear regression analysis using MATLAB, the experimental data was fitted with the isotherm model equation to obtain the values of q_{sat} and b for each of the isotherm. For a useful description of the adsorption equilibrium data at different temperatures, it is necessary to have an isotherm model that is temperature dependent. The temperature dependence of the isotherm model for the equilibrium constant b may take the form[16],

$$b = b_0 \exp\left(\frac{-\Delta H}{RT}\right) \tag{2.2}$$

where

b_0 -pre-exponential factor, $\left(= f\left(\frac{\Delta S}{R}\right)\right)$ bar^{-1}

R -universal gas constant, (=8.314) J mol^{-1} K^{-1}

ΔH -enthalpy change on adsorption, J mol^{-1}

ΔS -entropy change on adsorption, J mol^{-1} K^{-1}

T -temperature, K

Inorder to find the values of ΔH and b_0, equation (2.2) is rewritten as a straight line equation of the form $y = mx + c$,

$$\ln b = \left(\frac{-\Delta H}{R}\right)\frac{1}{T} + \ln b_0 \quad (2.3)$$

where

x -independent variable, $\left(= \frac{1}{T}\right)$

y -dependent variable, $(= \ln b)$

m -slope, $\left(= \frac{-\Delta H}{R}\right)$

c -intercept, $(= \ln b_0)$

Van't Hoff graphs are plotted between $\ln b$ and $\frac{1}{T}$ with two isotherm values for each of the pure gas species. From the slope and intercept of the plot, the values of ΔH and b_0 are calculated respectively. The resulting values of adsorption isotherm data for activated carbon (AC) and zeolite LiX are summarised in **Table 2.2** and **Table 2.3** respectively.

Table 2.2 Adsorption isotherm data for AC

Species	q_{sat} (mol kg^{-1})	b_0 (bar^{-1})	ΔH (kJ mol^{-1})
H_2	1.97	0.00872	-2.63
CH_4	4.47	0.00024	-17.74
CO	3.45	0.00075	-13.28
CO_2	6.85	0.00056	-17.09
N_2	3.44	0.00070	-12.73
O_2	4.68	0.00071	-11.83

Table 2.3 Adsorption isotherm data for LiX

Species	q_{sat} (mol kg^{-1})	b_0 (bar^{-1})	ΔH (kJ mol^{-1})
H_2	0.70	0.01382	-3.56
CH_4	3.21	0.00080	-14.84
CO	2.81	0.01050	-11.81
CO_2	5.13	0.00010	-28.49
N_2	2.39	0.00038	-17.14
O_2	5.74	0.00055	-8.94

Now with the values of q_{sat}, b_0 and ΔH estimated, we have a temperature dependent form of the isotherm model.

For the adsorption of multicomponent gas mixtures, the single component models can be extended to include the influence of other components on the adsorption behaviour of each individual component [16] with the possibilities of having competitive or non-competitive adsorption with/without the dissociation of gases (chemisorption). The total adsorption capacity includes the combined effects of competitive adsorption or non-competitive adsorption and dissociation of gases. Since the focus is on physisorption, the dissociation of gases i.e. chemisorption effects are not considered. In general, each adsorption site can hold at most one molecule of gas species. Hence the different gas components present in the feed compete for the same site of adsorption. The adsorption capacity of component i in a mixture of N components is thus determined via the following competitive adsorption equation:

$$q_i^* = \frac{q_{sat_i}\, b_i\, P_i}{1+\sum_{j=1}^{N} b_j\, P_j} \tag{2.4}$$

An adsorption equilibrium model is made using the above described extended Langmuir-Freundlich isotherm model to test the adsorptive capacity of coke oven gas (COG) components on different adsorbents. The operating conditions and composition of the COG feed to PSA system are summarised in **Table 2.4** and **Table 2.5** respectively.

Table 2.4 Operating conditions of COG feed

Pressure P (bar)	1
Temperature T (K)	298.15
Flow rate F_m (mol s^{-1})	160

Table 2.5 Volumetric composition of COG feed

H_2	0.6429
CH_4	0.2573
CO	0.0586
CO_2	0.0131
N_2	0.0259
O_2	0.0021

The adsorption isotherms for COG components on activation carbon and zeolite LiX adsorbents as shown in **Figure 2.2** and **Figure 2.3** respectively. It can be seen that activated carbon has a favourable isotherm for CH_4 while Zeolite LiX has a favourable isotherm for CO_2 over other components.

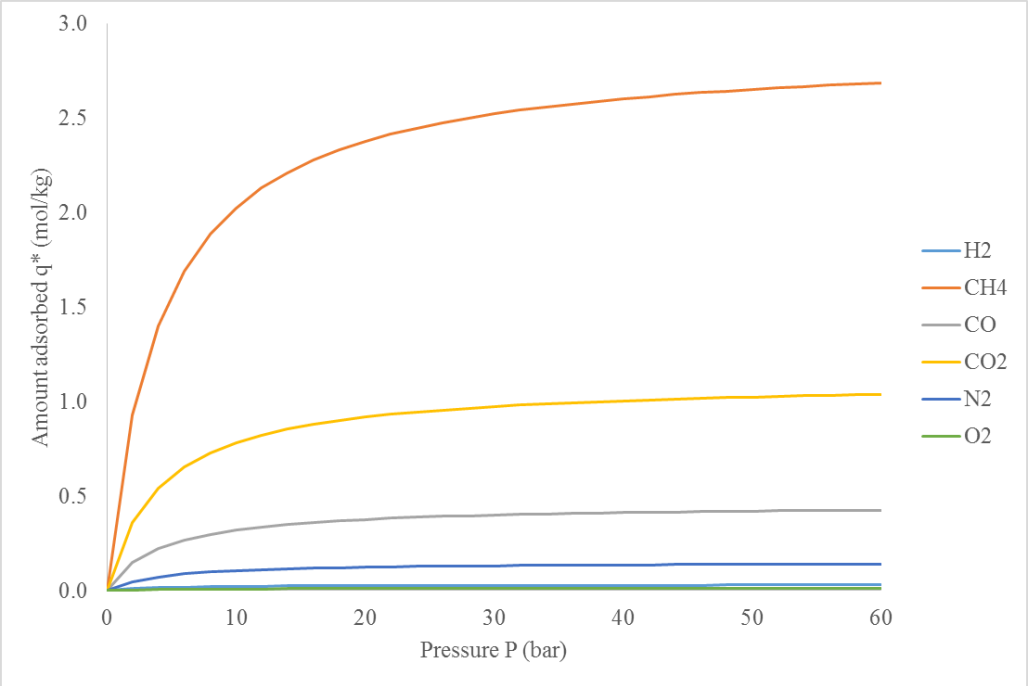

Figure 2.2 Adsorption isotherm of COG components on AC

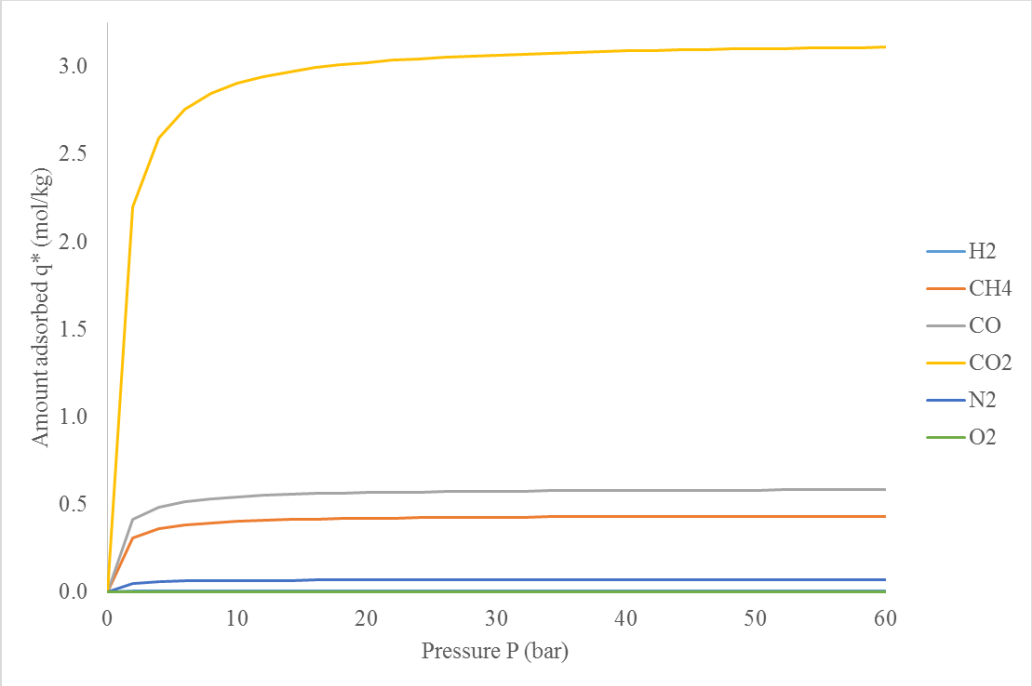

Figure 2.3 Adsorption isotherm of COG components on Zeolite LiX

From the adsorption isotherms, the working capacity of the COG components on the adsorbent between the operating pressure and thereby the selectivity of COG impurities over H_2 could be found out. The working capacity and selectivity are given by

$$\omega_i = q^*_{HP,i} - q^*_{LP,i} \quad (2.5)$$

$$\chi_{i/j} = \omega_i/\omega_j \quad (2.6)$$

where

ω_i -working capacity of gas component i on adsorbent, mol.kg^{-1}

$q^*_{HP,i}$-adsorbed phase equilibrium concentration of gas component i at high pressure, mol kg^{-1}

$q^*_{LP,i}$-adsorbed phase equilibrium concentration of gas component i at low pressure, mol kg^{-1}

$\chi_{i/j}$ -selectivity of gas component i over component j on adsorbent

The working capacity and selectivity results are shown in **Table 2.6** and **Table 2.7**.

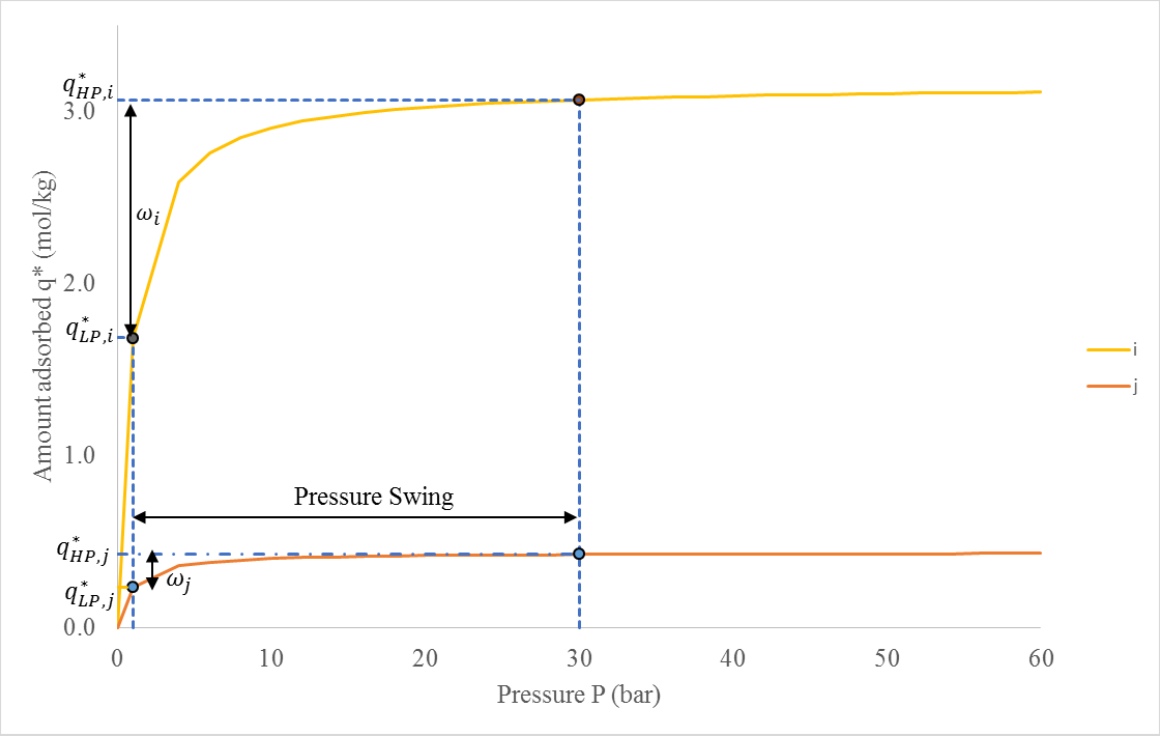

Figure 2.4 Working capacity and selectivity of gas components between the operating pressures

Table 2.6 Working capacity in mol kg-1 of COG components

Component	AC	LiX
H_2	0.02	0.002
CH_4	1.96	0.19
CO	0.31	0.26
CO_2	0.76	1.38
N_2	0.10	0.03
O_2	0.009	0.0004

Table 2.7 Selectivity of COG impurities over H_2

Component	AC	LiX
CH_4	90	81
CO	14	109
CO_2	35	582
N_2	5	13
O_2	0.4	0.2

It can be clearly seen from **Table 2.6** that the working capacity of CH_4 and CO_2 are higher than other gas components for AC and LiX adsorbents respectively.

The selectivity of most of the COG components as shown in **Table 2.7** are much higher than that of H_2 thereby aiding separation of high purity H_2 from COG. But for both adsorbents, the selectivity of O_2 is lower than that of H_2 hindering their separation and thereby affecting H_2 purity.

In these types of cases where equilibrium based separation becomes ineffective, kinetic based separation plays an important role to aid separation of the gases. The diffusivity (D) is inversely proportional to the square root of the molecular weight (MW) of the gas species as explained in equations (3.14) and (3.15) of section 3.2. Since, the molecular weight of O_2 molecules (32 g/mol) are larger than that of H_2 molecules (2 g/mol), the diffusion of O_2 (D_{O_2}) through the adsorption bed is much slower than that of H_2 (D_{H_2}) thereby resulting in separation of the gases.

$$D_{O_2} \sim \frac{1}{4} D_{H_2}$$

Hence, both equilibrium and kinetic effects should be properly accounted in the development of the PSA process for high purity hydrogen sequestration from coke oven gas which will be discussed in detail in the following chapter.

2.4 Molecular modeling

Despite the growth of industrial applications of the PSA processes, the design of commercial units and their optimization still requires an important experimental effort to find the adsorption equilibrium data. This information must be incorporated into the mathematical model to design and optimize the process. Fundamental studies about the adsorption of different gas species on different adsorbent materials are still scarce in the literature for industrial property protection reasons [15]. A molecular modeling approach to calculate these adsorption equilibrium data without experimentation could solve this problem and save a lot of time, energy and cost.

Recent development in molecular modeling software makes it easy to do sophisticated computations for a variety of applications. One such case is its application for surface chemistry which have challenges with computations because of the large number of atoms required in the model as well as the complex interactions involved [17].

The purpose of this study is to explore whether the Molecular Mechanics –Merck Molecular Force Field (MMFF) method in the Spartan molecular modeling software [18] could be used to accurately predict the adsorption data of various gas components on different adsorbents. It should be considered that the MMFF method is effective only with physical interaction phenomena like gas physisorption processes and for chemisorption processes, quantum mechanics and sometimes molecular dynamics methods are required. The various possibilities of MMFF molecular mechanics method is explained in appendix section A.2. Merck Molecular Force Field (MMFF) In this study we are especially interested with the prediction of heat of adsorption of different coke oven gas components on activated carbon and zeolite LiX adsorbents.

Total energies can be used to calculate the heat of adsorption according to equation (2.7).

$$\Delta H_{adsorption} = E_{adsorbent+adsorbate} - (E_{adsorbent} + E_{adsorbate}) \quad (2.7)$$

where

$\Delta H_{adsorption}$ -Isosteric heat of adsorption, kJ mol^{-1}

$E_{adsorbent}$ -Energy of adsorbent, kJ mol^{-1}

$E_{adsorbate}$ -Energy of adsorbate, kJ mol^{-1}

$E_{adsorbent+adsorbate}$ -Combined energy of adsorbent and adsorbate, kJ mol^{-1}

A negative ΔH indicates an exothermic (thermodynamically favourable) process, while a positive ΔH indicates an endothermic (thermodynamically unfavourable) process [19].

2.4.1 Modeling of Activated Carbon adsorbent

Activated Carbon (AC) is the most widely used sorbent. Its manufacture and use date back to the 19th century. Its usefulness derives from its micropore and mesopore volumes and the resulting high surface area. Activated carbon can be represented by a model of a twisted network of defective hexagonal carbon layer with functional groups bound to the periphery of the planes [20]. These surface groups play a key role in the surface chemistry of activated carbon. Some typical functional groups are shown in **Figure 2.5**.

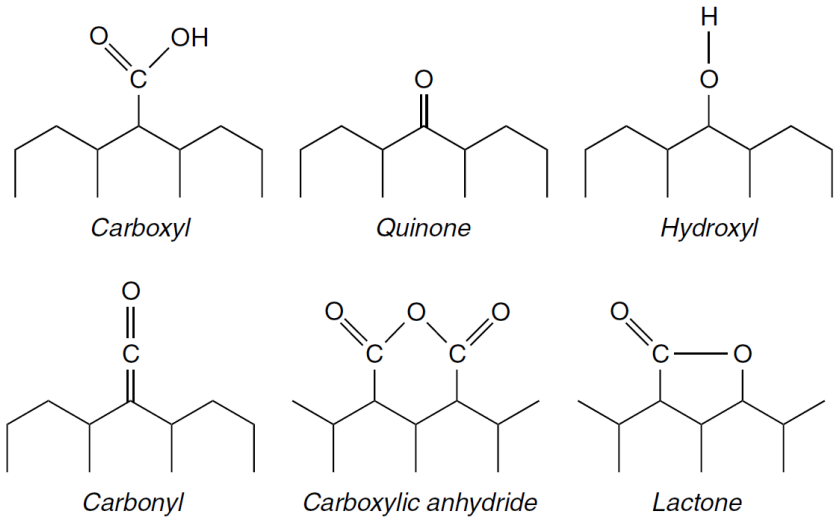

Figure 2.5 Surface groups on activated carbon [20]

The activated carbon described above with bounded surface groups will have a molecular structure [21] something similar to **Figure 2.6**.

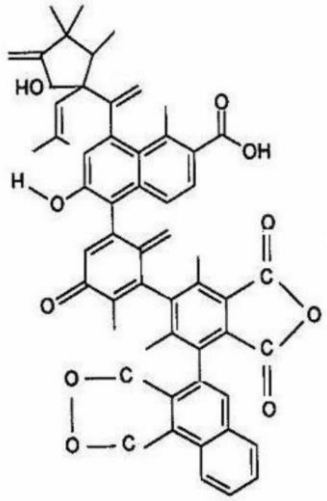

Figure 2.6 Molecular structure of Activated Carbon [21]

Activated carbon structure described above is modelled using Spartan software. Molecular mechanics calculations using Merck Molecular Force Field (MMFF) are performed to find the energy ($E_{adsorbent}$) relating to the isolated activated carbon. The resulting molecular model of an AC unit is depicted as follows:

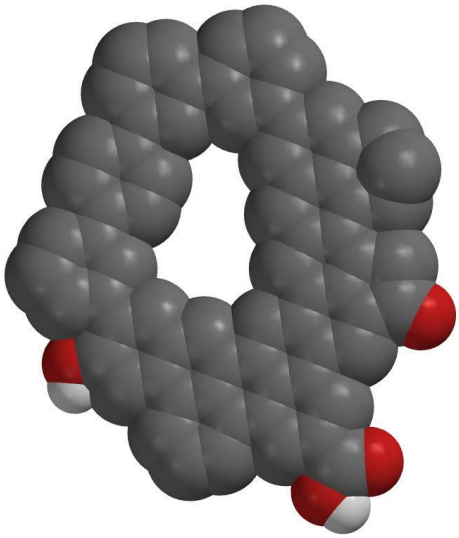

Figure 2.7 Molecular model of Activated Carbon in Spartan

Similarly, the energy ($E_{adsorbate}$) relating to the isolated gas components (H_2, CH_4, CO, CO_2, N_2, O_2) are calculated. Now, each of the gas component are placed along with the activation carbon and tested for possible binding sites by performing molecular mechanics calculation. The gas molecule tends to occupy the lowest energy position. An energy profile is created to identify the lowest energy position ($E_{adsorbent+adsorbate}$). Now with the values of $E_{adsorbent}$, $E_{adsorbate}$ and $E_{adsorbent+adsorbate}$ known, the heat of adsorption $\Delta H_{adsorption}$ is calculated using the equation (2.7). The simulation results of the molecular modeling simulation for activated carbon adsorption are summarised in **Table 2.8** as follows:

Table 2.8 Results of molecular modeling calculations for AC

Component	$E_{adsorbate}$ (kJ mol^{-1})	$E_{adsorbent}$ (kJ mol^{-1})	$E_{adsorbent+adsorbate}$ (kJ mol^{-1})	$\Delta H_{adsorption}$ (kJ mol^{-1})
H_2	0	2511.75	2507.01	-4.75
CH_4	0.11		2495.25	-16.61
CO	0		2497.84	-13.92
CO_2	0		2475.89	-35.86
N_2	0		2496.03	-15.72
O_2	0		2497.96	-13.79

Figure 2.8 shows the preferred sites of adsorption for different gas components on activated carbon from molecular mechanics calculations.

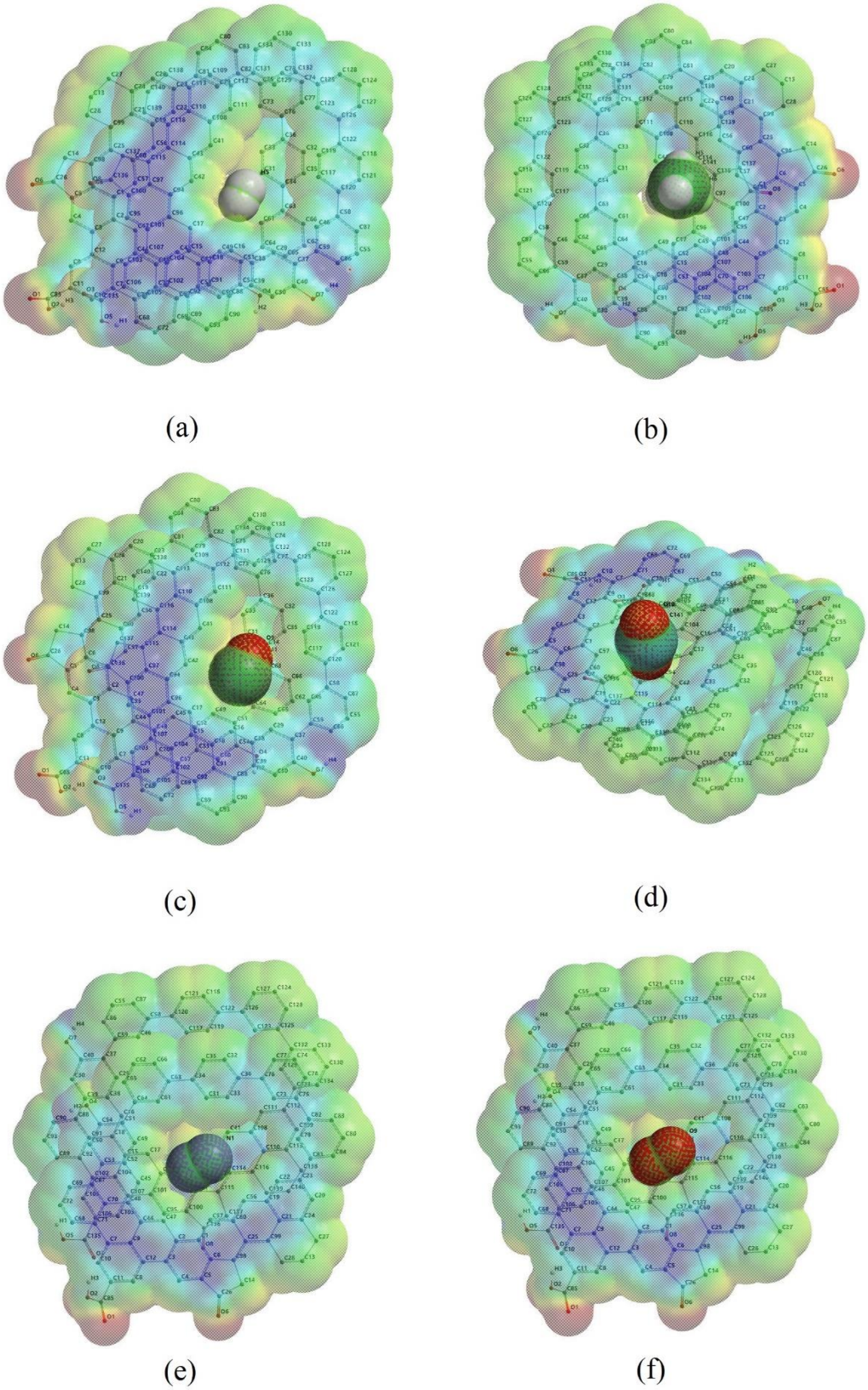

Figure 2.8 Binding sites of (a) H_2 (b) CH_4 (c) CO (d) CO_2 (e) N_2 (f) O_2 on AC

The above calculated energies (E) using molecular mechanics (MMFF) are all strain energies which are the sum of all the forces within the molecule and also the forces between the molecules. This is equivalent to the sum of a series of simple springs based on Hooke's law combined with a good physical description of weak van der Waals energy and hydrogen bridge interactions. A detailed explanation for strain energy is provided in appendix section A.1. Strain Energy relation in Molecular modeling [49]

Now the ΔH values calculated from molecular modeling are compared with those calculated from experimental values and the results are shown in **Table 2.9**. The results match quite well for all gas components except for CO_2. The isosteric heat of adsorption for CO_2 calculated from molecular modeling is -35.86 kJ mol^{-1}, while that from the experimental calculations has a value of only -17.74 kJ mol^{-1}. From literature study [15], it can be seen that the heat of adsorption for CO_2 on certain activated carbon structures can be -35 kJ mol^{-1} based on the difference in loading.

Also, considering the facts that the experimental data are subjected to thermal noise (RT ~ 3 kJ mol^{-1}) and that the data computed from molecular modeling are essentially at 0 K, the resemblance between experimental and simulated results of the heat of adsorption values is very good.

Table 2.9 Comparison between experimental and model values of Δ*H* on activated carbon

Component	$\Delta H_{experimental}$ (kJ mol^{-1})	ΔH_{model} (kJ mol^{-1})
H_2	-2.63	-4.75
CH_4	-17.74	-16.61
CO	-13.28	-13.92
CO_2	-17.09	-35.86
N_2	-12.73	-15.72
O_2	-11.83	-13.79

Next to the calculation of adsorption enthalpies, their corresponding entropy values are calculated from molecular modeling and their results are shown in **Table 2.10**

Table 2.10 Entropy calculation from molecular modeling

Component	$S_{adsorbate}$ (J mol^{-1} K)	$S_{adsorbent}$ (J mol^{-1} K^{-1})	$S_{adsorbent+adsorbate}$ (J mol^{-1} K^{-1})	$\Delta S_{adsorption}$ (J mol^{-1} K^{-1})
H_2	130.15	1556.26	1597.84	-88.57
CH_4	186.2		1606.62	-135.84
CO	197.29		1598.04	-155.51
CO_2	214.33		1601.43	-169.16
N_2	191.76		1597.98	-150.04
O_2	195.95		1598.04	-154.17

As explained in section 2.3, the pre-exponential factor (b_0) of adsorption equilibrium constant (b) as calculated from the experimental values is a function of ΔS given by

$$b_0 = \exp\left(\frac{\Delta S}{R}\right)$$

Table 2.11 Comparison of ΔS/R values from experimental and molecular modeling methods

Component	$\Delta S_{exp}/R$ (J mol^{-1} K)	$\Delta S_{model}/R$ (J mol^{-1} K)
H_2	-4.74	-10.65
CH_4	-8.33	-16.33
CO	-7.19	-18.70
CO_2	-7.48	-20.34
N_2	-7.26	-18.04
O_2	-7.25	-18.54

The ΔS/R values of experimental and molecular modeling results are compared as seen in **Table 2.11**. It can be seen that the ΔS/R values calculated from molecular modeling using MMFF approach are quite high compared to the experimental values. The problem with variation in entropy values is due to the reason that the basic model of small gas phase molecules is not inherently correct with respect to real situation. The adsorbents are not in gas phase but are either in the form of solid or viscous liquid, so a gas phase approach for entropy calculation cannot be good. Hence the static MMFF approach is not particularly good enough for entropy calculations.

However in case of physisorption processes, the approach to approximate the entropy values using Trouton's constant is satisfactory. Trouton's rule states that the entropy of vaporization (ΔS_{vap}) is almost the same value of about 85–88 J K^{-1} mol^{-1} for various kinds of liquids at their boiling points[22], [23]. Mathematically, Trouton's constant is expressed as

$$\frac{\Delta S_{vap}}{R} = 10.4$$

This rule could also be extended for adsorption of small gas molecules due to the fact that the entropy change of adsorption process is relatively insensitive to the molecular parameters employed in the calculations. The standard entropy changes calculated from Trouton's constant is in good agreement with most of the experimental values except for hydrogen. Thus, the relative insensitivity of entropy to the molecular parameters involved in the calculation allows for good estimation of the pre-exponential factor (b_0) for adsorption of different gas components with the exception of H_2.

2.4.2 Modeling of Zeolite LiX adsorbent

Zeolites are crystalline aluminosilicates of alkali or alkali earth elements, such as sodium, potassium, lithium and calcium and their chemical composition [20] are represented by:

$$M_{x/n}\left[(AlO_2)_x(SiO_2)_y\right].zH_2O$$

where x and y are integers with y/x ratio equal to or greater than 1. Greater ratio of y/x, yields flexibility to the adsorbent while lesser ratio yields rigidity to the adsorbent. n is the valence of the cation M and z is the number of water molecules in each unit cell.

The water molecules can be easily removed upon heating and evacuation leaving an almost unaltered aluminosilicates skeleton having a void fraction between 0.2 and 0.5 [20]. The skeleton has a regular structure of cages which are interconnected by windows in each cage. The cages can hold large amount of gas molecules in place of water.

More than 150 synthetic zeolite types are known, the most commercially important are the synthetic types A and X, synthetic mordenite and their ion-exchanged varieties. Of the 40 or so mineral zeolites, the most commercial ones are chabazite, faujasite and mordenite.

International Zeolite Association (IZA) provides a complete database of all possible zeolite structures. Our adsorbent of interest, Zeolite LiX belong to Faujasite (FAU) type. The framework of FAU type zeolite is shown in **Figure 2.9**. The basic building units of the FAU framework are hexagonal prism and sodalite cage. The sodalite cages are linked through the hexagonal prism to form faujasite unit cell with a super-cage structure.

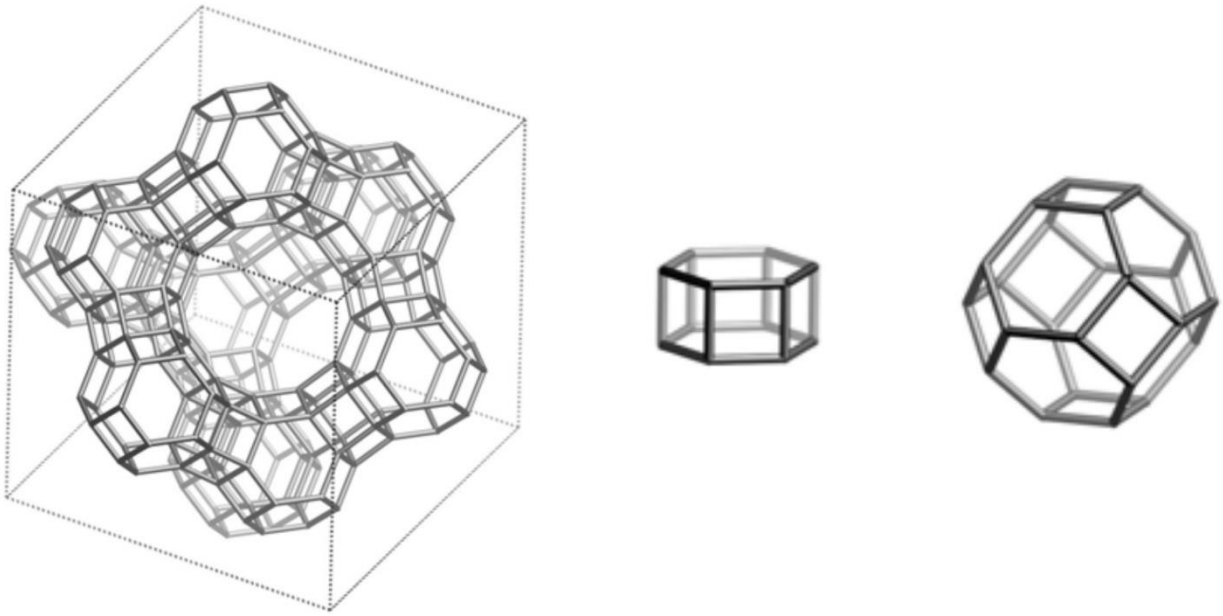

Figure 2.9 Framework and building units of FAU type zeolite [24]

The basic FAU structure made of Si and O atoms is taken from IZA database and is shown in **Figure 2.10**. When all lattice ions are Si, the zeolite lattice has the composition SiO_2 and is a polymorph of quartz. Bronsted acidic sites are generated when Si which has a formal valence of four is replaced by Al metal atom with a formal valence of three. Lithium cation is attached to the oxygen atom connecting the Si and Al atom, resulting in a chemically stable situation [25].

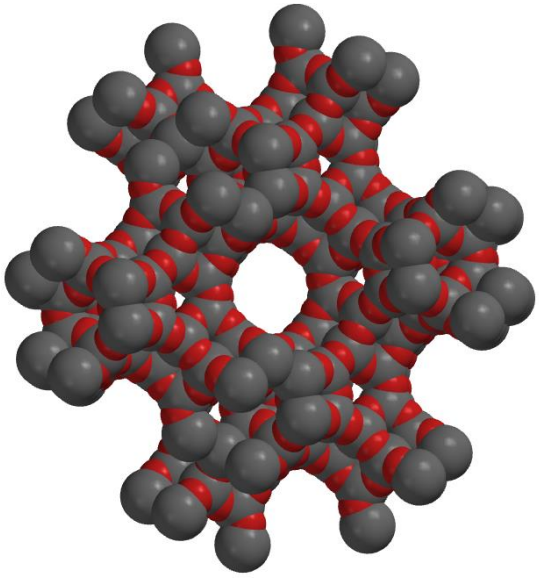

Figure 2.10 FAU unit cell structure in Spartan

Since a unit cell of FAU has too many atoms, the computational time required is very high. Hence, the unit cell is broken down into sodalite, hexagonal prism and super-cage structures as shown in **Figure 2.11** to perform faster molecular mechanics calculations.

Molecular mechanics calculations using Merck Molecular Force Field (MMFF) are performed to find the equilibrium geometry relating to each of the isolated basic units of zeolite. The integrity of sodalite and super-cage structures were found to remain intact after optimisation showing the stability of the structures.

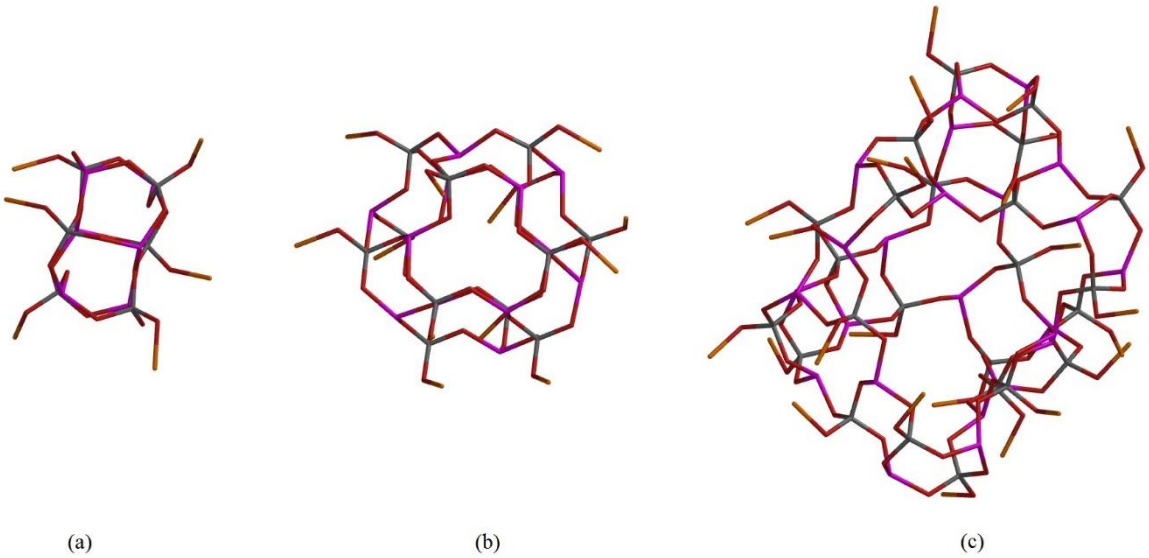

Figure 2.11 Tube model of (a) Hexagonal prism (b) Sodalite cage (c) Super-cage

With the adsorbent energy calculated ($E_{adsorbent}$), the energy ($E_{adsorbate}$) relating to the isolated gas components (H_2, CH_4, CO, CO_2, N_2, O_2) are calculated in a similar manner.

Now, each of the gas components are placed along with the zeolite units and tested for possible binding sites by performing molecular mechanics calculation. The gas molecule tends to occupy the lowest energy position. An energy profile is created to identify the lowest energy position ($E_{adsorbent+adsorbate}$).

Now with the values of $E_{adsorbent}$, $E_{adsorbate}$ and $E_{adsorbent+adsorbate}$ known, the heat of adsorption $\Delta H_{adsorption}$ is calculated using the equation (2.7).

It was found that all gas components except hydrogen have their lowest energy binding position in the super-cage. Hydrogen has its primary binding site in the sodalite cage with an isosteric heat of adsorption value of -7.15 kJ mol^{-1} and secondary binding site with a value of -4.04 kJ mol^{-1} in the super-cage.

The simulation results of the super-cage molecular mechanics calculation results are summarised in as **Table 2.12** follows:

Table 2.12 Results of molecular modeling calculations for LiX

Component	$E_{adsorbate}$ (kJ mol^{-1})	$E_{adsorbent}$ (kJ mol^{-1})	$E_{adsorbent+adsorbate}$ (kJ mol^{-1})	$\Delta H_{adsorption}$ (kJ mol^{-1})
H_2	0	8891.31	8887.27	-4.04
CH_4	0.11		8878.17	-13.24
CO	0		8876.94	-14.37
CO_2	0		8865.62	-25.69
N_2	0		8877.65	-13.65
O_2	0		8880.56	-10.75

Figure 2.12 shows the preferred sites of adsorption for different gas components on zeolite LiX from molecular mechanics calculations.

Now the ΔH values calculated from molecular modeling are compared with those calculated from experimental values and the results are shown in **Table 2.13** .

Table 2.13 Comparison between experimental and model values of ΔH on activated carbon

Component	$\Delta H_{experimental}$ (kJ mol^{-1})	ΔH_{model} (kJ mol^{-1})
H_2	-3.56	-4.04
CH_4	-14.84	-13.24
CO	-11.81	-14.37
CO_2	-28.49	-25.69
N_2	-17.14	-13.65
O_2	-8.94	-10.75

The simulation results of both activated carbon and zeolite LiX adsorbents are matching well with the experimental values. This shows that the molecular mechanics (MMFF) method is extremely good in predicting the isosteric heat of adsorption values quite close to experimental values considering the huge approximations made.

The procedure followed in building and optimization of the adsorbent molecules are briefly summarised in appendix section A.3. Building and optimisation procedures followed for modeling of adsorbent molecules needed for research using Spartan Molecular Mechanics model. The created set of general models for adsorption using carbon and zeolites can be operated as separate modules, thereby increasing the overall value of the models.

Hence, using molecular modeling approach to calculate the adsorption equilibrium data is simple and could save a lot of time, energy and cost as compared to the conventional experimental approach. Thereby, more fundamental studies on the adsorption of different gas species on different adsorbent materials can be performed using molecular modeling without being restricted to the limited adsorption literature resources from the industries.

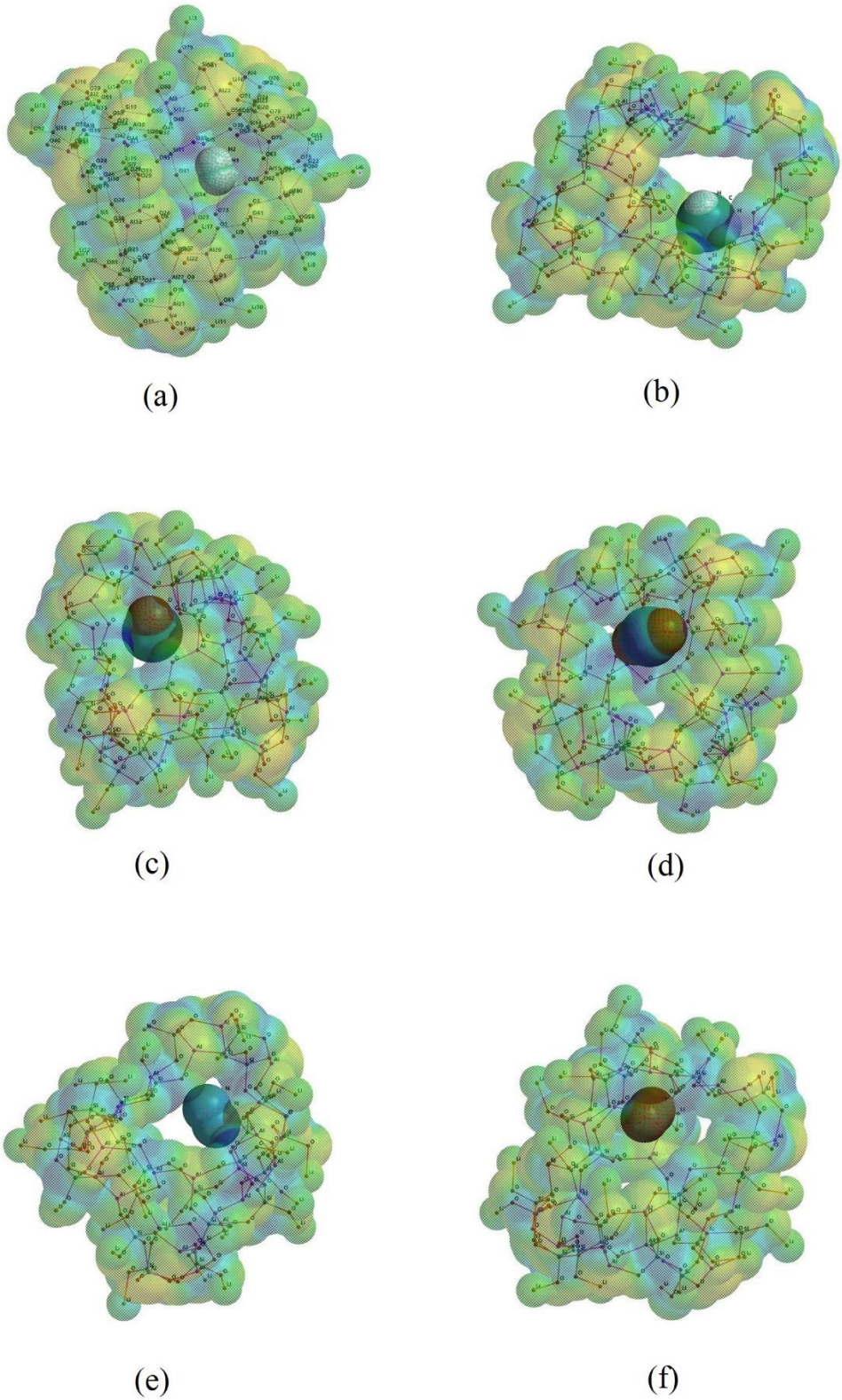

Figure 2.12 Binding sites of (a) H_2 (b) CH_4 (c) CO (d) CO_2 (e) N_2 (f) O_2 on LiX

Chapter 3

Mathematical Modeling

3.1 Introduction

Process simulation has become an essential part of a process engineer's work ever since the evolution of modern processors capable of computing complex equations in a reasonable amount of time. Adsorption processes are dynamic in nature unlike the steady state behaviour exhibited by other major separation processes like distillation and absorption. Hence, analytical solutions that work well with the above mentioned steady state separation technologies are not sufficient for adsorption processes. This impedes the development of a design method for adsorption process as those used in the steady state technologies.

Numerical methods have become increasingly popular and feasible with the modern powerful computers. Simulators developed for pressure swing adsorption (PSA) systems require complex boundary conditions that allows quick outcome predictions from changes in process conditions like pressure, temperature and composition etc. and make corresponding adjustments. The simulation also reduces capital investment in the preliminary design of a novel process cycle. Hence, a detailed model put into an accurate simulator allows a process engineer to optimize a process as complex as PSA rapidly while inspiring industrial confidence at the same time [8].

A pressure swing adsorption bed model must take into account the simultaneous mass, heat and momentum balances in the bulk gas flow, the transport and thermo-physical properties of the gas mixture and a set of boundary conditions for the input and output from the bed and the interface between the bulk gas and particle surface [26]–[29].

The following assumptions are used to derive the model equations [30].

- The gas components are following ideal gas behaviour
- The gas flow follows the axially dispersed plug flow model
- The mass transfer rate follows the linear driving force (LDF) model
- The frictional pressure drop in axial direction follows Darcy's law
- The pressure, temperature and concentration gradients in the radial direction are negligible
- The gas and the adsorbent are in a state of thermal equilibrium
- Heat transfer occurs along the column wall whose outer surface is maintained at a constant temperature
- The adsorbent properties and bed porosity are uniform along the column

3.2 Model equations

The component mass balance equation is given by

$$\varepsilon \frac{\partial c_i}{\partial t} + (1-\varepsilon)\varepsilon_p \frac{\partial c_i}{\partial t} + \varepsilon \frac{\partial}{\partial z}\left[-D_{ax}\frac{\partial c_i}{\partial z} + c_i v\right] + (1-\varepsilon)\frac{\partial q_i}{\partial t} = 0 \tag{3.1}$$

By applying Ideal Gas Law, $c_i = \frac{y_i P}{RT}$ and rearranging the terms, equation (3.1) becomes,

$$\frac{\partial y_i}{\partial t} = \frac{D_{ax}}{\left(1+\frac{\varepsilon_p}{\varepsilon}-\varepsilon_p\right)}\frac{T}{P}\frac{\partial}{\partial z}\left(\frac{P}{T}\frac{\partial y_i}{\partial z}\right) - \frac{1}{\left(1+\frac{\varepsilon_p}{\varepsilon}-\varepsilon_p\right)}\frac{T}{P}\frac{\partial}{\partial z}\left(y_i\frac{P}{T}v\right) - \frac{\left(\frac{1-\varepsilon}{\varepsilon}\right)}{\left(1+\frac{\varepsilon_p}{\varepsilon}-\varepsilon_p\right)}\frac{RT}{P}\frac{\partial q_i}{\partial t} - \frac{y_i}{P}\frac{\partial P}{\partial t} + \frac{y_i}{T}\frac{\partial T}{\partial t} \tag{3.2}$$

The total mass balance equation is given by

$$\varepsilon\frac{\partial \rho_g}{\partial t} + \varepsilon\frac{\partial}{\partial z}(\rho_g v) + (1-\varepsilon)\left(\varepsilon_p\frac{\partial \rho_g}{\partial t} + \sum_{i=1}^{n_{comp}}\frac{\partial q_i}{\partial t}\right) = 0 \tag{3.3}$$

By applying Ideal Gas Law, $\rho_g = \frac{P}{RT}$ and rearranging the terms, equation (3.3) becomes,

$$\frac{\partial P}{\partial t} = -\frac{\left(\frac{1-\varepsilon}{\varepsilon}\right)}{\left(1+\frac{\varepsilon_p}{\varepsilon}-\varepsilon_p\right)}RT\sum_{i=1}^{n_{comp}}\frac{\partial q_i}{\partial t} - \frac{1}{\left(1+\frac{\varepsilon_p}{\varepsilon}-\varepsilon_p\right)}T\frac{\partial}{\partial z}\left(\frac{P}{T}v\right) + \frac{P}{T}\frac{\partial T}{\partial t} \tag{3.4}$$

The rate of adsorption into solid phase considering LDF model is given by

$$\frac{\partial q_i}{\partial t} = k_i(q_i^* - q_i) \tag{3.5}$$

The energy balance for solid and gas phase is given by

$$\left[\varepsilon\rho_g C_{pg} + (1-\varepsilon)\varepsilon_p\rho_g C_{pg} + (1-\varepsilon)\rho_s C_{ps}\right]\frac{\partial T}{\partial t} - (1-\varepsilon)\sum_{i=1}^{n_{comp}}\left((-\Delta H_i)\frac{\partial q_i}{\partial t}\right) - \lambda_{ax}\frac{\partial^2 T}{\partial z^2} + \varepsilon\rho_g C_{pg}\frac{\partial}{\partial z}(vT) + \frac{2h_{in}}{r_{in}}(T - T_w) = 0 \tag{3.6}$$

Rearranging the equation,

$$\frac{\partial T}{\partial t} = \frac{\frac{\lambda_{ax}}{\varepsilon}}{\frac{\rho_g C_{pg}}{\varepsilon}+\left(\frac{1-\varepsilon}{\varepsilon}\right)\varepsilon_p\rho_g C_{pg}+\left(\frac{1-\varepsilon}{\varepsilon}\right)\rho_s C_{ps}}\frac{\partial^2 T}{\partial z^2} - \frac{\rho_g C_{pg}}{\frac{\rho_g C_{pg}}{\varepsilon}+\left(\frac{1-\varepsilon}{\varepsilon}\right)\varepsilon_p\rho_g C_{pg}+\left(\frac{1-\varepsilon}{\varepsilon}\right)\rho_s C_{ps}}\frac{\partial}{\partial z}(vT) + \frac{\left(\frac{1-\varepsilon}{\varepsilon}\right)}{\frac{\rho_g C_{pg}}{\varepsilon}+\left(\frac{1-\varepsilon}{\varepsilon}\right)\varepsilon_p\rho_g C_{pg}+\left(\frac{1-\varepsilon}{\varepsilon}\right)\rho_s C_{ps}}\sum_{i=1}^{n_{comp}}\left((-\Delta H_i)\frac{\partial q_i}{\partial t}\right) - \frac{\frac{2h_{in}}{\varepsilon r_{in}}}{\frac{\rho_g C_{pg}}{\varepsilon}+\left(\frac{1-\varepsilon}{\varepsilon}\right)\varepsilon_p\rho_g C_{pg}+\left(\frac{1-\varepsilon}{\varepsilon}\right)\rho_s C_{ps}}(T - T_w) \tag{3.7}$$

The energy balance for walls is given by

$$\rho_w C_{pw} \frac{\partial T_w}{\partial t} - \lambda_w \frac{\partial^2 T_w}{\partial z^2} - \frac{2 r_{in} h_{in}}{r_{out}^2 - r_{in}^2}(T - T_w) + \frac{2 r_{out} h_{out}}{r_{out}^2 - r_{in}^2}(T_w - T_a) = 0 \quad (3.8)$$

Rearranging the equation,

$$\frac{\partial T_w}{\partial t} = \frac{\lambda_w}{\rho_w C_{pw}} \frac{\partial^2 T_w}{\partial z^2} + \frac{1}{\rho_w C_{pw}} \frac{2 r_{in} h_{in}}{r_{out}^2 - r_{in}^2}(T - T_w) - \frac{1}{\rho_w C_{pw}} \frac{2 r_{out} h_{out}}{r_{out}^2 - r_{in}^2}(T_w - T_a) \quad (3.9)$$

According to Darcy's law, pressure drop along the length of the column is given by

$$\frac{\partial P}{\partial z} = -\frac{150}{4} \frac{1}{r_p^2} \left(\frac{1-\varepsilon}{\varepsilon}\right)^2 \mu v \quad (3.10)$$

The interstitial velocity is evaluated by rearranging equation (3.10)

$$v = \left(-\frac{\partial P}{\partial z}\right) \frac{4}{150} r_p^2 \left(\frac{\varepsilon}{1-\varepsilon}\right)^2 \frac{1}{\mu} \quad (3.11)$$

Axial concentration and temperature gradients always exist in packed beds. Hence, a diffusive mass and heat transfer will always occur and tend to degrade the performance of the process. Therefore an accurate prediction of mass and thermal axial dispersion coefficients is very important for detailed modeling of the flow through the packed bed. Wakao developed one of the most widely used coefficients [26]:

$$D_{ax} = \frac{D_m}{\varepsilon}(20 + 0.5\, Sc\, Re) \quad (3.12)$$

$$\lambda_{ax} = \lambda_g(7 + 0.5\, Pr\, Re) \quad (3.13)$$

where

Schmidt number, $Sc = \frac{\mu}{\rho_g D_m}$

Reynolds number, $Re = \frac{\rho_g \varepsilon u d_p}{\mu}$

Prandtl number, $Pr = \frac{C_{pg} \mu}{\lambda_g}$

The molecular diffusivity is calculated using Chapman-Enskog equation [14], [31].

$$D_{m,i} = 0.0018583 \frac{T^{\frac{3}{2}}\left(\frac{1}{MW_i}\right)^{\frac{1}{2}}}{P\sigma^2\Omega} \tag{3.14}$$

where the Lennard Jones potential energy function [32], [33] is given by

$$\sigma = \frac{\sigma_1 + \sigma_2 + \sigma_3 + \cdots + \sigma_n}{n}$$

$$\xi = \sqrt{\xi_1 \xi_2 \ldots \xi_n}$$

and the collision integral is a function given by

$$\Omega = f\left(\frac{k_B T}{\xi}\right)$$

The Knudsen diffusivity [14] is calculated using the following equation.

$$D_{k,i} = 9.7 * 10^3 \, r_{pore} \sqrt{\frac{T}{MW_i}} \tag{3.15}$$

The effective diffusivity is given by

$$D_{e,i} = \frac{\varepsilon_p}{\tau} \frac{1}{\left(\frac{1}{D_{m,i}} + \frac{1}{D_{k,i}}\right)} \tag{3.16}$$

The mass transfer coefficient is calculated using the effective diffusivity [14] using the following formula

$$k_i = \frac{15 D_{e,i}}{r_p^2} \tag{3.17}$$

3.3 Numerical Methods for Solving the Partial Differential Equations

To understand an adsorption problem, solving its governing equations are necessary, which are generally a set of partial differential equations (PDE). Although solving PDEs analytically is not impossible, it is tedious and impractical compared to ordinary differential equations (ODE). To overcome this problem, various numerical methods are available to give approximate solution close enough to analytical solution. Two such predominantly applied schemes are finite volume methods (FVM) and finite difference methods (FDM). These numerical methods approximate the PDEs by discretising the spatial dimension to convert PDEs into ODEs in time. The ODEs can then be solved by powerful ODE solving schemes such as the Runge-Kutta method.

Inorder to rigorously optimize cyclic adsorption processes using detailed models, robust numerical simulation techniques are necessary. The scheme should be fast and robust enough to handle stiff problems, while capturing the process dynamics and performance accurately. Due to the nature of the conservation equations, sharp fronts of concentration and temperature may propagate along the adsorption bed. Assuring the accuracy and stability of the model in such situations is challenging, especially when dealing with highly non-linear isotherms.

FDM cannot handle discontinuities where sharp fronts can occur. Another issue with FDM is that mass is not rigorously conserved. Although the accuracy could be increased by having finer grids, the computation time increases significantly. FVM rely on integration to give a more fundamental interpretation of mass, energy or momentum fluxes between interfaces, thereby the mass, energy and momentum conservations are rigorous. Several papers comparing FDM and FVM shown that FVM is more accurate and as a result, coarser grids can be used saving computational time [8], [30], [34], [35]. Hence, in this work FVM is chosen for the spatial discretisation.

Finite Volume Method for Spatial Discretisation

The column is divided into N cells each having a volume of ΔV as shown in **Figure 3.1**. Any conserved quantity f is approximated by a cell average given by,

$$f_j(t) = \frac{1}{\Delta V}\int_{V_j} f(t)dV \tag{3.18}$$

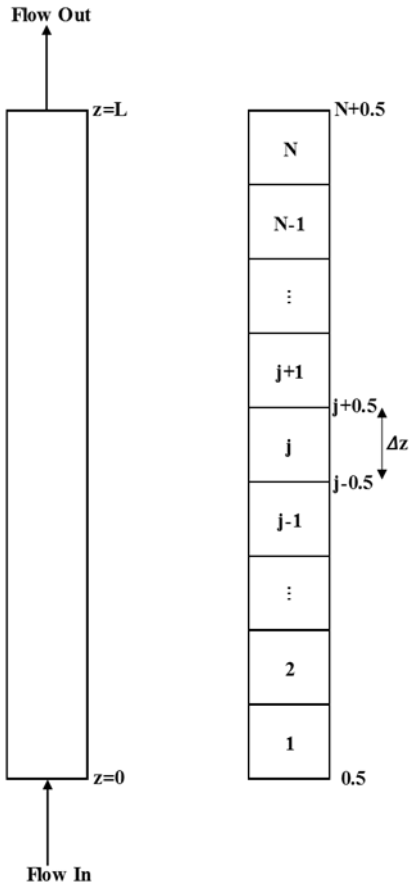

Figure 3.1 Discretisation of adsorption column

The spatial derivatives in the governing equations are converted to algebraic expressions by integration over each cell j with boundaries denoted as j-0.5 and j+0.5. The equations (3.1) – (3.11) in the discretised form are as follows:

Component Mass Balance:

$$\frac{\partial y_{i,j}}{\partial t} = \frac{D_{ax}}{\left(1+\frac{\varepsilon_p}{\varepsilon}-\varepsilon_p\right)}\frac{T_j}{P_j}\frac{1}{\Delta Z}\left(\left(\frac{P_{j+0.5}}{T_{j+0.5}}\frac{y_{i,j+1}-y_{i,j}}{\Delta Z}\right)-\left(\frac{P_{j-0.5}}{T_{j-0.5}}\frac{y_{i,j}-y_{i,j-1}}{\Delta Z}\right)\right)-$$
$$\frac{1}{\left(1+\frac{\varepsilon_p}{\varepsilon}-\varepsilon_p\right)}\frac{T_j}{P_j}\frac{1}{\Delta Z}\left(\left(y_{i,j+0.5}\frac{P_{j+0.5}}{T_{j+0.5}}v_{j+0.5}\right)-\left(y_{i,j-0.5}\frac{P_{j-0.5}}{T_{j-0.5}}v_{j-0.5}\right)\right)-$$
$$\frac{\left(\frac{1-\varepsilon}{\varepsilon}\right)}{\left(1+\frac{\varepsilon_p}{\varepsilon}-\varepsilon_p\right)}\frac{RT_j}{P_j}\frac{\partial q_{i,j}}{\partial t}-\frac{y_{i,j}}{P_j}\frac{\partial P_j}{\partial t}+\frac{y_{i,j}}{T_j}\frac{\partial T_j}{\partial t} \tag{3.19}$$

Total Mass Balance:

$$\frac{\partial P_j}{\partial t} = -\frac{\left(\frac{1-\varepsilon}{\varepsilon}\right)}{\left(1+\frac{\varepsilon_p}{\varepsilon}-\varepsilon_p\right)}RT_j\sum_{i=1}^{n_{comp}}\frac{\partial q_{i,j}}{\partial t}-\frac{1}{\left(1+\frac{\varepsilon_p}{\varepsilon}-\varepsilon_p\right)}T_j\frac{1}{\Delta Z}\left(\left(\frac{P_{j+0.5}}{T_{j+0.5}}v_{j+0.5}\right)-\left(\frac{P_{j-0.5}}{T_{j-0.5}}v_{j-0.5}\right)\right)+\frac{P_j}{T_j}\frac{\partial T_j}{\partial t} \tag{3.20}$$

Rate of Adsorption:

$$\frac{\partial q_{i,j}}{\partial t} = k_{i,j}\left(q^*_{i,j}-q_{i,j}\right) \tag{3.21}$$

Column Energy Balance:

$$\frac{\partial T_j}{\partial t} = \frac{\frac{\lambda_{ax}}{\varepsilon}}{\frac{\rho_{g,j}C_{pg}}{\varepsilon}+\left(\frac{1-\varepsilon}{\varepsilon}\right)\varepsilon_p\rho_{g,j}C_{pg}+\left(\frac{1-\varepsilon}{\varepsilon}\right)\rho_s C_{ps}}\frac{1}{\Delta Z}\left(\frac{T_{j+1}-T_j}{\Delta Z}-\frac{T_j-T_{j-1}}{\Delta Z}\right)-$$
$$\frac{\frac{\rho_{g,j}C_{pg}}{\varepsilon}}{\frac{\rho_{g,j}C_{pg}}{\varepsilon}+\left(\frac{1-\varepsilon}{\varepsilon}\right)\varepsilon_p\rho_{g,j}C_{pg}+\left(\frac{1-\varepsilon}{\varepsilon}\right)\rho_s C_{ps}}\frac{1}{\Delta Z}\left(v_{j+0.5}T_{j+0.5}-v_{j-0.5}T_{j-0.5}\right)+$$
$$\frac{\left(\frac{1-\varepsilon}{\varepsilon}\right)}{\frac{\rho_{g,j}C_{pg}}{\varepsilon}+\left(\frac{1-\varepsilon}{\varepsilon}\right)\varepsilon_p\rho_{g,j}C_{pg}+\left(\frac{1-\varepsilon}{\varepsilon}\right)\rho_s C_{ps}}\sum_{i=1}^{n_{comp}}\left(\left(-\Delta H_i\right)\frac{\partial q_{i,j}}{\partial t}\right)-$$
$$\frac{\frac{2h_{in}}{\varepsilon r_{in}}}{\frac{\rho_{g,j}C_{pg}}{\varepsilon}+\left(\frac{1-\varepsilon}{\varepsilon}\right)\varepsilon_p\rho_{g,j}C_{pg}+\left(\frac{1-\varepsilon}{\varepsilon}\right)\rho_s C_{ps}}\left(T_j-T_{w,j}\right) \tag{3.22}$$

Wall Energy Balance:

$$\frac{\partial T_{w,j}}{\partial t} = \frac{\lambda_w}{\rho_w C_{pw}} \frac{1}{\Delta Z}\left(\frac{T_{w,j+1}-T_{w,j}}{\Delta Z} - \frac{T_{w,j}-T_{w,j-1}}{\Delta Z}\right) + \frac{1}{\rho_w C_{pw}} \frac{2 r_{in} h_{in}}{r_{out}^2 - r_{in}^2}\left(T_j - T_{w,j}\right) - \frac{1}{\rho_w C_{pw}} \frac{2 r_{out} h_{out}}{r_{out}^2 - r_{in}^2}\left(T_{w,j} - T_a\right) \tag{3.23}$$

Pressure drop along the length of the column:

$$\frac{P_{j+0.5}-P_{j-0.5}}{\Delta Z} = -\frac{150}{4}\frac{1}{r_p^2}\left(\frac{1-\varepsilon}{\varepsilon}\right)^2 \mu v_j \tag{3.24}$$

Interstitial velocity along the column:

$$v_{j+0.5} = -\left(\frac{P_{j+1}-P_j}{\Delta Z}\right)\frac{4}{150} r_p^2 \left(\frac{\varepsilon}{1-\varepsilon}\right)^2 \frac{1}{\mu} \tag{3.25}$$

In cases where sharp discontinuities propagate in the system, weighted essentially non-oscillatory (WENO) methods have successfully been implemented with the FVM framework to reduce non-physical oscillations around discontinuities, while still capturing the smooth portion of the solution. In the WENO scheme, a convex combination of lower order fluxes is employed to achieve a higher order approximation. A non-linear adaptive procedure is used in WENO scheme to automatically choose the locally smoothest stencil in order to avoid non-physical oscillations near discontinuities [30].

The WENO scheme relation is given by

$$f_{j+0.5} = \frac{\alpha_{0,j}}{\alpha_{0,j}+\alpha_{1,j}}\left[\frac{1}{2}\left(f_j + f_{j+1}\right)\right] + \frac{\alpha_{1,j}}{\alpha_{0,j}+\alpha_{1,j}}\left[\frac{3}{2} f_j - \frac{1}{2} f_{j-1}\right] \tag{3.26}$$

where

$$\alpha_{0,j} = \frac{2/3}{\left(f_{j+1} - f_j + \delta\right)^4};$$

$$\alpha_{1,j} = \frac{1/3}{\left(f_j - f_{j-1} + \delta\right)^4}$$

The flux calculation at j+0.5 requires the state variable values at j-1, j and j+1. For j=2… (N-1) the state variable values are available and hence the calculations are rather straight forward. But, for j=1 and j=N calculation, the values of state variables at 0 and N+1 are required which are not available. This issue is overcome by adding two ghost cells, one to the left of cell 1 and other to the right of cell N. The value of the state variables at the ghost cells 0 and N+1 are calculated using the following approximations:

$$f_0 = 2(f_{0.5}) - f_1$$

$$f_{N+1} = 2(f_{N+0.5}) - f_N$$

Inorder to simplify the numerical simulation, the model equations are converted into their corresponding non-dimensionalized form.

Dimensionless coefficients in the model equations are as follows:

$$\overline{P} = \frac{P}{P_0};\ \overline{T} = \frac{T}{T_0};\ \overline{T}_w = \frac{T_w}{T_0};\ \overline{T}_a = \frac{T_a}{T_0};\ x_i = \frac{q_i}{q_{s0}};\ \bar{v} = \frac{v}{v_0};\ Z = \frac{z}{L};\ \tau = t\frac{v_0}{L}$$

3.4 Boundary conditions

The solution of the above equations require proper initial and boundary conditions. Ideal initial condition assumes the column to be saturated with a known gas at particular pressure and temperature.

The boundary conditions for all the steps in the PSA cycle are generalized into three basic types as follows:

(a) Open-Open: In this type of flow, both the feed and product ends are open.

(b) Open-Closed: In this type of flow, the feed end is open while the product end is closed.

(c) Closed-Open: In this type of flow, the feed end is closed while the product end is open.

A combination of Dirichlet (the value of boundary point is specified) and Neumann (the derivative of boundary is specified) boundary conditions are used for close prediction of the behaviour of the column at its ends during different steps[30], [36].

If the flow across the column is in opposite direction, then the boundary conditions are reversed.

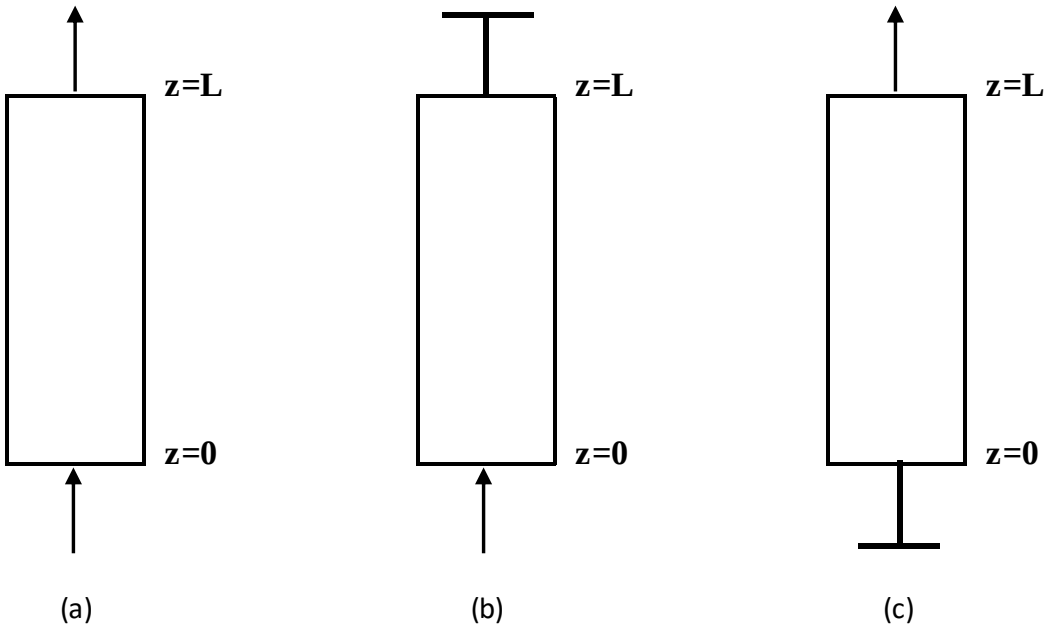

Figure 3.2 Boundary condition types for PSA process

Table 3.1 Generalised Boundary Conditions for different steps of PSA cycle

Step Type	z=0	z=L
Open-Open (Adsorption / Purge)	$\left.\frac{\partial y_i}{\partial z}\right\|_{z=0} = y_{i,feed}$ $\left.\frac{\partial T}{\partial z}\right\|_{z=0} = T_{feed}$ $T_w\|_{z=0} = T_a$ $v\|_{z=0} = v_{feed}$	$\left.\frac{\partial y_i}{\partial z}\right\|_{z=L} = 0$ $\left.\frac{\partial T}{\partial z}\right\|_{z=L} = 0$ $T_w\|_{z=L} = T_a$ $\left.\frac{\partial v}{\partial z}\right\|_{z=L} = 0$
Open-Closed (Repressurization / Pressure Equalisation ↑)	$\left.\frac{\partial y_i}{\partial z}\right\|_{z=0} = y_{i,feed}$ $\left.\frac{\partial T}{\partial z}\right\|_{z=0} = T_{feed}$ $T_w\|_{z=0} = T_a$ $v\|_{z=0} = v_{feed}$	$\left.\frac{\partial y_i}{\partial z}\right\|_{z=L} = 0$ $\left.\frac{\partial T}{\partial z}\right\|_{z=L} = 0$ $T_w\|_{z=L} = T_a$ $v\|_{z=L} = 0$
Closed-Open (Evacuation / Blowdown / Pressure Equalisation ↓)	$\left.\frac{\partial y_i}{\partial z}\right\|_{z=0} = 0$ $\left.\frac{\partial T}{\partial z}\right\|_{z=0} = 0$ $T_w\|_{z=0} = T_a$ $v\|_{z=0} = 0$	$\left.\frac{\partial y_i}{\partial z}\right\|_{z=L} = 0$ $\left.\frac{\partial T}{\partial z}\right\|_{z=L} = 0$ $T_w\|_{z=L} = T_a$ $\left.\frac{\partial v}{\partial z}\right\|_{z=L} = 0$

3.5 Mass and Energy Balance error

The accuracy of the model is checked by calculating mass and energy balance errors. The larger the number of discretisation volumes (N) the better the accuracy is. But large number of discretisation volumes, require high computational time. Hence, a balance between accuracy and computational time has to be made. It was found that for N≥50 the accuracy is sufficiently high (explained in Chapter 4).

The mass balance error can be calculated from the following equation:

$$\text{mass}_{\text{balance}} = \frac{\text{mass}_{\text{in}} - (\text{mass}_{\text{out}} + \text{mass}_{\text{acc}})}{\overline{\text{mass}}} \tag{3.27}$$

where

$$\text{mass}_{\text{in}} = \varepsilon A \int_0^{t_{\text{final}}} (\rho_g v)\big|_{z=0}\, dt$$

$$\text{mass}_{\text{out}} = \varepsilon A \int_0^{t_{\text{final}}} (\rho_g v)\big|_{z=L}\, dt$$

$$\text{mass}_{\text{acc}} = \text{mass}_{\text{acc,solid}} + \text{mass}_{\text{acc,fluid}}$$

$$\text{mass}_{\text{acc,fluid}} = \left[\varepsilon A \int_0^{L} \left(\rho_g\big|_{t=t_{\text{final}}} - \rho_g\big|_{t=0}\right) dz\right] + \left[(1-\varepsilon)\varepsilon_p A \int_0^{L} \left(\rho_g\big|_{t=t_{\text{final}}} - \rho_g\big|_{t=0}\right) dz\right]$$

$$\text{mass}_{\text{acc,solid}} = \left[(1-\varepsilon)A \int_0^{L} (\Sigma q_i|_{t=t_{\text{final}}} - \Sigma q_i|_{t=0})\; dz\right]$$

$$\overline{\text{mass}} = \frac{\text{mass}_{\text{in}} + \text{mass}_{\text{out}}}{2}$$

In addition to the mass balance error, the heat balance error can be calculated from the following equation:

$$\text{heat}_{\text{balance}} = \frac{\text{heat}_{\text{in}} + \text{heat}_{\text{gen}} - (\text{heat}_{\text{out}} + \text{heat}_{\text{acc}})}{\overline{\text{heat}}} \tag{3.28}$$

where

$$\text{heat}_{\text{in}} = \varepsilon A C_{pg} \int_0^{t_{\text{final}}} (T\rho_g v)\big|_{z=0}\, dt$$

$$\text{heat}_{\text{out}} = \varepsilon A C_{pg} \int_0^{t_{\text{final}}} (T\rho_g v)\big|_{z=L}\, dt$$

$$\text{heat}_{\text{gen}} = \left[(1-\varepsilon)A \int_0^{L} (\Sigma \Delta H_i q_i|_{t=t_{\text{final}}} - \Sigma \Delta H_i q_i|_{t=0})\; dz\right]$$

$$\text{heat}_{\text{acc}} = \text{heat}_{\text{acc,solid}} + \text{heat}_{\text{acc,fluid}}$$

$$\text{heat}_{\text{acc,solid}} = \left[(1-\varepsilon)AC_{ps}\rho_s \int_0^{L} \left(T|_{t=t_{\text{final}}} - T|_{t=0}\right) dz\right] + \left[A_w C_{pw} \rho_w \int_0^{L} (T_w|_{t=t_{\text{final}}} - T_w|_{t=0})\, dz\right]$$

$$\text{heat}_{\text{acc,fluid}} = \left[\varepsilon A C_{pg} \int_0^L \left(T\rho_g\big|_{t=t_{final}} - T\rho_g\big|_{t=0}\right) dz\right] + \left[(1-\varepsilon)\varepsilon_p A C_{pg} \int_0^L \left(T\rho_g\big|_{t=t_{final}} - T\rho_g\big|_{t=0}\right) dz\right]$$

$$\overline{\text{heat}} = \frac{\text{heat}_{in} + \text{heat}_{out}}{2}$$

3.6 Process Performance

The performance of the PSA process is evaluated by considering the following parametric values at CSS, defined by

1. Purity, which is the volume percentage of H_2 in the raffinate stream

$$\text{Purity } \% = \frac{\text{mass}_{out,H_2}\big|_{ads}}{\text{mass}_{out}\big|_{ads}} * 100$$

2. Recovery, which is the amount of H_2 recovered from the feed stream

$$\text{Recovery } \% = \frac{\text{mass}_{out,H_2}\big|_{ads}}{\text{mass}_{in,H_2}\big|_{ads} + \text{mass}_{in,H_2}\big|_{rep}} * 100$$

3. Productivity, which corresponds to the amount of H_2 produced per unit time per amount of adsorbent

$$\text{Productivity} = \frac{\text{mass}_{out,H_2}\big|_{ads}}{\text{adsorbent volume} * \text{cycle time}}$$

4. Total energy consumption, in terms of kilowatt hours per metric ton of H_2 produced

$$E_T = \frac{(E_{ads})}{\text{Mass of } H_2 \text{ in the raffinate stream per cycle}}$$

Where

$$E_{ads} = \frac{1}{\eta} \varepsilon A \left(\frac{\gamma}{\gamma - 1}\right) \int_0^{t_{ads}} vP\big|_{z=0} \left[\left(\frac{P\big|_{z=0}}{P_{COG}}\right)^{\frac{\gamma-1}{\gamma}} - 1\right] dt$$

3.7 Model Validation

The equations used in the mathematical model developed above are verified by comparing with different literatures [8], [12], [28], [30], [36]–[42] involving similar work. Inorder to quantitatively validate the model developed in the study, a simple pressure swing adsorption process for the separation of a binary gas mixture containing CO_2 and N_2 using zeolite 13X adsorbent is taken from literature [30]. Breakthrough simulations were performed with the developed model for the binary gas mixture separation with the operating conditions taken from the literature. The breakthrough simulation results obtained from the model were quite similar to the literature results thereby confirming the validity of the model developed in this study. A comparison of the literature and model results for the velocity, temperature and composition breakthrough profiles for CO_2 at the exit of the adsorption bed is shown in **Figure 3.3**. There is a slight variation in simulation results as compared with the literature results having a slower response especially in the second transition zone from 3500 sec to 4000 sec. This variation in results might possibly be due to the reason that the literature result considered constant diffusivity values, while the model developed in this study took proper account of the effects of temperature, pressure and gas composition while calculating the diffusivity terms.

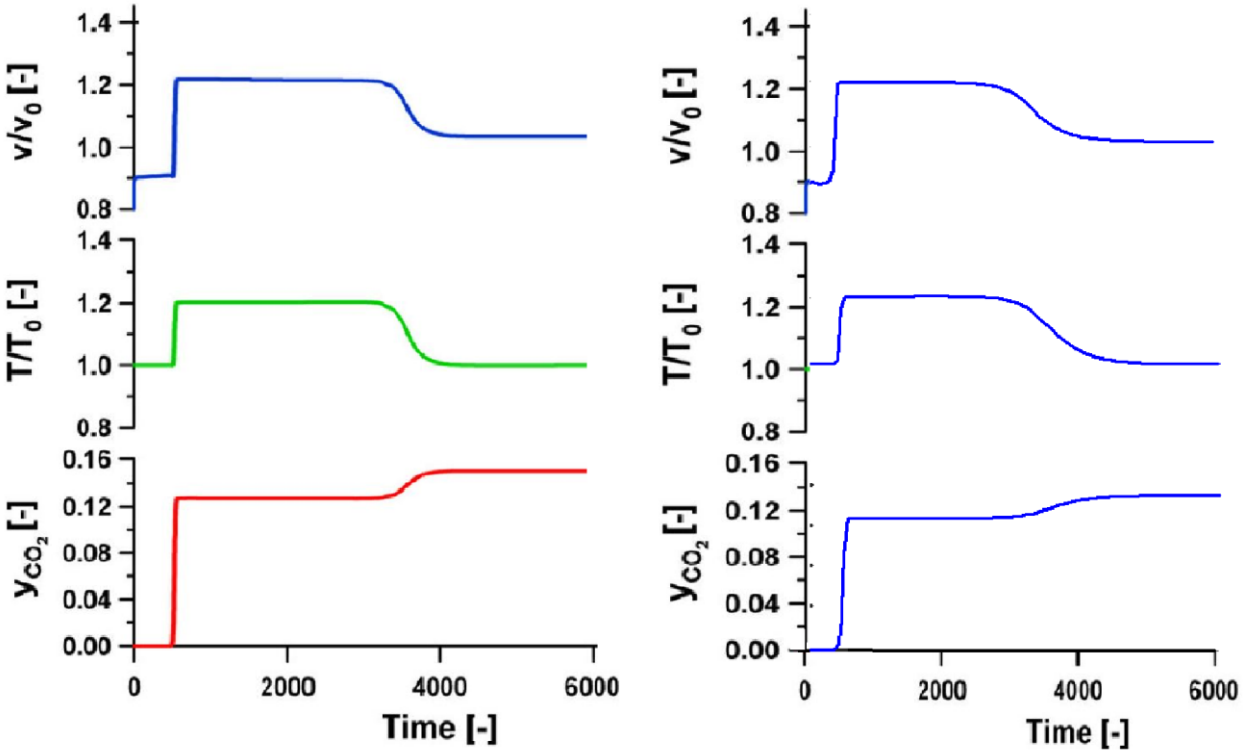

Figure 3.3 Velocity, temperature and composition breakthrough profiles for CO_2 at the exit of the adsorption bed (a) plots from reference literature [30]; (b) plots obtained from model developed in this study

3.8 Dynamic Column Breakthrough (DCB) Simulations

In a pressure swing adsorption process, the adsorption step plays an important role with respect to the optimisation of the process cycle. The adsorption dynamics and breakthrough behaviour of the bed according to the feed mixture is of extreme importance to have a properly designed PSA process. Hence, the simulation of dynamic column breakthrough experiment is considered as a first case study.

DCB setup is similar to that of an adsorption step with an open-open boundary condition. Both the carbon and zeolite columns are assumed to be initially saturated with 100% H_2 at P_H=30 bar and the COG feed stream at high pressure (P_H) is introduced into the carbon bed at the column inlet keeping both ends of the column open with a known flow velocity (v_{feed}). The pressure at the column outlet is assigned to the desired operating pressure. The outlet of carbon bed is connected to the inlet of zeolite bed. The columns are considered to be adiabatic (h_{in} = h_{out} = 0). The boundary conditions for breakthrough simulation are similar to that of adsorption step as listed in **Table 3.1**. The physical properties and operating parameters are listed in **Table 3.2**. The simulation results of the breakthrough profiles of gas concentrations (y), velocity (v), temperature (T) and pressure (P) of both activated carbon (AC) and zeolite (13X) columns are shown in **Figure 3.4** and **Figure 3.6** respectively.

There are two transitions seen in each of the **Figure 3.4** and **Figure 3.6**. The first is the sharp transition at a time of 600 seconds approximately for AC bed and 1000 seconds approximately for 13X bed representing the breakthrough of the gas fronts. The second transition at a time of 3500 seconds approximately for AC bed and 6550 seconds approximately for 13X bed corresponds to the elution of the heat front. An enlarged view of the second transition zone in the AC bed and 13X bed are shown in **Figure 3.5** and **Figure 3.7** respectively. The complete breakthrough of the gases are generally considered complete only after the heat fronts exit the column. At the end of the breakthrough, the amount of different gas components accumulated inside the columns can be calculated from the mass balance.

It can be clearly seen from the two transitions of the breakthrough experiments that for physical adsorption processes with relatively low molar adsorption heats, the effect of gas front due to mass balance is more significant while the effect of heat front due to energy balance is negligible. Hence, heat balance effects are of less importance in physisorption processes and mass balance is the one that dominates the process.

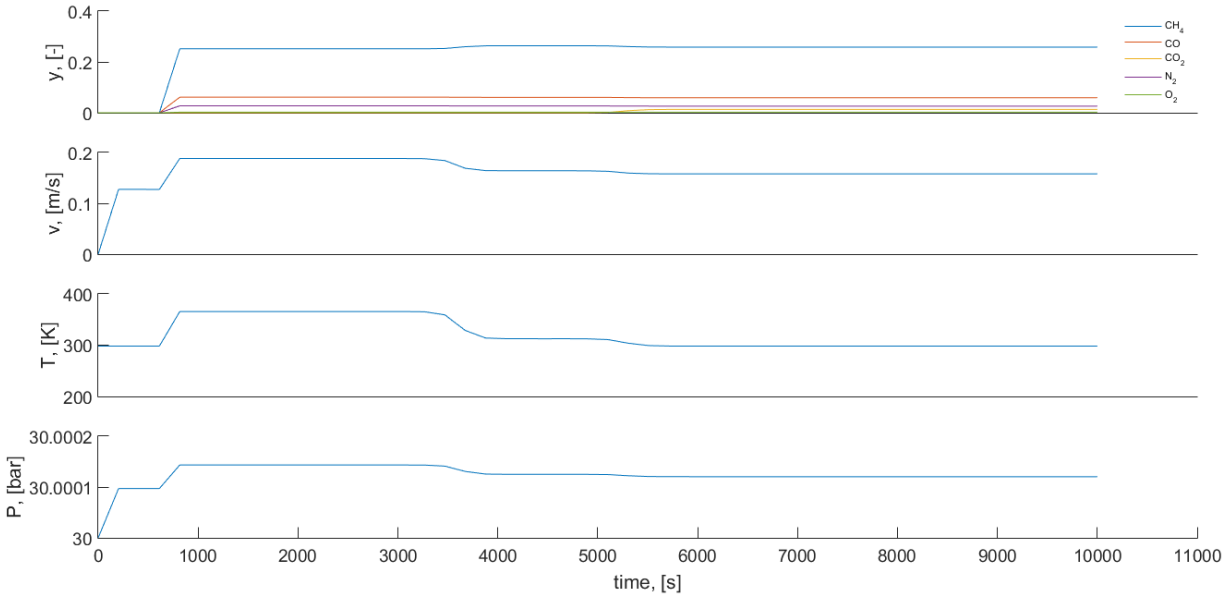

Figure 3.4 Composition, velocity, temperature and pressure breakthrough profiles for COG feed at the exit of AC adsorption bed

An enlarged view of the second transition zone in the bed from 3000 to 6000 sec is shown below.

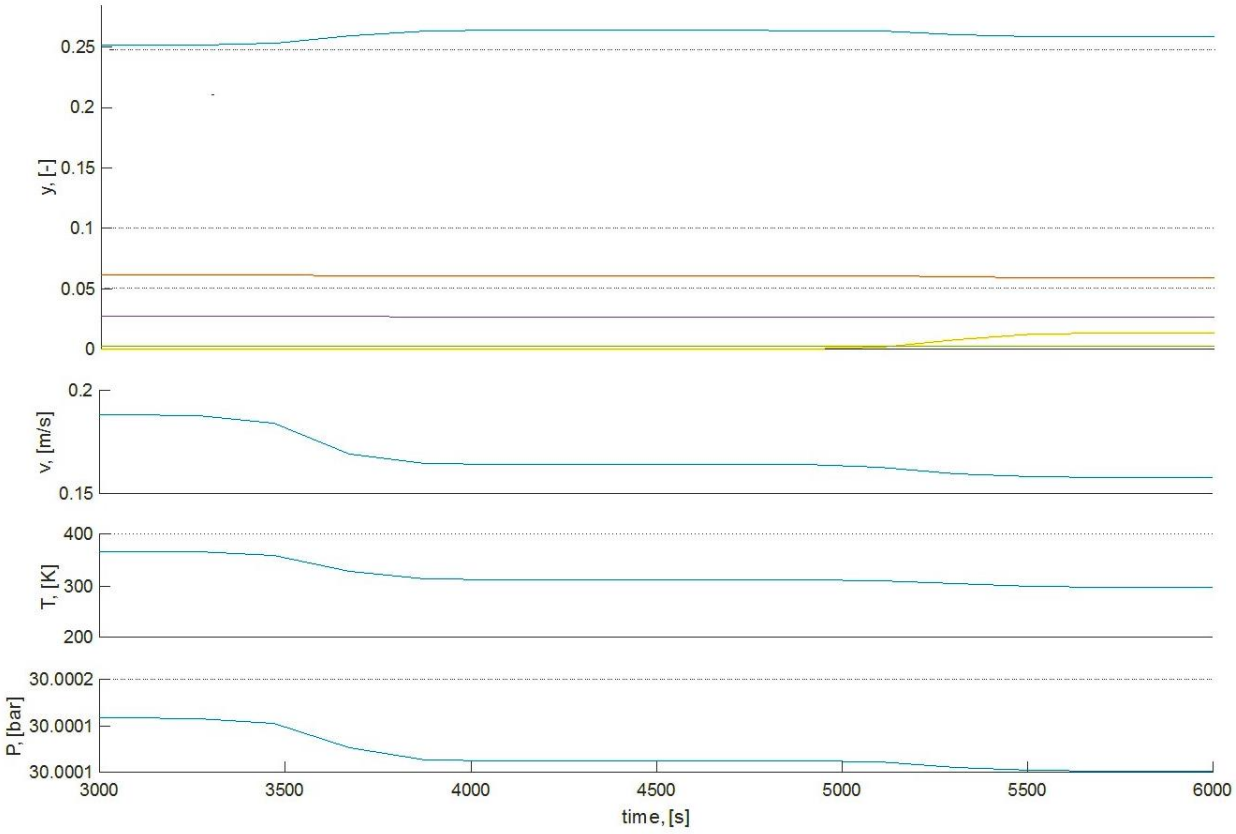

Figure 3.5 An enlarged view of the second transition zone in the AC bed due to the elution of heat front from **Figure 3.4**

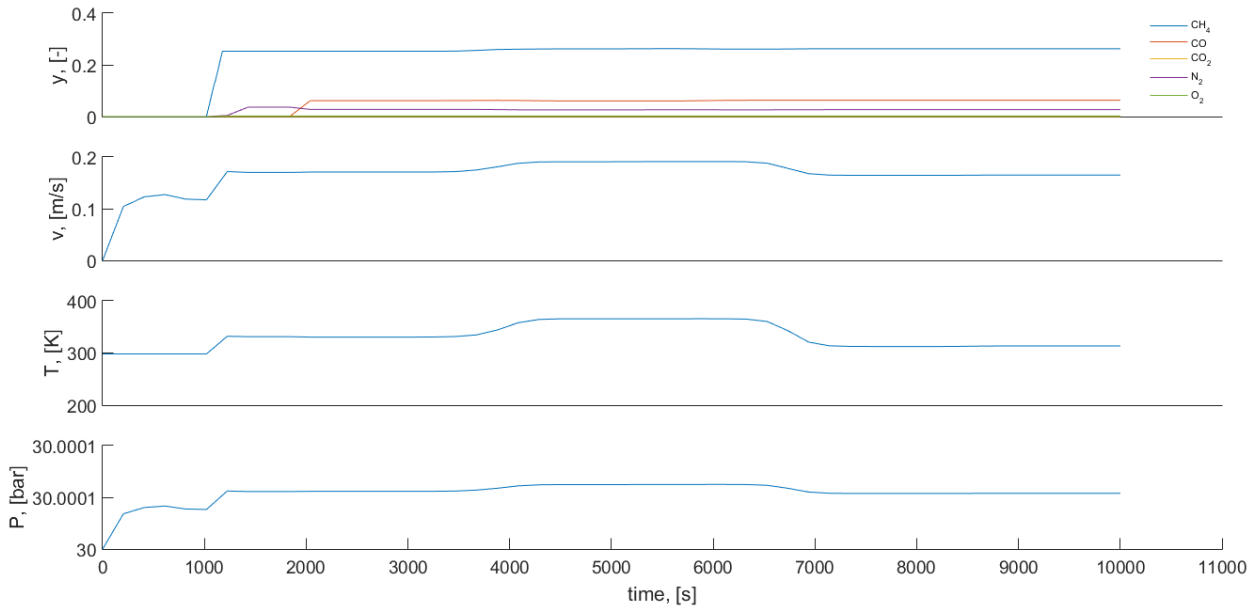

Figure 3.6 Composition, velocity, temperature and pressure breakthrough profiles for COG feed at the exit of 13X adsorption bed

An enlarged view of the second transition zone in the bed from 6000 to 8000 sec is shown below.

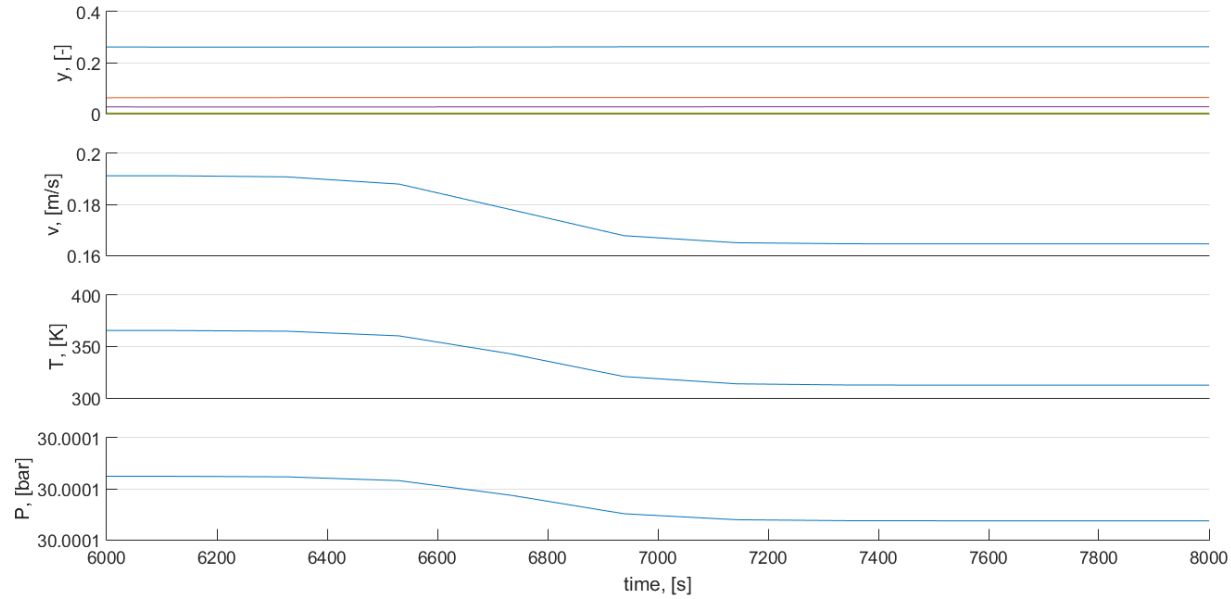

Figure 3.7 An enlarged view of the second transition zone in the 13X bed due to the elution of heat front from **Figure 3.6**

3.8.1 Variation of Breakthrough profile with Pressure

Simulations were run with different feed pressures and their effects on the breakthrough profiles for both carbon and zeolite beds are shown in **Figure 3.8** and **Figure 3.9** respectively. The sharpness of the wavefront profiles increase with the increase in pressure. As the feed pressure increases, the wavefront is moved down the bed thereby increasing the bed performance. This is due to the reason that the increase in feed pressure increases the adsorptive capacity of the bed according to the nature of adsorption equilibrium isotherm. This favourable behaviour continue to happen as the pressure increases, but becomes constant after a certain pressure wherein the adsorbent bed gets saturated with the maximum loading of adsorbate. It can also be seen that the effect of heat front in the second transition zone increases with increase in pressure.

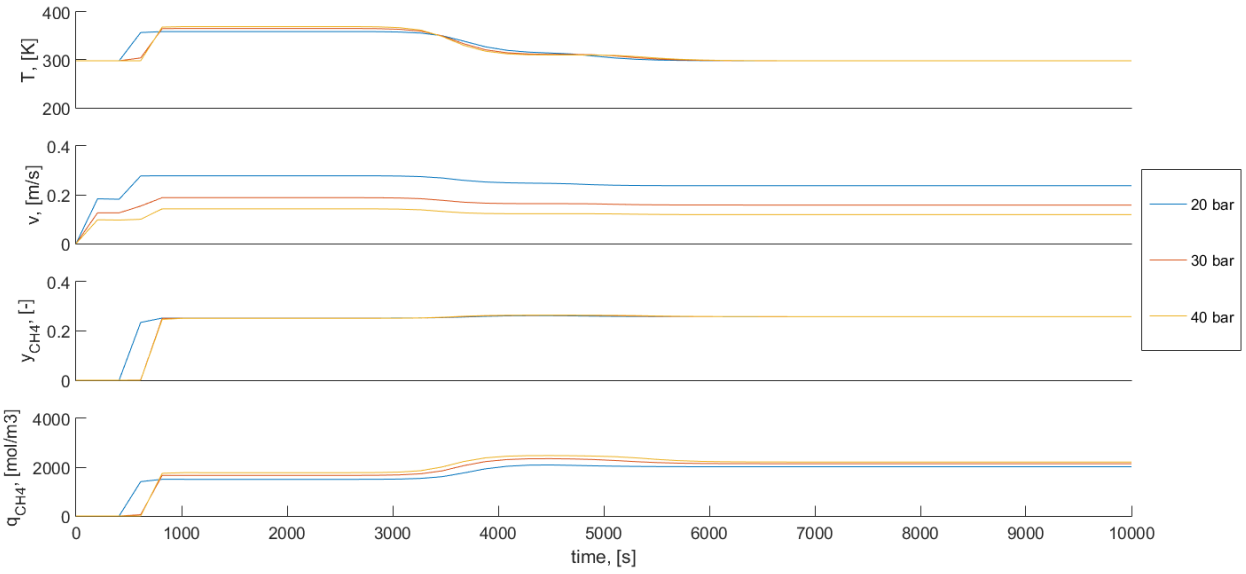

Figure 3.8 Temperature, velocity, composition and adsorption amount breakthrough profiles for CH_4 variation with pressure at the exit of AC adsorption bed

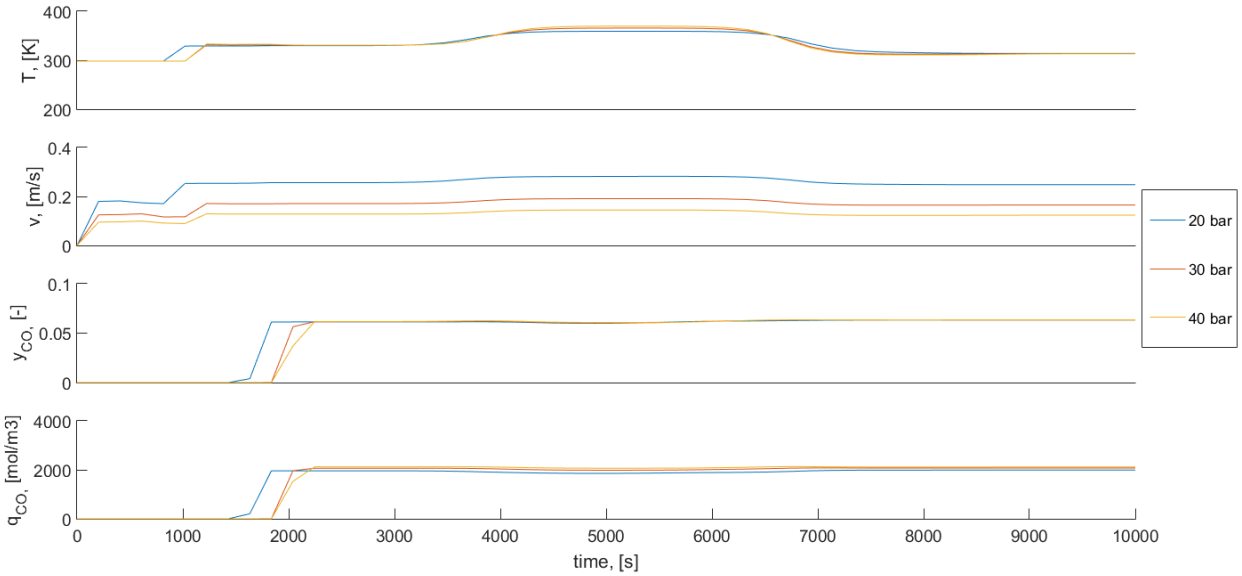

Figure 3.9 Temperature, velocity, composition and adsorption amount breakthrough profiles for CO variation with pressure at the exit of 13X adsorption bed

3.8.2 Variation of Breakthrough profile with Temperature

As the feed temperature increases, adsorption capacity of all the gas components in the bed decreases due to the reason that adsorption is an exothermic phenomenon. Simulations were run with different feed temperatures and their effects on the breakthrough profiles for both carbon and zeolite beds are shown in **Figure 3.10** and **Figure 3.11** respectively. The sharpness of the wavefront decrease with increase in temperature. As the feed temperature increases, the wavefront is moved up the bed, thereby affecting the performance of the bed with decreased adsorption capability. Also, it can be seen that the effect of heat front in the second transition also decreases with increased feed temperature.

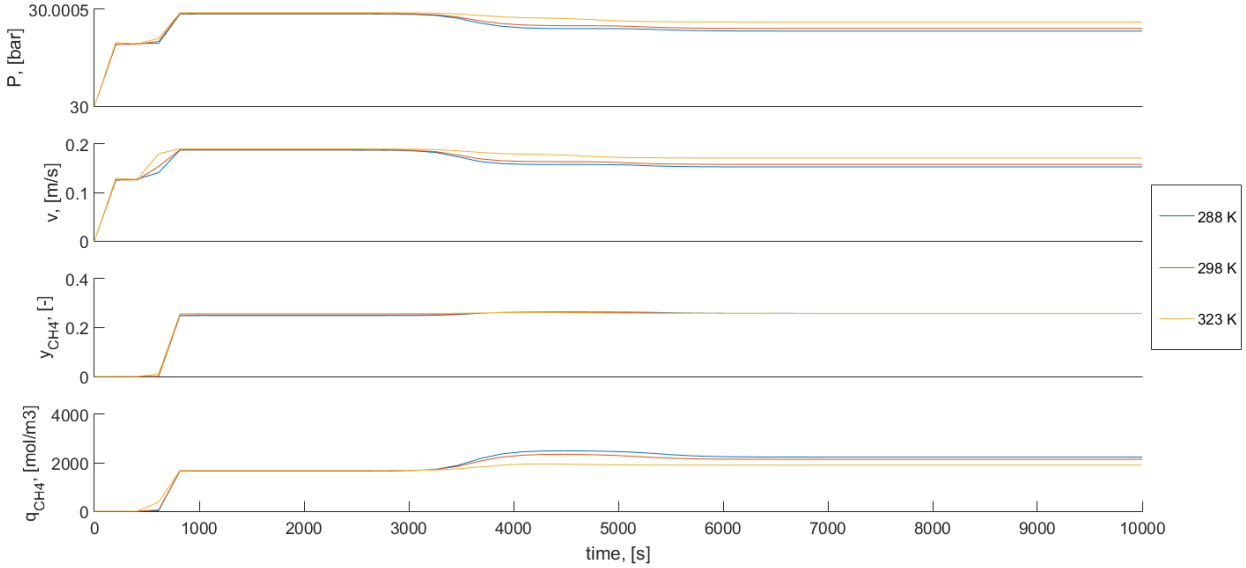

Figure 3.10 Pressure, velocity, composition and adsorption amount breakthrough profiles for CH_4 variation with temperature at the exit of AC adsorption bed

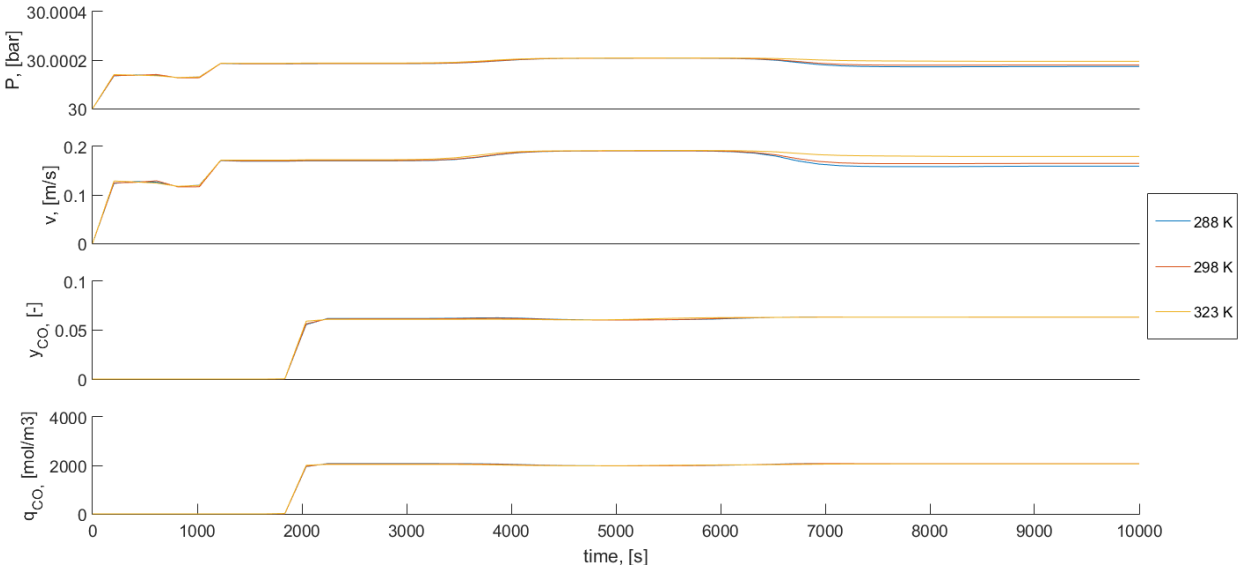

Figure 3.11 Pressure, velocity, composition and adsorption amount breakthrough profiles for CO variation with temperature at the exit of 13X adsorption bed

3.8.3 Variation of Breakthrough profile with Flow rate

As the feed flow rate increases, the time for interaction between the adsorbent material and adsorbate gas molecules decrease. Hence the adsorption capacity of the bed decreases. Simulations were run with different feed flow rates and their effects on the breakthrough profiles for both carbon and zeolite beds are shown in **Figure 3.12** and **Figure 3.13** respectively. The sharpness of the wavefront decrease with increase in flow rate. As the feed flow rate increases, the wavefront is moved up the bed, thereby affecting the performance of the bed with decreased adsorption capability. It can also be seen from the breakthrough results that the effect of heat front in the second transition increases with increase in feed flow rate.

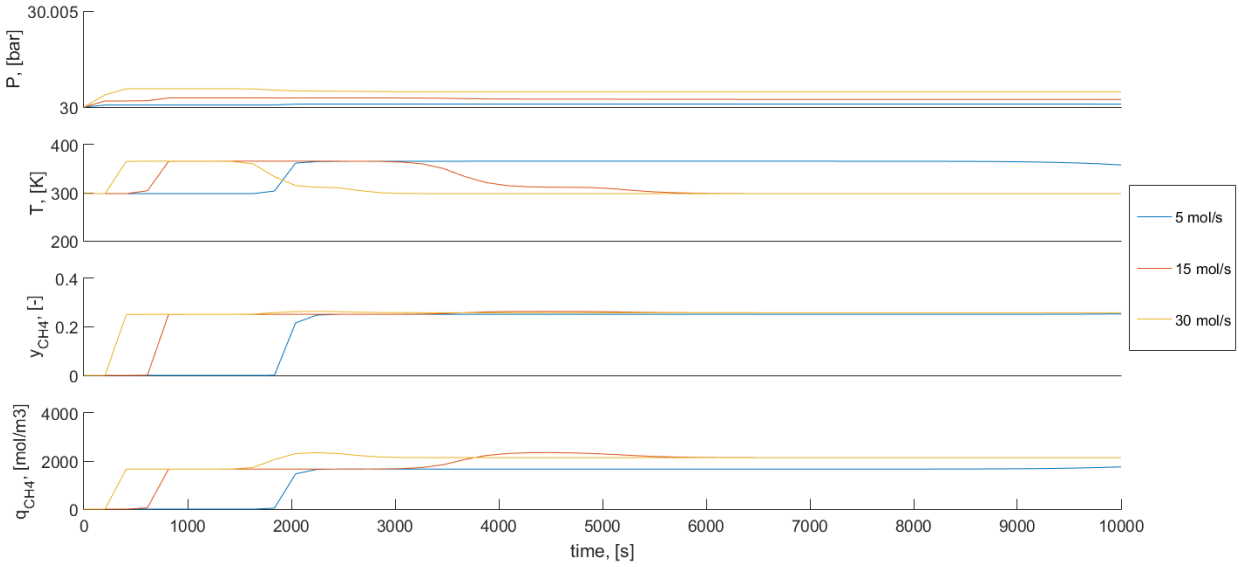

Figure 3.12 Pressure, temperature, composition and adsorption amount breakthrough profiles for CH_4 variation with feed flow rate at the exit of AC adsorption bed

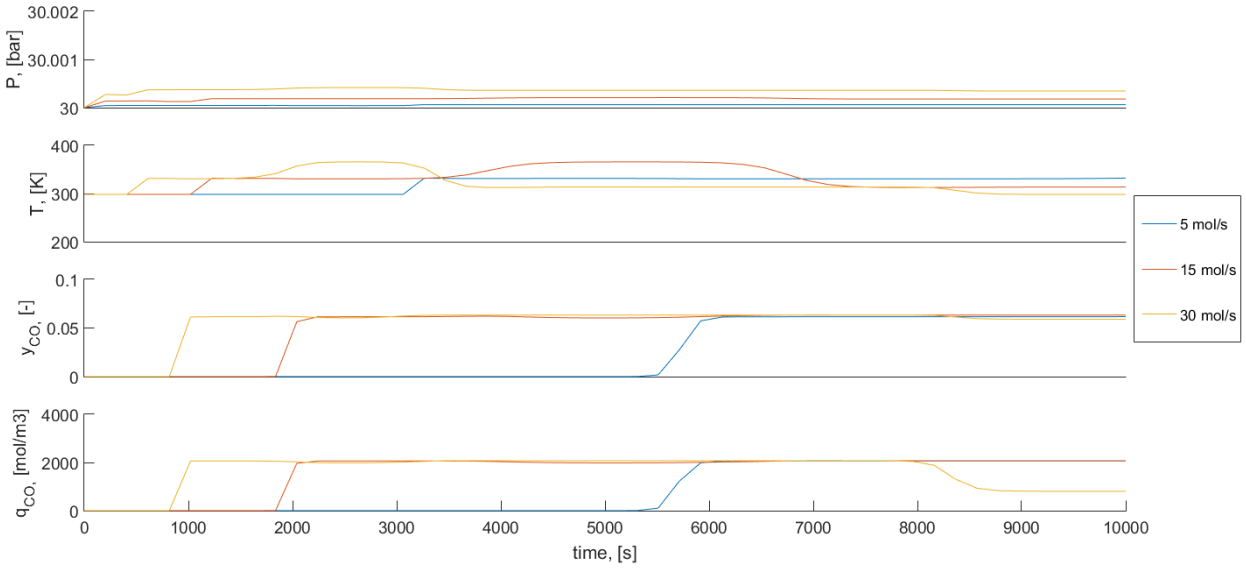

Figure 3.13 Pressure, temperature, composition and adsorption amount breakthrough profiles for CO variation with feed flow rate at the exit of 13X adsorption bed

3.9 Various steps of PSA cycle

The PSA cycle follows a number of steps that govern the performance of the process [14], [20], [43]–[45]. The steps followed by each column are shown in the form of a flow sheet in **Figure 3.14** for the PSA cycle proposed in the current work aiming at high purity H_2 with the best possible recovery.

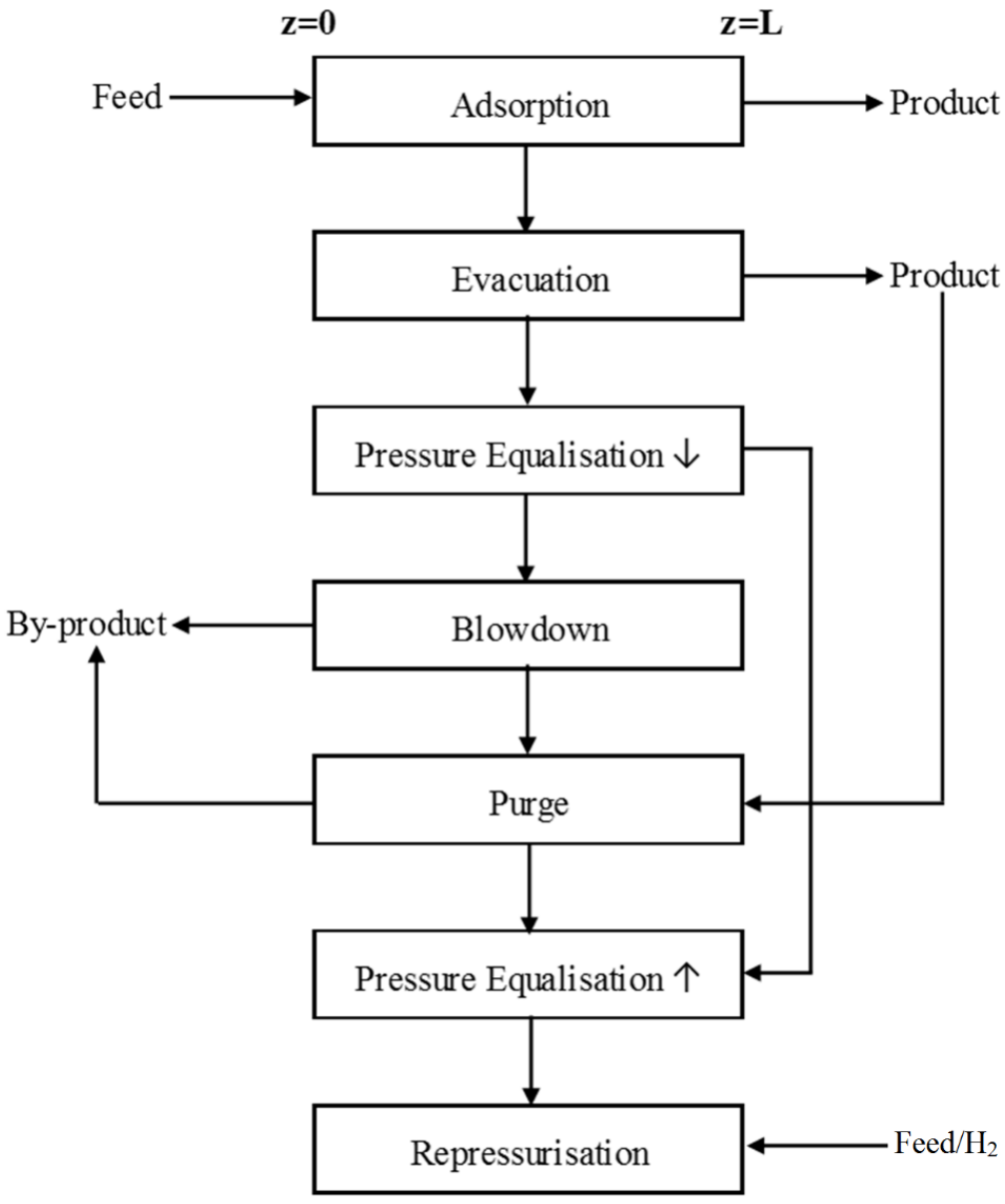

Figure 3.14 Flow sheet of different stages of PSA system

The PSA cycle consists of the following steps:

1. Adsorption:
   The COG feed enters the column and the product end (z=L) is opened. The heavier components are adsorbed while H_2 rich raffinate is collected from the product end.

2. Evacuation:
   The feed end (z=0) is closed and the column pressure is reduced to an intermediate pressure P_I by leaving the product end opened. The aim of this step is to collect as much H_2 as possible while retaining heavier components in the column.

3. Pressure Equalisation ↓:
   The feed end remain closed and the column pressure is reduced from P_I to an equalisation pressure P_{EQ} by connecting the product end to a column that is in its pressure equalisation ↑ step at that instant of time.

4. Blowdown:
   The product end is closed and CH_4 enriched product is collected from the feed end by decreasing the column pressure to P_L.

5. Purge:
   The H_2 rich evacuation product is depressurised to P_L and fed through the feed end. The remaining heavier components present in the column are purged out and collected at the product end so that the bed is free of heavier components.

6. Pressure Equalisation ↑:
   The product flow from the pressure equalisation ↓ step enters the column at the product end with the feed end closed hence increasing the pressure from P_L to P_{EQ}.

7. Repressurisation:
   COG/H_2 is introduced into the column at the product end with the feed end closed, thereby raising the column pressure to P_H and making the column ready for the next cycle of adsorption.

The state of the column at the end of a step is taken as the initial condition for the subsequent step. The sequence of steps is repeated until a cyclic steady state (CSS) is reached. Considering CSS behaviour, only one column each of activated column and zeolite LiX bed is simulated in time assuming all the other columns behave in the same manner.

3.10 PSA flowsheet overview for hydrogen sequestration from COG

The overview of the multibed PSA process for hydrogen separation from Coke Oven Gas is summarised as shown in **Figure 3.15**. The COG stream from the treatment plant is pressurised and passed through an activaed carbon adsorption bed in order to ensure complete removal of any sulfide compounds or heavy components still present in the feed. The clean feed is then passed through a sequence of adsorption columns filled with activated carbon and zeolite adsorbents. The H_2 rich product is collected as raffinate at high pressure while a CH_4 rich stream is collected as bottom product at low pressure.

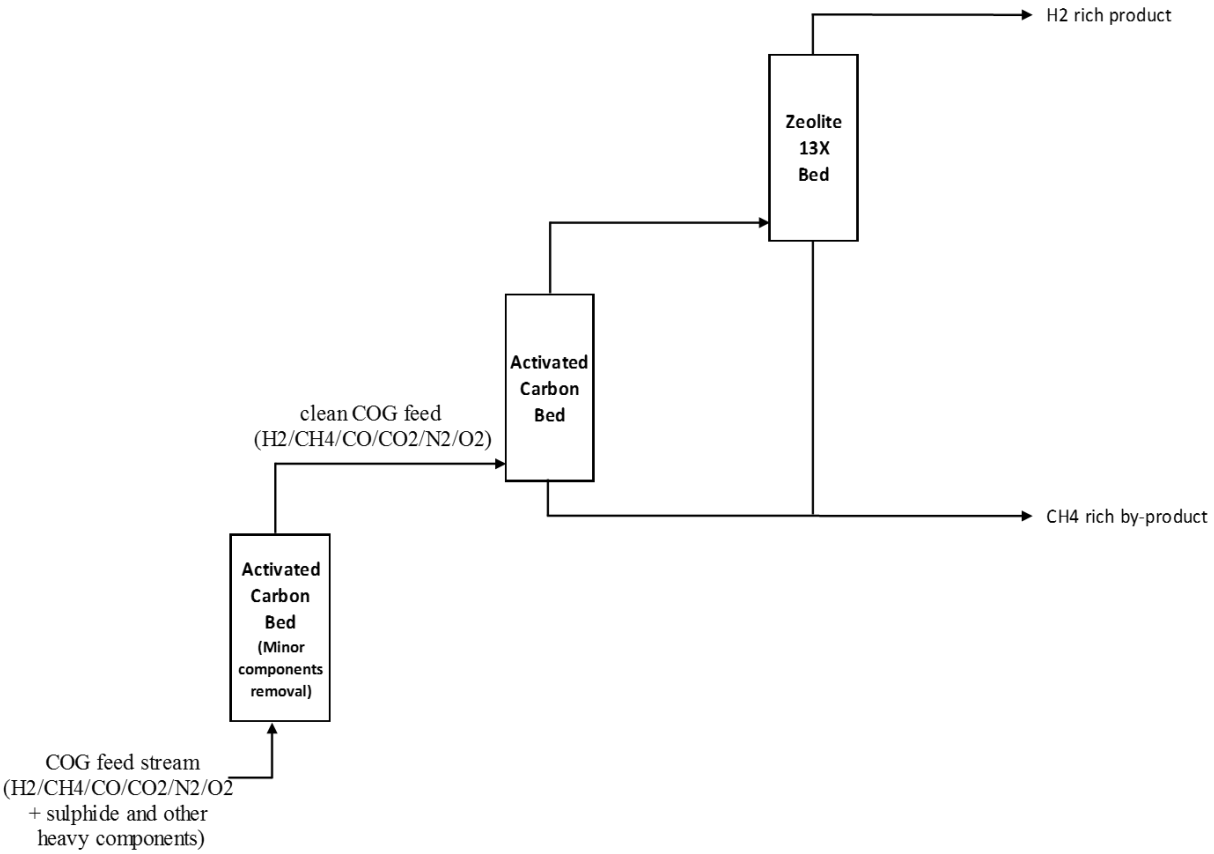

Figure 3.15 Schematic of the multi-bed PSA cycle for H_2 sequestration

Different parameters used in the PSA simulation are summarised in **Table 3.2**. The model developed in this chapter is optimized in the following chapter by performing rigorous parametric studies in order to achieve the best possible bed performance for the PSA process to produce high purity hydrogen product.

Table 3.2 Parameters used in PSA simulation

Parameter	Notation	Unit	Value	
Thermo-physical properties and constants				
Coke gas pressure	P_{COG}	bar	1	
Specific heat capacity of gas phase	C_{pg}	J mol^{-1} K^{-1}	30.7	
Fluid viscosity	μ	Pa s	1.72 x 10^{-5}	
Adiabatic constant	γ	-	1.4	
Thermal conductivity of gas	λ_g	J m^{-1} K^{-1} s^{-1}	0.09	
Universal gas constant	R	m^3 Pa mol^{-1} K^{-1}	8.314	
Column wall density	ρ_w	kg m^{-3}	7800	
Specific heat capacity of column wall	C_{pw}	J kg^{-1} K^{-1}	502	
Thermal conductivity of column wall	λ_w	J m^{-1} K^{-1} s^{-1}	16	
Compressor efficiency	η	-	0.72	
Adsorbent properties			**AC**	**LiX**
Column voidage	ε	-	0.4	0.4
Particle voidage	ε_p	-	0.433	0.64
Particle radius	r_p	mm	1	1
Pore radius	r_{pore}	Å	16.7	37.9
Adsorbent density	ρ_s	kg m^{-3}	850	1400
Specific heat capacity of adsorbent	C_{ps}	J kg^{-1} K^{-1}	1046	1757
Operating conditions				
High pressure	P_H	bar	30	
Low pressure	P_L	bar	1	
Equalisation pressure	P_{EQ}	bar	25	
Evacuation pressure	P_I	bar	15	
Feed rate	F_m	mol s^{-1}	150	
Feed temperature	T	K	298.15	
Ambient temperature	T_a	K	298.15	
Constants for dimensionless parameters				
Dimensionless pressure	P_0	bar	P_H	
Dimensionless temperature	T_0	K	T	
Dimensionless velocity	v_0	m s^{-1}	v_{feed}	
Dimensionless adsorption amount	q_0	mol m^{-3}	$q_{s,H2}$	
Dimensionless length	z_0	m	L	
Dimensionless time	t_0	s	L/v_0	

Chapter 4

Parametric Studies & Model Optimisation

An extensive parameter study was performed to understand the effects of various factors on the performance of the multi-bed PSA process developed for high purity hydrogen production from coke oven gas. Aiming for hydrogen purity greater than 99.999% with the best possible recovery, simulations were run by varying the parameters such as purge to feed ratio, feed temperature, pressure, particle size, number of pressure equalisations, duration of different steps, feed flow rate, flow direction, carbon to zeolite ratio. Each of the simulation yields a cyclic steady state with H_2 purity and recovery values.

4.1 Purge-to-feed variation

The purge step in PSA is a desorption step in which the adsorbents are regenerated by desorbing the adsorbed gas components that remain in the adsorbent bed after blowdown step by passing a purge stream at low pressure. Generally a fraction of the H_2 product is used to purge out the remaining gas components from the bed. The amount of purge stream required affects the product purity as well as its recovery. As the purge amount increases, purging becomes more effective in removing the gas components from the adsorbent. This effective regeneration results in more impurities being adsorbed by the bed in the next cycle of adsorption thereby increasing the H_2 product purity. So in principle, more the purge stream better the product purity is. At the same time, since purging is done using the pure H_2 product, increase in purge amount decreases the recovery of the product. Usually, the purge amount specification for PSA is given by the purge-to-feed ratio which is the ratio between the amount of H_2 used as purge stream to the amount of H_2 present in the feed and this ratio should never be greater than one.

Simulations were run with different purge-to-feed ratio. The results are presented in **Figure 4.1** showing the effects of this ratio on product purity and recovery. It can be seen that as this ratio increases, the product purity increases as well, but the recovery decreases. The rate of purity increase is much slower compared the rate of decrease in recovery. From these results, we can observe that if the purge-to-feed ratio is too low, the purity of the product gets affected and if the ratio is too high, the recovery of the product is reduced. The ideal purge-to-feed ratio is identified during the optimisation of the process which will be discussed in the later part of study.

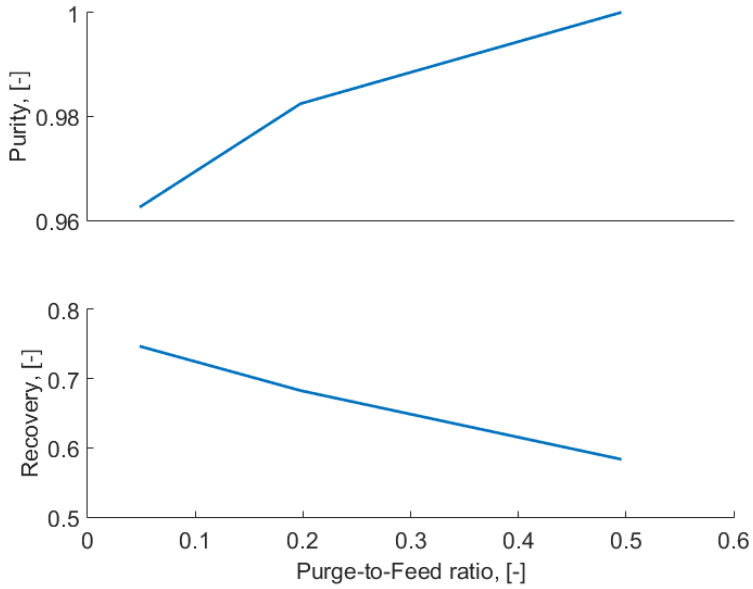

Figure 4.1 Effect of purge-to-feed ratio variation on bed performance

Table 4.1 Simulation conditions for the study on purge-to-feed variation

P/F (-)	P_H (bar)	P_L (bar)	Time (sec)						f_{Ads} (mol/s)	f_{Purge} (mol/s)	$f_{Repress}$ (mol/s)
			Ads	Evac	PEQ	BD	Purge	Repress			
0.05	30	1	420	50	50	100	100	250	15	2	30
0.20	30	1	420	50	50	100	400	250	15	2	30
0.5	30	1	420	50	50	100	1000	250	15	2	30

4.2 Feed flow rate variation

As the feed flow rate increases, the time for interaction between the adsorbent material and adsorbate gas molecules decrease. Hence the adsorption capacity of the bed decreases resulting in more impurities being present in H_2 product leading to decreased product purity with an increase in recovery. Simulations were run with different feed flow rates and their results are presented in **Figure 4.2**. It can be seen that with the increase in feed flow rate, the recovery of the product increases while its purity decreases. Hence, lower the feed flow rate better the adsorptive capacity and hence the product purity. But, the feed flow rate cannot be two low as it affects the productivity of the process. The suitable feed flow rate is identified during the optimisation of the process which will be discussed in the later part of study.

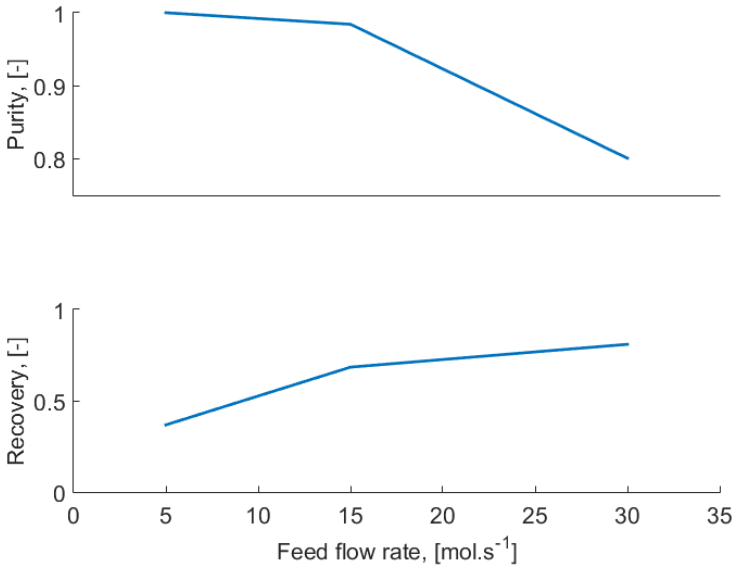

Figure 4.2 Effect of feed flow rate variation on bed performance

Table 4.2 Simulation conditions for the study on feed flow rate variation

f_{Ads} (mol/s)	P_H (bar)	P_L (bar)	Time (sec)						f_{Purge} (mol/s)	$f_{Repress}$ (mol/s)
			Ads	Evac	PEQ	BD	Purge	Repress		
5	30	1	420	50	50	100	400	250	2	30
15	30	1	420	50	50	100	400	250	2	30
30	30	1	420	50	50	100	400	250	2	30

4.3 Particle size variation

Particle size affects the bed performance in two ways. If other parameters remain constant, a smaller particle size leads to higher bed pressure drop as shown in **Figure 4.4**.According to the linear driving force (LDF) equation, the LDF coefficient (k_{LDF}) is inversely proportional to the square of the particle radius. Hence for a smaller particle, the mass transfer rate is high. Also, smaller particle means higher surface area of adsorption for the same amount of adsorbent material in the bed. Both these properties increase the adsorptive capacity of the adsorbent, hence increasing the product purity. But along with the impurities, the adsorption of H_2 also increase resulting in decreased recovery of H_2 product.

Simulation studies were performed with various particle sizes and their results are shown in **Figure 4.3**. It can be seen from the results that with larger particles, pressure drop is low and recovery is high but the product purity decreases. The effect of particle size on product purity is significant for both bulk separation and purification processes.

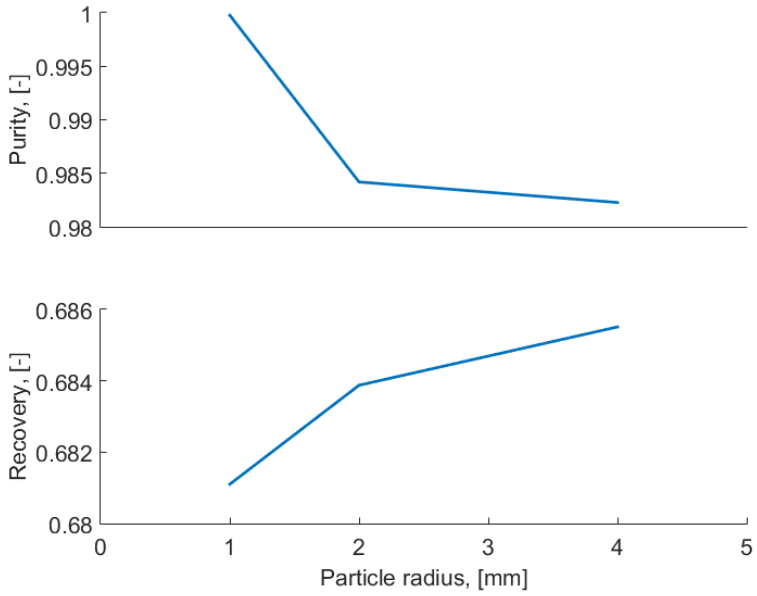

Figure 4.3 Effect of particle size variation on bed performance

Table 4.3 Simulation conditions for the study on particle size variation

r_p (mm)	P_H (bar)	P_L (bar)	Time (sec)						f_{Ads} (mol/s)	f_{Purge} (mol/s)	$f_{Repress}$ (mol/s)
			Ads	Evac	PEQ	BD	Purge	Repress			
1	30	1	420	50	50	100	400	250	15	2	30
2	30	1	420	50	50	100	400	250	15	2	30
4	30	1	420	50	50	100	400	250	15	2	30

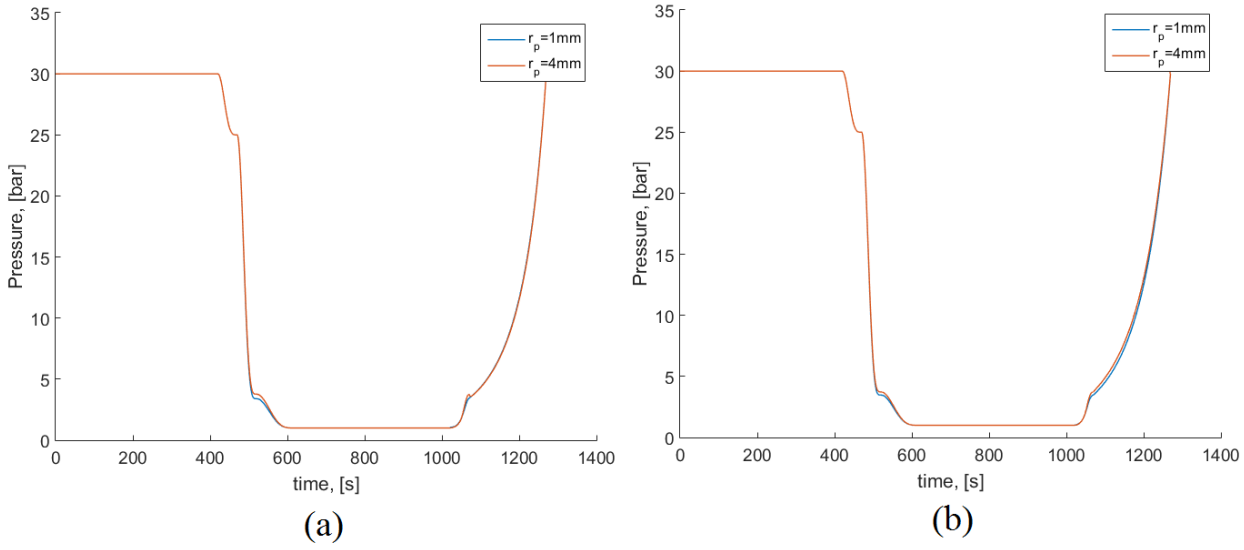

Figure 4.4 Pressure variation along the cycle with varied particle size (a) AC (b) 13X

4.4 Column Length-to-Particle Diameter ratio variation

Simulations were run with different column length-to-particle diameter ratios and their results are shown in **Figure 4.5**. The effects of axial dispersion which is a function of particle diameter are minimized as the column length-to-particle diameter ratio increases. This improves the adsorptive capacity of the bed leading to better adsorption of impurities resulting in higher product purity. But along with the impurities, the adsorption of H_2 also increases leading to decreased product recovery.

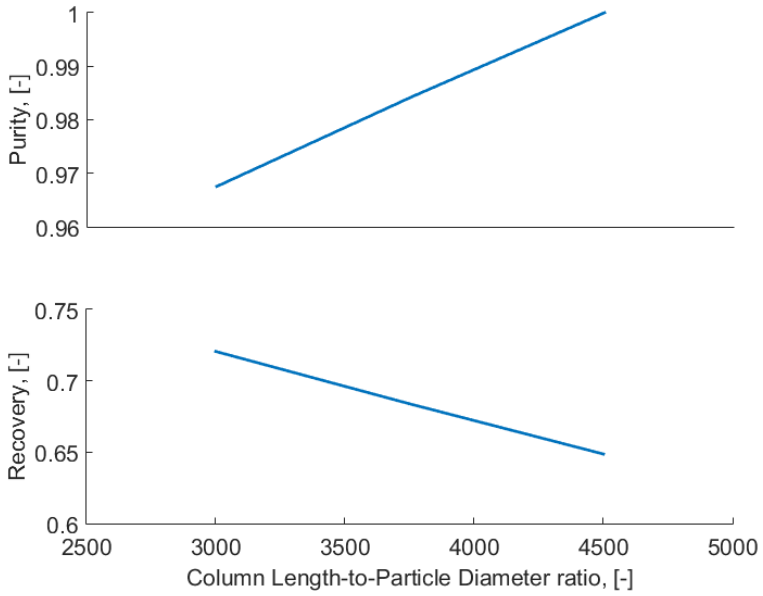

Figure 4.5 Effect of column length-to-particle diameter ratio variation on bed performance

Table 4.4 Simulation conditions for the study on column length-to-particle diameter ratio variation

L/D ratio (-)	P_H (bar)	P_L (bar)	Time (sec)						f_{Ads} (mol/s)	f_{Purge} (mol/s)	$f_{Repress}$ (mol/s)
			Ads	Evac	PEQ	BD	Purge	Repress			
24	30	1	420	50	50	100	400	250	15	2	30
30	30	1	420	50	50	100	400	250	15	2	30
36	30	1	420	50	50	100	400	250	15	2	30

4.5 Carbon-to-Zeolite ratio variation

Simulations were run with different carbon-to-zeolite ratios and their results are shown in **Figure 4.6**. As the ratio of carbon increases, the purity and recovery of the product decreases. Since zeolite has better selectivity for some impurity components as compared to that of activated carbon, decreasing zeolite ratio beyond a certain limit degrades the adsorption capacity thereby affecting process performance.

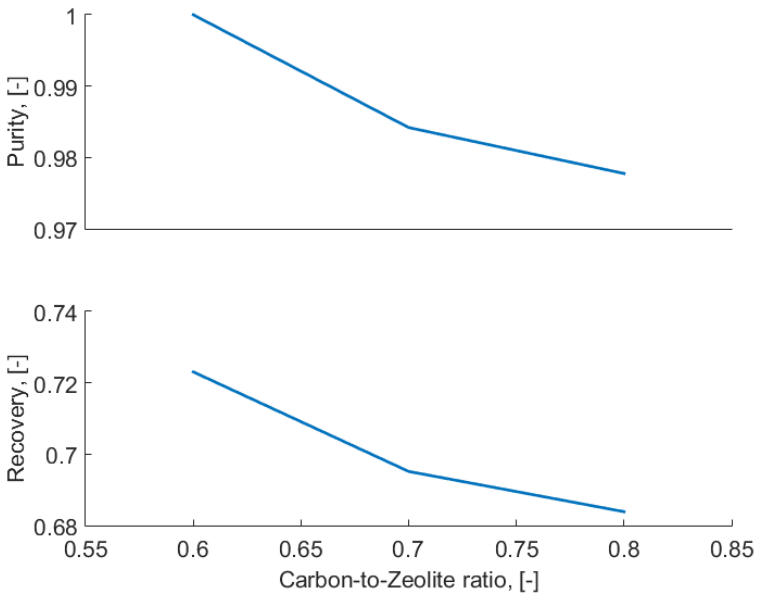

Figure 4.6 Effect of Carbon-to-Zeolite ratio variation on bed performance

Table 4.5 Simulation conditions for the study on Carbon-to-Zeolite ratio variation

AZ ratio (-)	P_H (bar)	P_L (bar)	Time (sec)						f_{Ads} (mol/s)	f_{Purge} (mol/s)	$f_{Repress}$ (mol/s)
			Ads	Evac	PEQ	BD	Purge	Repress			
0.6	30	1	420	50	50	100	400	250	15	2	30
0.7	30	1	420	50	50	100	400	250	15	2	30
0.8	30	1	420	50	50	100	400	250	15	2	30

4.6 Feed pressure variation

For a constant feed flow, an increase in feed pressure increases the adsorption capacity of the bed according to the nature of adsorption equilibrium isotherm. Simulations were run with different feed pressures. The results are presented in **Figure 4.7** showing the effects of feed pressure variation on product purity and recovery. It can be seen that as the feed pressure increases, the product purity increases due to increased adsorption capacity of the adsorbents. There is a decrease in product recovery due to the reason that along with impurities the adsorption of H_2 also increases.

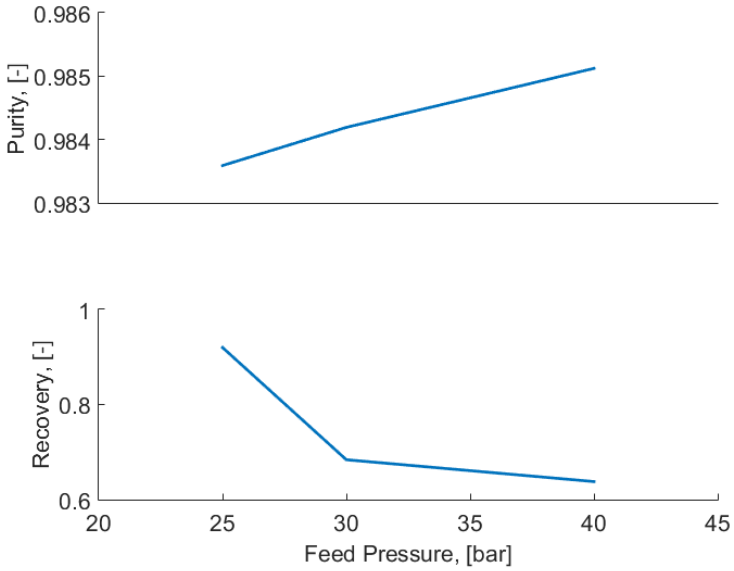

Figure 4.7 Effect of feed pressure variation on bed performance

Table 4.6 Simulation conditions for the study on feed pressure variation

P_H (bar)	P_L (bar)	Time (sec)						f_{Ads} (mol/s)	f_{Purge} (mol/s)	$f_{Repress}$ (mol/s)
		Ads	Evac	PEQ	BD	Purge	Repress			
25	1	420	50	50	100	400	250	15	2	30
30	1	420	50	50	100	400	250	15	2	30
40	1	420	50	50	100	400	250	15	2	30

4.7 Feed Temperature variation

As the feed temperature increases, adsorption capacity of all the gas components in the bed decreases. This is due to the reason that adsorption is an exothermic phenomenon. Simulation studies were performed with various feed temperatures and their results are shown in **Figure 4.8**. It can be seen from the results that with the increase in feed temperature the product purity decreases with an increase in recovery.

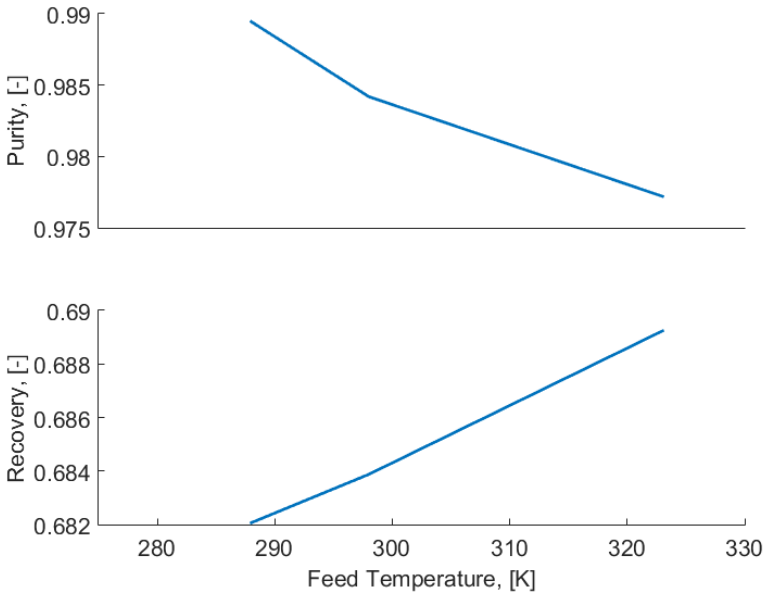

Figure 4.8 Effect of feed temperature variation on bed performance

Table 4.7 Simulation conditions for the study on feed temperature variation

T (K)	P_H (bar)	P_L (bar)	Time (sec)						f_{Ads} (mol/s)	f_{Purge} (mol/s)	$f_{Repress}$ (mol/s)
			Ads	Evac	PEQ	BD	Purge	Repress			
288	30	1	420	50	50	100	400	250	15	2	30
298	30	1	420	50	50	100	400	250	15	2	30
323	30	1	420	50	50	100	400	250	15	2	30

4.8 Evacuation Pressure variation

After high pressure adsorption step, as the pressure is decreased H_2 being the least adsorptive component comes out of the column first. Hence as the evacuation pressure decreases, the H_2 recovery increases. But after a certain pressure drop along with H_2, the impurities also get desorbed and starts coming out of the column thereby decreasing product purity. Simulations were run with different evacuation pressures. The results are presented in **Figure 4.9** showing the effects of evacuation pressure variation on product purity and recovery.

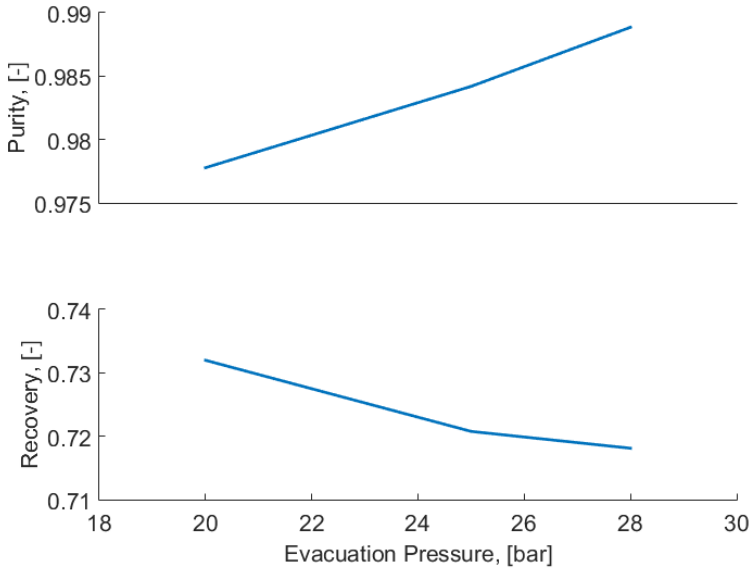

Figure 4.9 Effect of evacuation pressure variation on bed performance

Table 4.8 Simulation conditions for the study on evacuation pressure variation

P_{Evac} (bar)	P_H (bar)	P_L (bar)	Time (sec)						f_{Ads} (mol/s)	f_{Purge} (mol/s)	$f_{Repress}$ (mol/s)
			Ads	Evac	PEQ	BD	Purge	Repress			
20	30	1	420	50	50	100	400	250	15	2	30
25	30	1	420	50	50	100	400	250	15	2	30
28	30	1	420	50	50	100	400	250	15	2	30

4.9 Number of Pressure Equalisations variation

After a bed has completed its purge step and another bed has completed its evacuation step, instead of blowing down the second bed directly, the two beds can be connected to each other through their product ends in order to equalise their pressures. Thus the first bed is partially pressurised with gas from the outlet of the second bed. After the pressure equalisations, the two beds are disconnected and the first bed is further repressurised with feed/H_2 gas while the second bed is vented to complete the blowdown. The pressure equalisation step conserves energy because the low pressure bed is partially pressurised with the compressed gas from the high pressure bed. But, with increase in the number of pressure equalisations, the number of connecting columns that are needed for the pressure equalisation also increases, thereby increasing the capital cost. Based on these considerations, pressure equalisation steps are incorporated in the PSA process.

Simulations were run with different number of pressure equalisations and their results are presented in **Figure 4.10**. It can be seen that increase in the number of pressure equalisations favour product recovery as more H_2 is passed from the high pressure to low pressure column instead of being blown down as bottom product. But along with H_2, impurities are also passed across the column thereby affecting the purity of H_2 product.

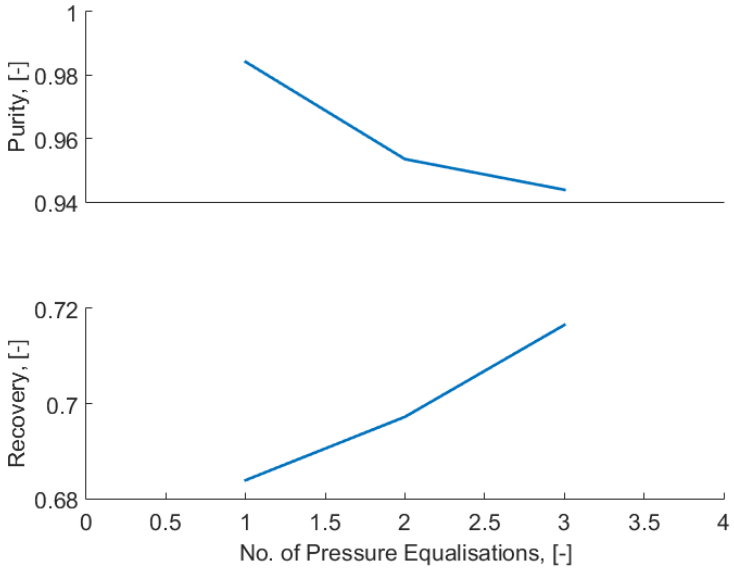

Figure 4.10 Effect of no. of pressure equalisations variation on bed performance

Table 4.9 Simulation conditions for the study on no. of pressure equalisations variation

No. of PEQs (-)	P_H (bar)	P_L (bar)	Time (sec)						f_{Ads} (mol/s)	f_{Purge} (mol/s)	$f_{Repress}$ (mol/s)
			Ads	Evac	PEQ	BD	Purge	Repress			
1	30	1	420	50	50	100	400	250	15	2	30
2	30	1	420	50	50	100	400	250	15	2	30
3	30	1	420	50	50	100	400	250	15	2	30

4.10 Blowdown time variation

During the blowdown step, the CH_4 rich impurities are blown down as bottom product. **Figure 4.11** shows the simulation results corresponding to different time allocations to the blowdown step. It can be seen that the increase in blowdown time allows for more impurities to desorb from the bed thereby aiding better regeneration of the column. This increases the product purity as the adsorption capacity increases with a decrease in product recovery as H_2 adsorption also increases.

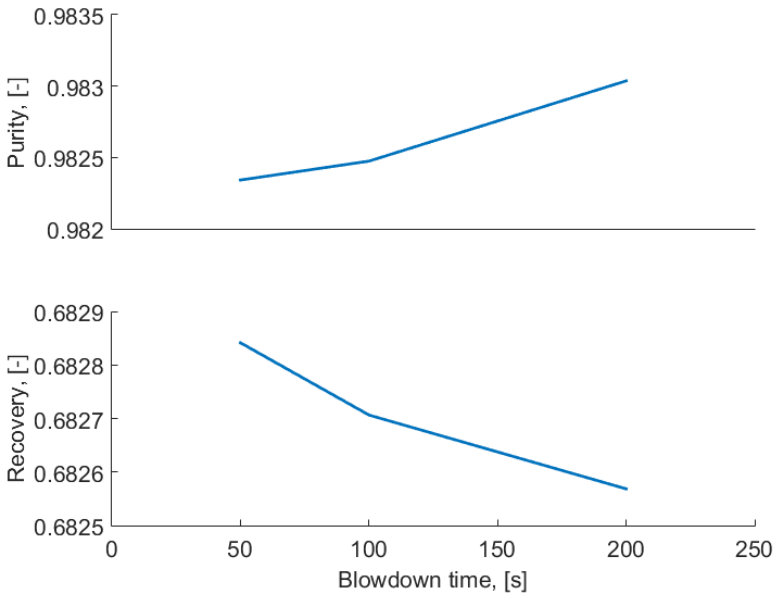

Figure 4.11 Effect of blowdown time variation on bed performance

Table 4.10 Simulation conditions for the study on blowdown time variation

t_{BD} (s)	P_H (bar)	P_L (bar)	Time (sec)					f_{Ads} (mol/s)	f_{Purge} (mol/s)	$f_{Repress}$ (mol/s)
			Ads	PEQ	Evac	Purge	Repress			
50	30	1	420	50	50	400	250	15	2	30
100	30	1	420	50	50	400	250	15	2	30
200	30	1	420	50	50	400	250	15	2	30

4.11 Pressure Equalisation time variation

Simulations were run with different pressure equalisation times and their results are presented in **Figure 4.12**. It can be seen that increase in pressure equalisation time favours product recovery as more H_2 is passed from high pressure to low pressure column instead of being blown down as bottom product. But along with H_2, impurities also pass across the column thereby affecting the purity of H_2 product.

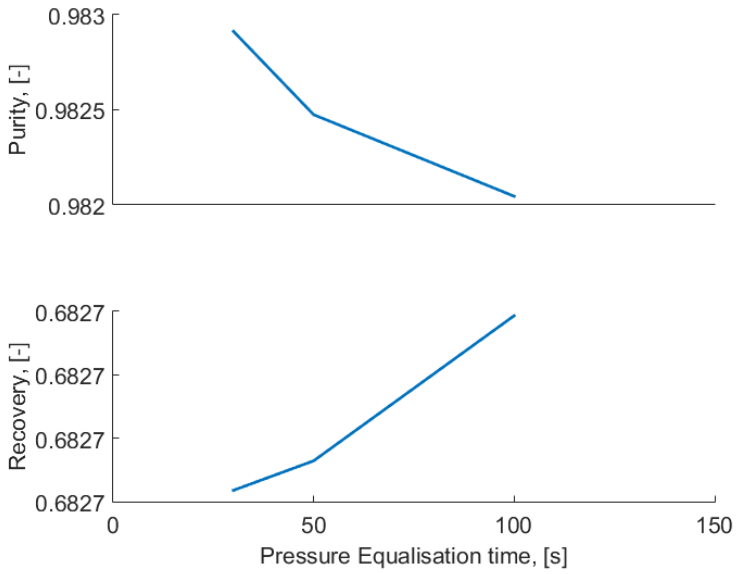

Figure 4.12 Effect of pressure equalisation time variation on bed performance

Table 4.11 Simulation conditions for the study on pressure equalisation time variation

t_{PEQ} (s)	P_H (bar)	P_L (bar)	Time (sec)					f_{Ads} (mol/s)	f_{Purge} (mol/s)	$f_{Repress}$ (mol/s)
			Ads	Evac	BD	Purge	Repress			
30	30	1	420	50	100	400	250	15	2	30
50	30	1	420	50	100	400	250	15	2	30
100	30	1	420	50	100	400	250	15	2	30

4.12 Evacuation time variation

Simulations were run with different evacuation times. The results are presented in **Figure 4.13** showing the effects of evacuation time variation on product purity and recovery. The increase in evacuation time allows for more H_2 to desorb from the bed, thereby increasing product recovery. But along with H_2, other impurities also pass through the column thereby affecting the product purity.

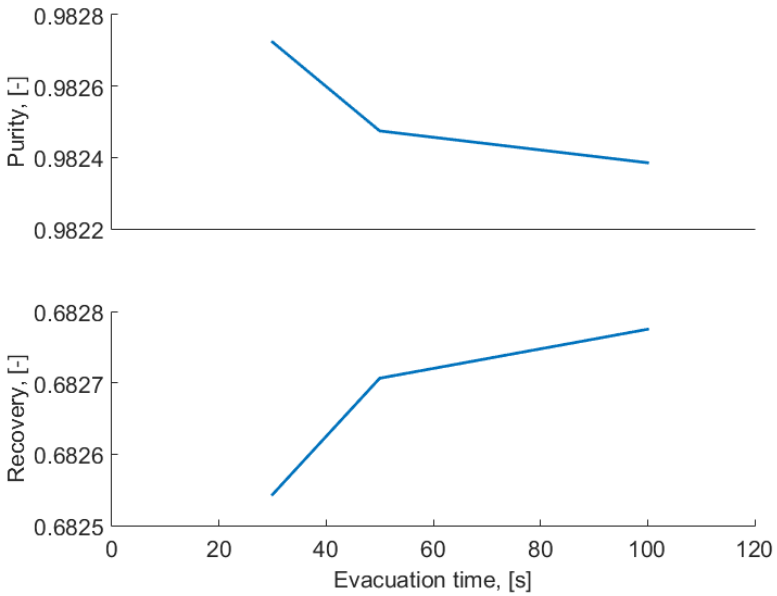

Figure 4.13 Effect of evacuation time variation on bed performance

Table 4.12 Simulation conditions for the study on evacuation time variation

t_{Evac} (s)	P_H (bar)	P_L (bar)	Time (sec)					f_{Ads} (mol/s)	f_{Purge} (mol/s)	$f_{Repress}$ (mol/s)
			Ads	PEQ	BD	Purge	Repress			
30	30	1	420	50	100	400	250	15	2	30
50	30	1	420	50	100	400	250	15	2	30
100	30	1	420	50	100	400	250	15	2	30

4.13 Number of Discretization volumes variation

Number of discretization volumes (N) is related to the role of relatively sharp concentration profiles, therefore both the bed performance factors i.e. purity and recovery are sensitive to the number of discretization volumes. Simulations were run with different discretization volumes and their results are presented in **Figure 4.14**. It can be seen that the difference in performance values with variation in discretization volumes after N=30 is very small (<0.1%) and there is almost no variation after N=50. Hence, N=50 is chosen as the discretization volume for all the simulations.

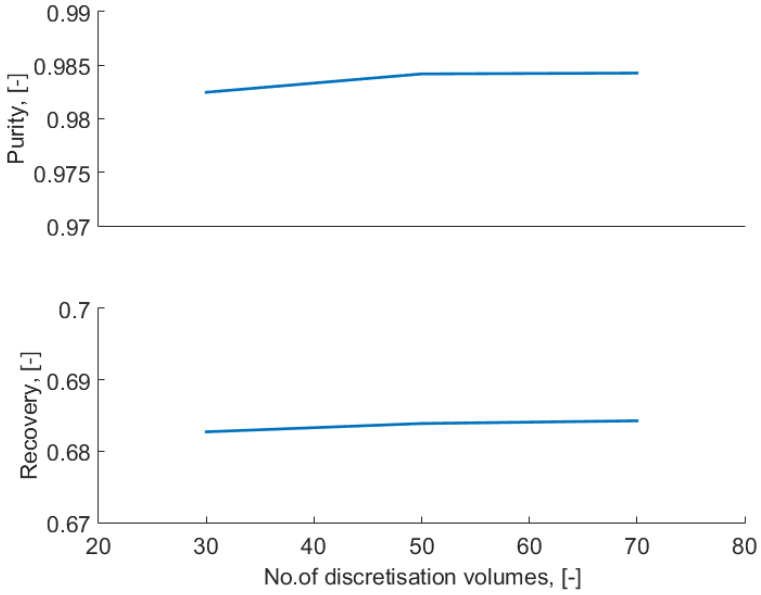

Figure 4.14 Effect of no. of discretization volumes on bed performance

Table 4.13 Simulation conditions for the study on no. of discretization volumes variation

N	P_H	P_L	Time (sec)						f_{Ads}	f_{Purge}	$f_{Repress}$
(-)	(bar)	(bar)	Ads	Evac	PEQ	BD	Purge	Repress	(mol/s)	(mol/s)	(mol/s)
30	30	1	420	50	50	100	400	250	15	2	30
50	30	1	420	50	50	100	400	250	15	2	30
70	30	1	420	50	50	100	400	250	15	2	30

Through various parameter studies performed above, a better understanding of the effects of different parameters on the performance of PSA cycle is achieved. With the knowledge gained from this chapter on parametric studies, several optimisations are performed using the combined effects of different parameters in order to obtain the best possible performance for the PSA process and their results are presented in the next chapter.

Chapter 5

Results and Discussion

A set of four two-columned pressure swing adsorption cycle with counter-current purge and repressurisation with one pressure equalisation step is developed for producing high purity hydrogen from coke oven gas. The step configuration of the final optimised PSA cycle is shown in **Figure 5.1**

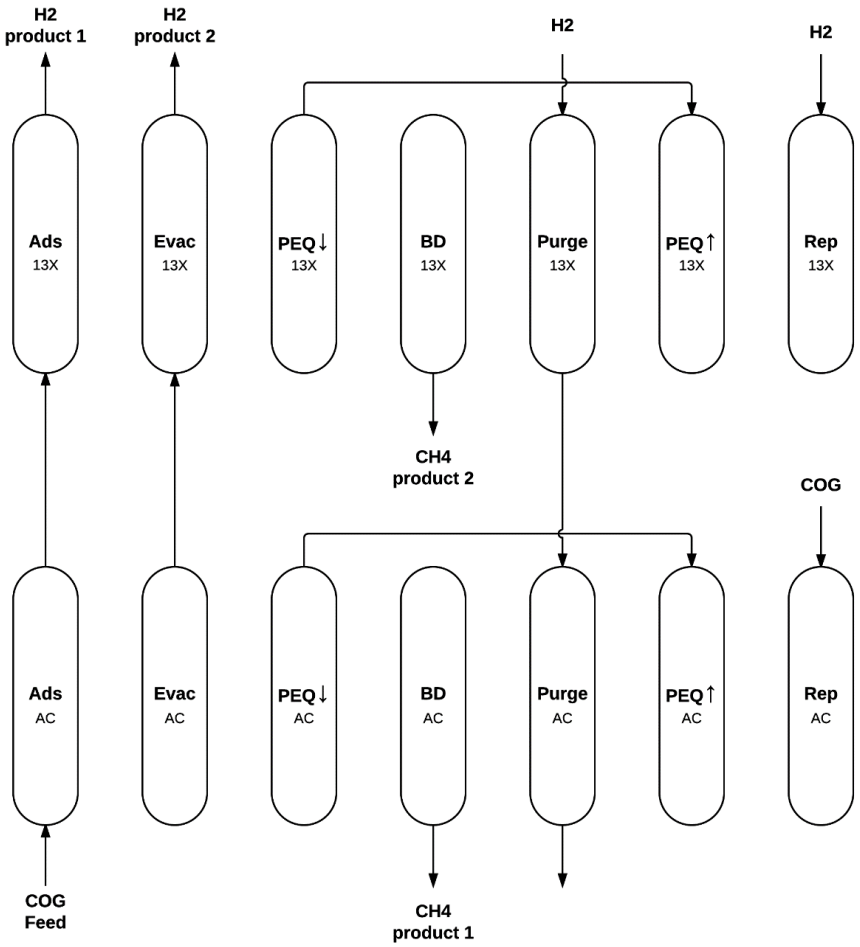

Figure 5.1 Step configuration of a four-column PSA cycle (Ads –adsorption; Evac –evacuation; PEQ↓ –pressurising pressure equalisation; BD –blowdown; PEQ↓ –pressurising pressure equalisation; Rep –Repressurisation)

The pressurised coke oven gas feed enters the carbon (AC) column wherein the adsorption of the impurities takes place in the bed. The hydrogen enriched outflow of the carbon bed is connected to the feed end of zeolite (13X) column in which the adsorption process continues wherein high purity hydrogen with desired feed quality requirements for fuel cell vehicles (FCVs) is obtained at the product end. After the adsorption step, the feed end of carbon column is closed leaving the product end open. Evacuation takes place in the bed and hydrogen being the weakly adsorbed species comes out of the column first which is passed subsequently through the zeolite column and high purity hydrogen is collected at the zeolite column's product end. After the evacuation step is over, the feed end of zeolite column is also closed. This step is followed by the depressurising pressure equalisation step in which the product ends of each of carbon and zeolite columns are connected to the product ends of their counterpart columns respectively which are in their pressurising pressure equalisation step. The gas components move from the high pressure to low pressure columns resulting in pressurisation of the low pressure columns. After the pressure equalisation step is over, the columns are enriched with CH_4 which are blown down through the product ends during the depressurisation step to atmospheric pressure. After depressurisation, still some impurities remain in the bed due to their equilibrium condition. Now, the feed ends of both the columns are open. A part of the H_2 product is used as purge stream and passed through the product end of the zeolite column and the outflow from the zeolite feed end enters the product end of carbon column. During this step, the remaining impurities present in the bed are pushed out of the columns and collected at the feed end of carbon column. At the end of purge step, the impurities are removed from the beds and thus the columns are regenerated. The purge step is followed by the pressurising pressure equalisation step in which the high pressure gas components from the depressurising columns are passed through the product ends of the columns with the feed ends closed resulting in pressurisation of the columns. The repressurisation step follows the pressure equalisation step in which a part of high purity H_2 product is used to further pressurise the columns to make the beds ready for the next cycle of adsorption.

The sequence of steps was repeated until the simulation reaches a cyclic steady state (CSS). Strictly considering, a CSS condition is reached only when there is no change in the column profiles of all the state variables after each step for two consecutive cycles. To check whether the simulation reached its cyclic steady state or not, the performance parameters i.e. the purity and recovery of H_2 product for five consecutive cycles were compared. It was considered that a CCS condition is reached when the difference of the purity and recovery of H_2 for the five consecutive cycles were both less than 10^{-6}.

Cycle timing for the 4 columns in parallel for each of carbon and zeolite beds is shown in **Figure 5.2** depicting the relative duration for each step. At every instant of time, there is atleast one column in the adsorption step thereby making the product outflow continuous. Also, the depressurising and pressurising pressure equalisation steps must be connected in time thereby ensuring proper pressure transfer from high pressure to low pressure columns. Numerically, a single column is simulated in time while the connecting steps are stored.

Duration (sec) / Column No.	50	100	150	200	250	300	350	400	450	500	550	600	650	700	750	800	850	900	950	1000	1050	1100	1150	1200	1250	1300	1350	1400
1	Ads															Evac	PEQ↓	BD	Purge					PEQ↑	Rep			
2	Ads	Evac	PEQ↓	BD	Purge					PEQ↑	Rep					Ads												
3	Ads							Evac	PEQ↓	BD	Purge					PEQ↑	Rep							Ads				
4	Purge		PEQ↑	Rep						Ads													Evac	PEQ↓	BD	Purge			

Figure 5.2 Cycle timing diagram of 4-columns (each for AC and 13X) for the 14 step PSA cycle with counter-current H_2 purge

The pressure profile at the outlet end of a carbon and zeolite columns over a cycle for the four column PSA unit at the cyclic steady state condition is shown in **Figure 5.3**.

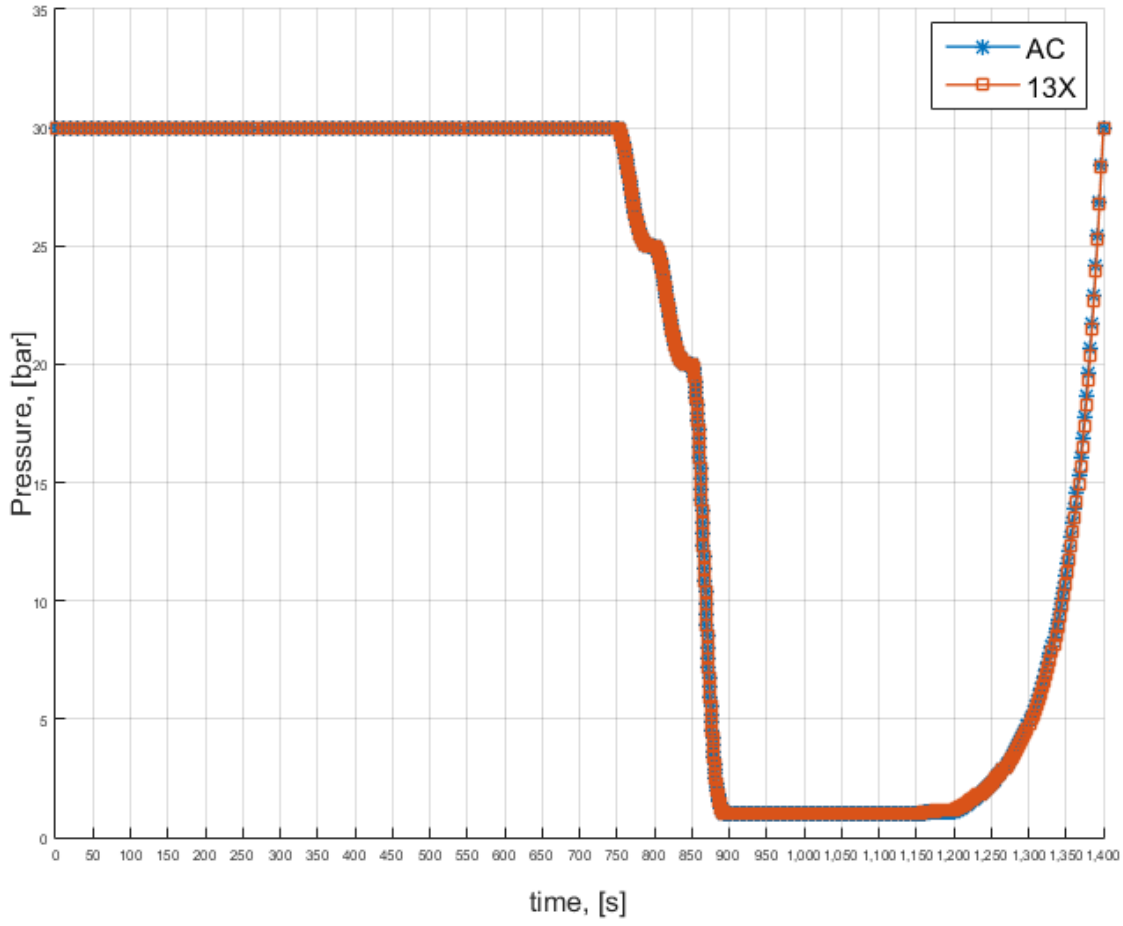

Figure 5.3 Pressure profiles at the outlet end of a carbon and zeolite column over a cycle at the cyclic steady state of the 4-column (each for AC and 13X) H_2 PSA unit

Pareto plots are made for three different feed pressures (P_H) by varying the feed flow rate as shown in **Figure 5.4**. Moving from one point on any Pareto curve to another on the same curve results in the improvement of one performance parameter, either purity or recovery at the expense of the other. It can be seen that as we move along the right of a parity curve, the purity of the product increases with the compensation in product recovery. Also from the Pareto plots for three different feed pressures, it can be visualised that as the feed pressure increases a desired purity could be achieved with much better recovery than that of a lower feed pressure.

Also, the Pareto plots could be used as a tool for sensitivity analysis. It shows how the outcome of simulation varies with small deviations of various boundary conditions. In this case, the analysis is performed by slightly varying the feed pressure and feed flow rate to observe their effects on the purity and recovery of the product. It can be seen that the model accurately captures the small changes in boundary conditions during the simulation of the process to give precise results of their effects on process performance.

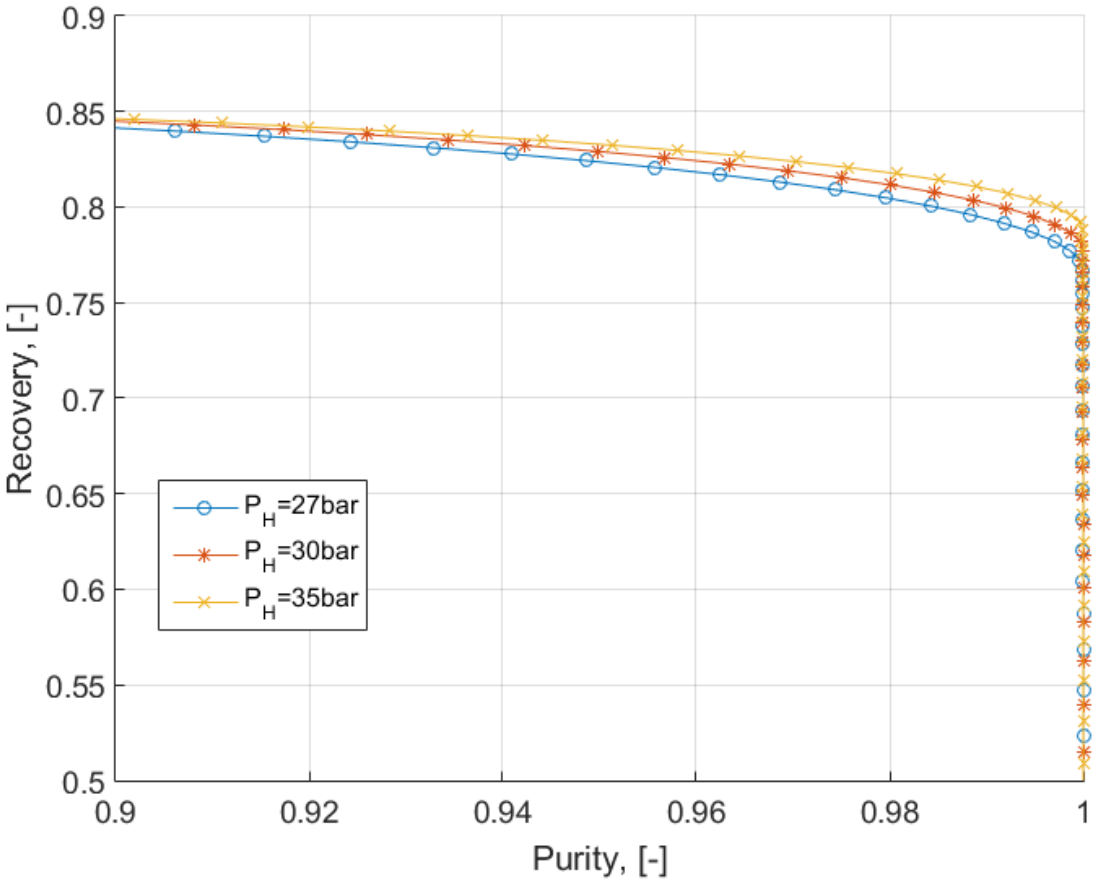

Figure 5.4 Pareto curves for the optimisation problem of simultaneously increasing purity and recovery

A comparison of hydrogen purity and recovery of the PSA system with changes in purge-to-feed ratio is shown in **Figure 5.5**. It can be seen that as the purge-to-feed ratio increases, the purity of the product increases with a decrease in product recovery. At the P/F ratio of 0.18, the hydrogen product reaches the desired purity of 99.999+% with a recovery of 78%. Further increase of the P/F ratio results in unwanted loss of product recovery which should be avoided for better overall performance of the process.

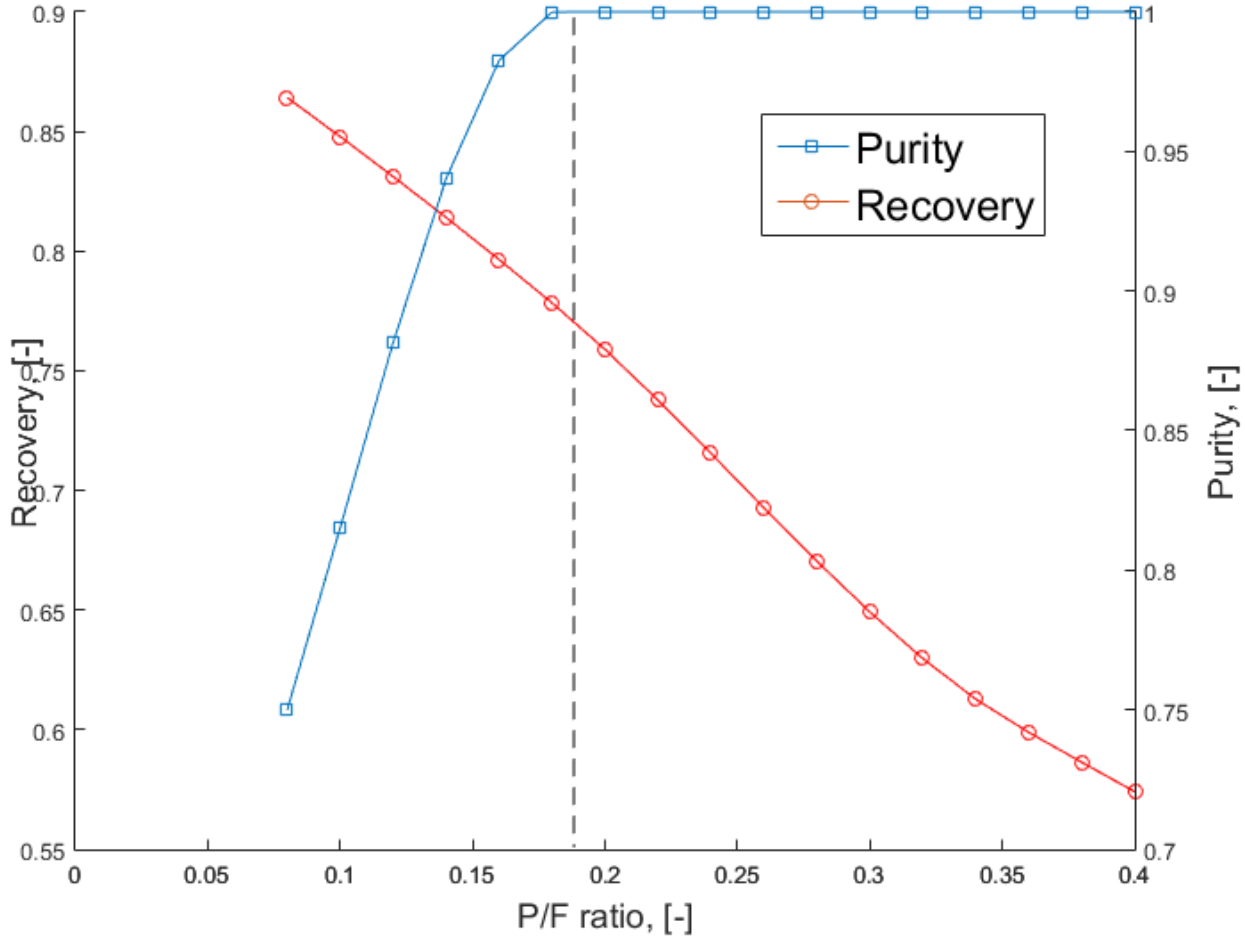

Figure 5.5 Comparison of hydrogen purity and recovery of the PSA system with different purge-to feed ratio

The final optimised values of different parameters used in improving the performance of the PSA simulation process are summarised in **Table 5.1**

Table 5.1 Optimised values of the parameters used in PSA simulation

Parameter	Value
Operating conditions:	
Feed Pressure, P_H (bar)	30
Blowdown Pressure, P_L (bar)	1
Equalisation Pressure, P_{EQ} (bar)	20
Evacuation Pressure, P_{Evac} (bar)	25
Feed Temperature, T (K)	298
Feed flow rate, $F_{m,feed}$ (mol s^{-1})	30
Purge flow rate, $F_{m,purge}$ (mol s^{-1})	10
Repress flow rate, $F_{m,repress}$ (mol s^{-1})	16
Purge-to-Feed ratio, P/F (-)	0.18
Bed Properties:	
Total column length, L (m)	15
Inner column radius, r_{in} (m)	0.350
Outer column radius, r_{out} (m)	0.355
Carbon-to-Zeolite ratio, AZ (-)	0.5
Particle radius, r_p (mm)	2
Duration of each step:	
Adsorption time, t_{Ads} (s)	750
Evacuation time, t_{Evac} (s)	50
Equalisation time, t_{PEQ} (s)	50
Blowdown time, t_{BD} (s)	50
Purge time, t_{purge} (s)	250
Repress time, t_{Rep} (s)	200

Gas phase concentrations in the carbon and zeolite beds at the start and end time of each step during the PSA cycle is shown in **Figure 5.6** and **Figure 5.7** respectively.

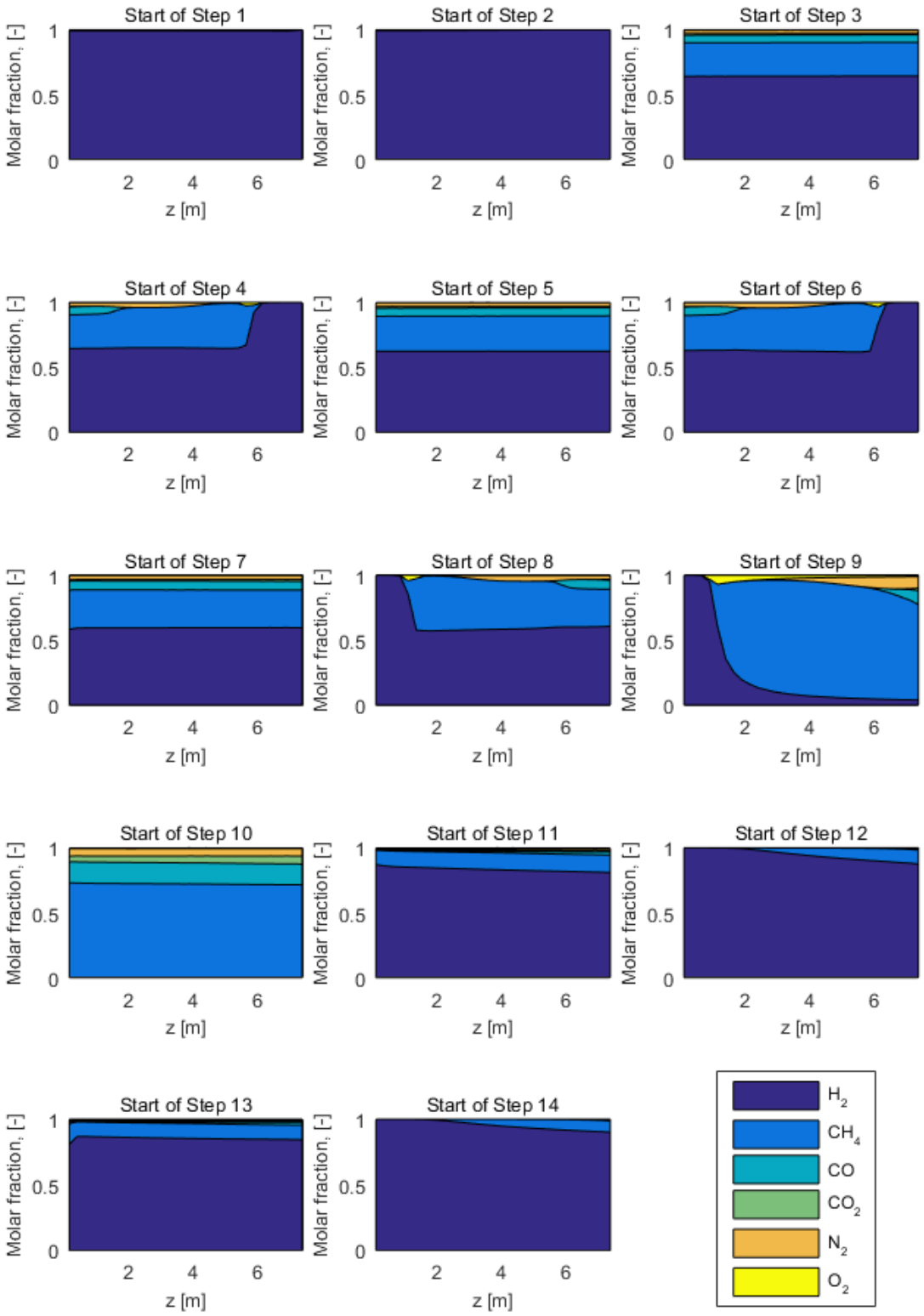

Figure 5.6 Gas phase concentrations in the bed at the start of each step during the PSA cycle. Steps: (1) AC Adsorption; (2) 13X Adsorption; (3) AC Evacuation; (4) 13X Evacuation; (5) AC Depressurising Pressure Equalisation; (6) 13X Depressurising Pressure Equalisation; (7) AC Blowdown; (8) 13X Blowdown; (9) 13X Purge; (10) AC Purge; (11) 13X Pressurising Pressure Equalisation; (12) AC Pressurising Pressure Equalisation; (13) AC Repressurisation; (14) 13X Repressurisation

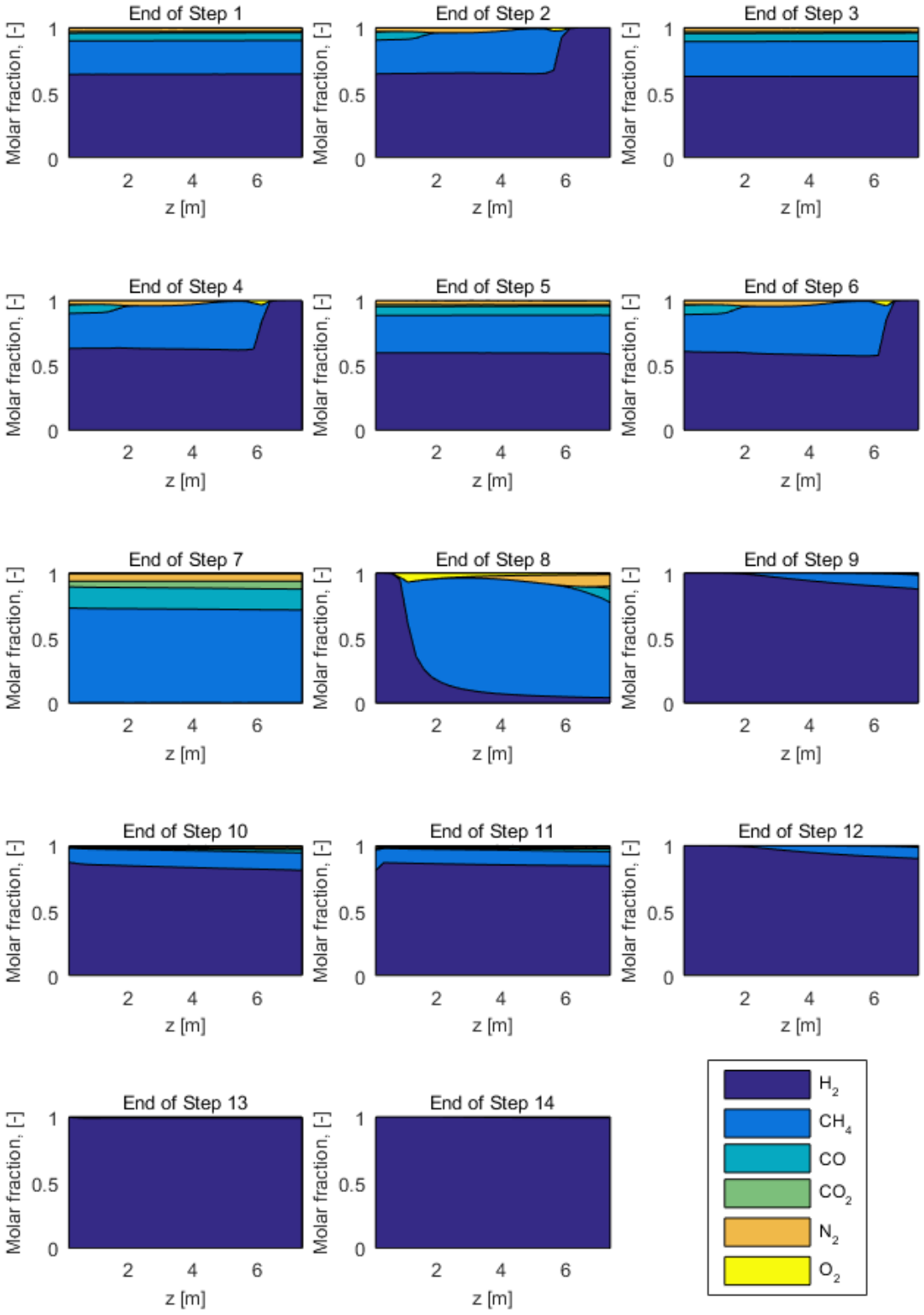

Figure 5.7 Gas phase concentrations in the bed at the end of each step during the PSA cycle. Steps: (1) AC Adsorption; (2) 13X Adsorption; (3) AC Evacuation; (4) 13X Evacuation; (5) AC Depressurising Pressure Equalisation; (6) 13X Depressurising Pressure Equalisation; (7) AC Blowdown; (8) 13X Blowdown; (9) 13X Purge; (10) AC Purge; (11) 13X Pressurising Pressure Equalisation; (12) AC Pressurising Pressure Equalisation; (13) AC Repressurisation; (14) 13X Repressurisation

Variation of gas concentration profile at the outlet of the column as a function of time for each step of the PSA cycle is shown in **Figure 5.8**. It can be seen from the gas concentration profile of **Figure 5.7** at the end of adsorption step of zeolite column that the adsorption step was just stopped before the H_2 wavefront reaches the end of the column. This ensures that the hydrogen product at the outlet end is still pure and free from impurities as shown in **Figure 5.8**. Further extension of adsorption step timing dilutes the hydrogen product with impurities which should be avoided.

Also, it can be seen from the outflow of step 4 of **Figure 5.8** that when the pressure is decreased during the evacuation step, hydrogen being the weakly bonded gas component is the first to get desorbed from the bed which could be collected thereby increasing product recovery. During depressurising pressure equalisation step, the remaining hydrogen present in the bed is transferred to the low pressure column.

Now, the column rich with CH_4 mixture is blown down as bottom product as shown in **Figure 5.8**. Variation of adsorbate loading at the end of each step of the PSA cycle is shown in **Figure 5.9**. It can be seen from the adsorbate loading at the end of step 7 and step 8 of **Figure 5.9** that some gas components remain adsorbed in the bed after blowdown step. A part of H_2 product is used to purge out the remaining gas components present in the bed.

After the purging step, the beds are better regenerated and are repressurised with H_2 product making them ready for next cycle of adsorption. It can be observed from step 13 and step 14 of **Figure 5.7** and **Figure 5.9** that after repressurisation step, both the bulk phase gas concentration in the bed and the adsorbate loading are free from impurities thereby ensuring effective adsorption of impurities during the next cycle of adsorption.

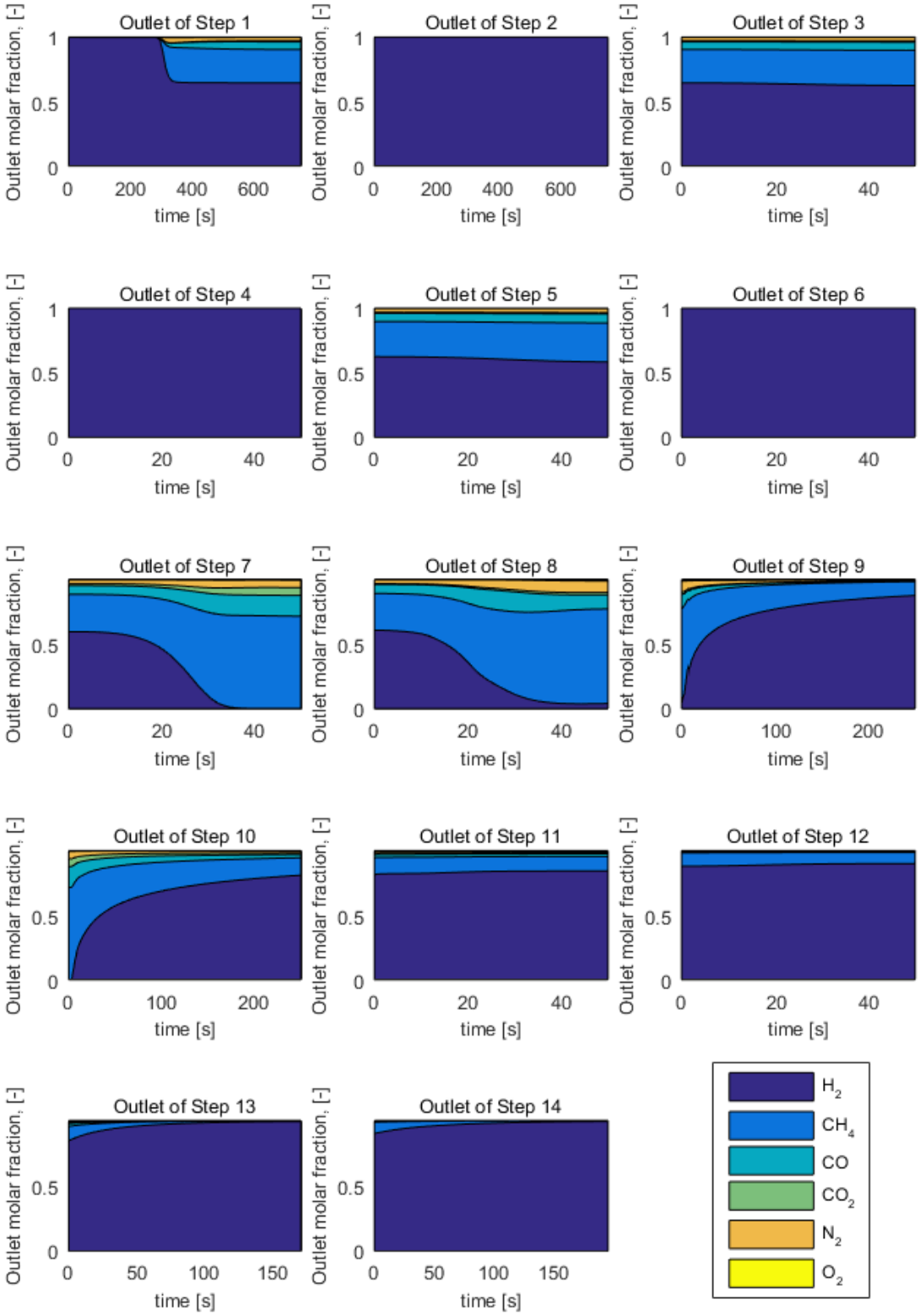

Figure 5.8 Outlet gas phase concentrations from the bed over the step time during the PSA cycle. Steps: (1) AC Adsorption; (2) 13X Adsorption; (3) AC Evacuation; (4) 13X Evacuation; (5) AC Depressurising Pressure Equalisation; (6) 13X Depressurising Pressure Equalisation; (7) AC Blowdown; (8) 13X Blowdown; (9) 13X Purge; (10) AC Purge; (11) 13X Pressurising Pressure Equalisation; (12) AC Pressurising Pressure Equalisation; (13) AC Repressurisation; (14) 13X Repressurisation

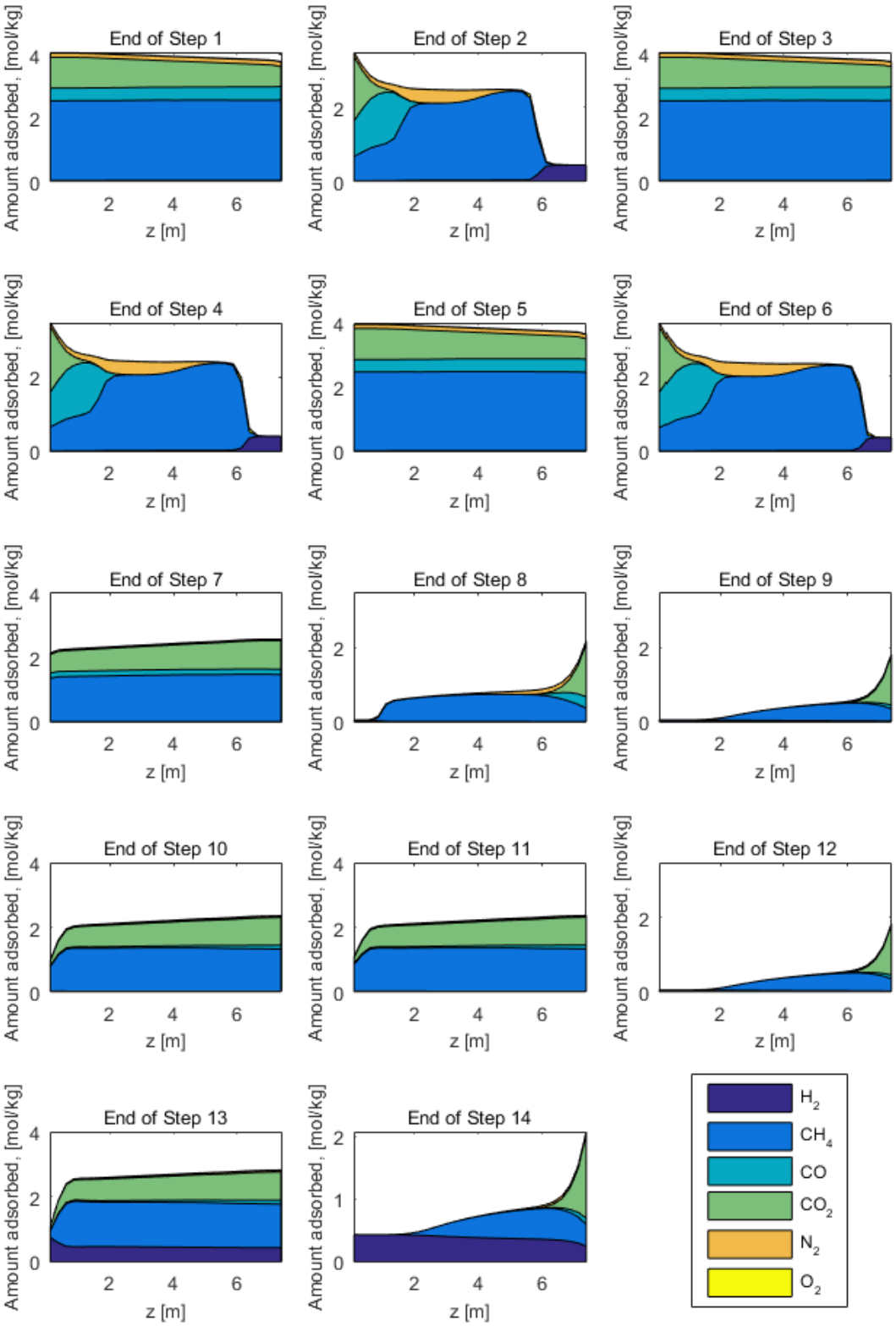

Figure 5.9 Adsorbate loading at the end of each step during the PSA cycle. Steps: (1) AC Adsorption; (2) 13X Adsorption; (3) AC Evacuation; (4) 13X Evacuation; (5) AC Depressurising Pressure Equalisation; (6) 13X Depressurising Pressure Equalisation; (7) AC Blowdown; (8) 13X Blowdown; (9) 13X Purge; (10) AC Purge; (11) 13X Pressurising Pressure Equalisation; (12) AC Pressurising Pressure Equalisation; (13) AC Repressurisation; (14) 13X Repressurisation

The concentration of impurities present in the hydrogen product are compared with the desired fuel cell vehicles (FCVs) concentration levels as described in section 1.2.3 and are found to be well within the allowable concentration levels as shown in **Table 5.2**.

Table 5.2 Comparison of concentration levels of impurities in hydrogen product with the allowable concentration levels

Impurity	Allowable Concentration (ppm)	Impurities concentration in H_2 product (ppm)
Methane	2	1
Carbon monoxide	0.2	3×10^{-10}
Carbon dioxide	2	4×10^{-6}
Nitrogen	100	0.002
Oxygen	5	0.007

Apart from the production of high purity hydrogen which is the desired product, the PSA process also produces two other valuable streams of methane rich product from the blowdown steps and an outlet purge stream whose composition is similar to that of the feed COG gas. The outlet purge stream can hence be mixed with the COG feed to be used as feed stream to the PSA cycle thereby improving the overall product recovery to 86%. The heating value of the blowdown streams are quite good on volume basis due to their rich methane content and hence could be used to partially displace natural gas usage in the internal operations of steel making process. The operating conditions of the different streams involved in the PSA process are summarised in **Table 5.3**.

Table 5.3 An overview of the different streams involved the H_2 PSA process (Rep –repress; Evac –evacuation; BD – blowdown)

Conditions	Feed stream	Purge in stream	Rep (2 streams)	Product stream	Evac stream	BD stream I	BD stream II	Purged out stream
Composition								
H_2	0.643	~1	~1	~1	~1	0.264	0.246	0.624
CH_4	0.257	-	-	-	-	0.528	0.546	0.269
CO	0.059	-	-	-	-	0.119	0.127	0.058
CO_2	0.013	-	-	-	-	0.035	0.014	0.024
N_2	0.026	-	-	-	-	0.047	0.063	0.022
O_2	0.002	-	-	-	-	0.004	0.004	0.003
Pressure (bar)	30	1	30	30	25	1	1	1
Temperature (K)	298	298	298	307	306	303	303	286
Flow rate (mol/s)	30	10	16	23	15	71	101	16
Average cycle flow rate (mol/s/cycle)	16.07	1.8	2.2	12.54	0.55	2.4	3.5	2.92

The developed PSA system operates with 8 columns in total, four each for carbon and zeolite beds. The specifications for each of the carbon and zeolite columns are in accordance with technical feasibility as summarised in **Table 5.4**. The cost of activated carbon and zeolite 13X adsorbents are 2.50 €/kg and 4.50 €/kg respectively according to Caldic B.V., an adsorbent distributor company [46].

Table 5.4 Specifications for activated carbon and zeolite columns

Column specifications	Carbon column	Zeolite column
Length (L)	7.5 m	7.5 m
Outer Radius (r_{out})	0.355 m	0.355 m
Inner Radius (r_{in})	0.350 m	0.350 m
Volume of adsorbent needed (V)	1.15 m^3	1.15 m^3
Amount of adsorbent needed (m)	981 kg	1616 kg

The resulting performance parameters for the optimised PSA cycle for producing high purity hydrogen product from coke oven gas are calculated as explained in section 3.6 and the results are summarised in **Table 5.5**.

Table 5.5 Performance parameters of the optimised PSA cycle

Performance Parameters	Value
Purity [-]	99.999+%
Recovery [-]	78%
Productivity, [moles of H_2 per m^3 of adsorbent bed per second]	9.26
Compressor Energy Consumption, [kWh/kg of H_2 produced]	3.37

Hence, from the multi-bed pressure swing adsorption model developed in the study, it is possible to produce high purity (>99.999 vol %) hydrogen product from coke oven gas at a recovery of over 75% with the quality requirements matching well with the desired hydrogen fuel source for fuel cell vehicles.

Economic Analysis

In this section, a simple economic analysis is performed to estimate the feasibility of the developed process. All the reference capacity based capital and operating cost details required for the economic analysis are obtained from the resources of Tata Steel [47]. The total investment cost includes the sum of capital costs of PSA unit, adsorbents used and the compressor required for pressurisation of coke oven gas. The variable cost includes the cost of coke oven gas fuel and the electricity cost required for compression of coke oven gas. Certain assumptions are made in the development of the economic model as follows: the fixed cost, the depreciation cost and the profit/loss are assumed to be 20%, 10% and 5% respectively of the total investment cost. For different capacities, the investment cost can be calculated from the reference investment using the power law described below:

$$\text{Investment (MUS\$)} = \text{Reference Investment} * \left(\frac{\text{Capacity}}{\text{Reference capacity}}\right)^{0.66}$$

It is found from the calculation results that for the production capacity of the designed PSA model (1675 tons/year), the production cost of gaseous hydrogen from coke oven gas at 30 bar is around 2300 €/ton which is slightly higher than the hydrogen production cost (2000 €/ton) from natural gas through the conventional steam methane reforming (SMR) process. But as the capacity increases to the reference capacity of 4000 ton/year, the production cost of hydrogen comes down and becomes equal that of the hydrogen produced from SMR process. The calculation results are summarised in **Table 5.6**.

Now, in order to valorise the produced hydrogen to be used as feed for fuel cell electric vehicles (FCEVs), the product should be compressed to 700 bar and stored under high pressure condition [48]. Hence in the economic model described above, the capital and operating cost required for the compression of hydrogen from 30 bar to 700 bar are included along with the investment cost for high pressure hydrogen storage container. The resulting production cost of the compressed hydrogen fuel comes to be around 3300 €/ton (for a profit ratio of 5% of the investment cost) which is much lower than the market price of compressed hydrogen fuel (6000 €/ton) showing a positive business scenario as detailed in **Table 5.7**.

Therefore by selling the produced compressed hydrogen fuel at the market price of 6000 €/ton, a profit of nearly 50% of the investment cost could be achieved as shown in **Table 5.8**. Hence, the return on investment for the developed business scenario comes down to less than a period of 3 years.

However, the discussed economic model is a simple case which did not include additional factors of consideration such as the transportation and logistics cost involved in the process, the lifetime of the adsorbents, the fluctuating price of electricity etc. which should properly be taken into account when considering a detailed economic model which is beyond the scope of this study.

Table 5.6 Economic Analysis for H_2 gas produced @ 30 bar from COG using PSA

	Reference capacity			Designed capacity	
Capacity (t/y)			4088		1675
1.PSA unit (M€)			7.59		4.21
2.Adsorbents (M€)			0.10		0.06
3.COG Compressor (M€)			1.97		1.09
Total Investment (M€)			**10**		**5**
Variable cost	**€/t**	**Yield %**	**€/t**		**€/t**
1.COG fuel (€/t)	121	12	1023		1023
2.COG compressor electricity (€/t)	169		169		169
Total operating cost (€/t)			**1192**		**1192**
Fixed cost					
% of Investment/capacity (€ /t)		20	473		641
Out of pocket price (€/t)			1665		1832
% Depr/Amort of I/C (€/t)		10	236		320
% Profit of I/C (€/t)		**5**	118	**5**	160
Integral cost price (€/t)			**2020**		**2313**
Hydrogen from natural gas (€/t)	**2060**				

Table 5.7 Economic Analysis for compressed H_2 gas production @ 700 bar

	Reference capacity			Designed capacity	
Capacity (t/y)			4088		1675
1.PSA unit (M€)			7.59		4.21
2.Adsorbents (M€)			0.10		0.06
3.COG Compressor (M€)			1.97		1.09
4. H2 Compressor (M€)			3.73		2.07
5.H2 storage (M€)			2.96		1.64
Total Investment (M€)			**16**		**9**
Variable cost	**€/t**	**Yield %**	**€/t**		**€/t**
1.COG fuel (€/t)	121	12	1023		1023
2.COG compressor electricity (€/t)	169		169		169
3.H2 compressor electricity (€/t)	241		241		241
Total operating cost (€/t)			**1433**		**1433**
Fixed cost					
% of Investment/capacity (€ /t)		20	800		1084
Out of pocket price (€/t)			2234		2517
% Depr/Amort of I/C (€/t)		10	400		542
% Profit of I/C (€/t)		**5**	200	**5**	271
Integral cost price (€/t)			**2834**		**3330**
Product					
Hydrogen Fuel (€/t) (@700 bar)	**6000**				

Table 5.8 Profitability analysis for selling compressed H_2 gas at market price

	Reference capacity			Designed capacity	
Capacity (t/y)			4088		1675
1.PSA unit (M€)			7.59		4.21
2.Adsorbents (M€)			0.10		0.06
3.COG Compressor (M€)			1.97		1.09
4. H2 Compressor (M€)			3.73		2.07
5.H2 storage (M€)			2.96		1.64
Total Investment (M€)			**16**		**9**
Variable cost	**€/t**	**Yield %**	**€/t**		**€/t**
1.COG fuel (€/t)	121	12	1023		1023
2.COG compressor electricity (€/t)	169		169		169
3.H2 compressor electricity (€/t)	241		241		241
Total operating cost (€/t)			**1433**		**1433**
Fixed cost					
% of Investment/capacity (€ /t)		20	800		1084
Out of pocket price (€/t)			2234		2517
% Depr/Amort of I/C (€/t)		10	400		542
% Profit of I/C (€/t)		**84**	3366	**54**	2941
Integral cost price (€/t)			**6000**		**6000**
Product					
Hydrogen Fuel (€/t)	**6000**				

Chapter 6

Conclusion

A flexible, fast and robust simulation tool for simulating a variety of pressure swing adsorption processes considering both equilibrium and kinetic effects using a detailed non-isothermal and non-isobaric model has been developed in the study. It has been successfully used for optimisation of a 14-step multi-bed PSA cycle for producing high purity (>99.999%) hydrogen from coke oven gas with a recovery of over 75%.

The adsorption equilibrium data required for the model were first calculated from experimental results using non-linear regression data fitting method. Then the carbon and zeolite adsorbents used in the adsorption process are modelled and simulated through molecular modeling MMFF method for estimating the adsorption equilibrium data i.e. isosteric heat of adsorption. The values estimated from molecular modeling matched well with the values calculated from experimental data. This gives a basic proof of concept that the adsorption equilibrium data could be calculated in a simple, fast and cost-effective way using molecular modeling methods without involving much experimentation, thereby saving a lot of time and energy involved in the process.

A series of rigorous parametric studies and breakthrough tests were performed using the developed mathematical model for better understanding of the effects of different factors on the performance of the PSA process. With the better understanding obtained from the above-mentioned studies, the model was optimized by performing several simulation tests to achieve the best possible process performance in terms of purity and recovery of the H_2 product, productivity of the adsorbents and energy consumption for compression of gases. Also, the bottom product which is a methane rich stream could be used for its heating value to partially displace natural gas consumption in the internal operations of the industry.

Thus, the concept developed in this study allows for an increased energy efficiency of coal usage by better utilisation of its by-product i.e. coke oven gas by converting it into valuable H_2 product, thereby increasing its chemical value to be used as a clean fuel for mobility applications as explained in the economic analysis section of previous chapter. An overview schematic of H_2 production from coke oven gas and its utilisation for fuel cell vehicles (FCVs) application is shown in **Figure 6.1**

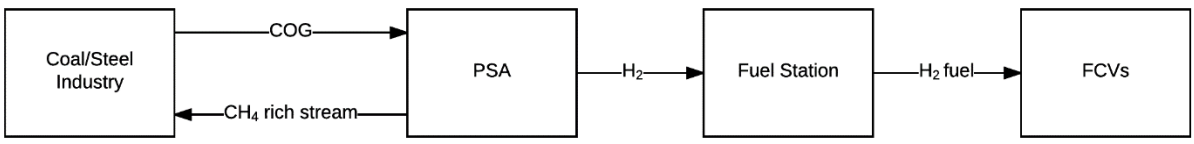

Figure 6.1 Overview schematic of H_2 production and utilisation for mobility applications

The scope of the developed concept can extend beyond the usage of hydrogen for mobility application. Currently, most of the electricity requirements for steel industries are provided by steam power plants with coal or its by-product coke oven gas produced from steel industries as energy input. Instead, the hydrogen produced from coke oven gas using the developed PSA concept could be fed to proton exchange membrane (PEM) fuel cells as shown in **Figure 6.2** for electricity generation in a cleaner way which is also energy-efficient as compared to that of conventional steam power plants.

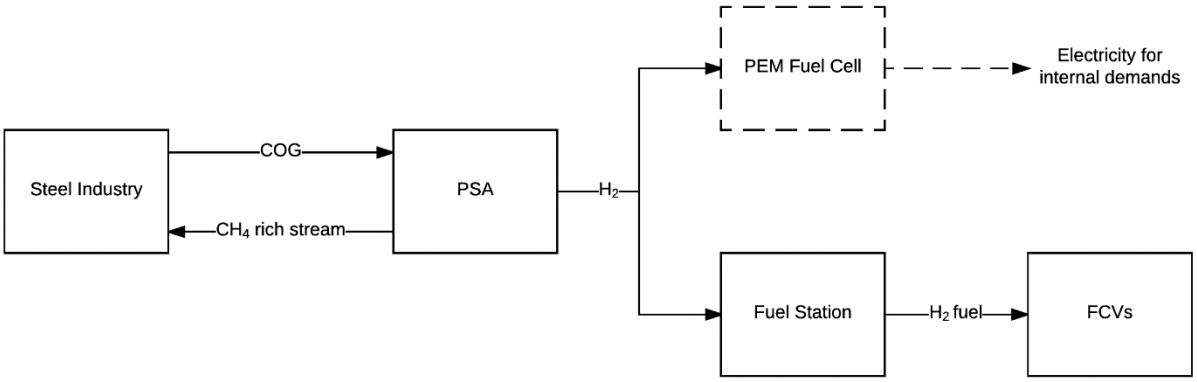

Figure 6.2 Electricity generation in Steel industry from H_2 produced through PSA process

In the future, when carbon capture technologies become an integral part of the industrial operation, the captured CO_2 should be used (CCU) instead of being stored (CCS) underground as it is not a permanent solution to the problem. The long term vision of the concept developed in this study is to effectively use the captured CO_2 along with the H_2 produced from PSA by producing liquid hydrocarbons/synthetic fuels as explained in **Figure 6.3**.

The storage of CO_2 in the form of liquid hydrocarbons is much effective as compared to that of gaseous CO_2 storage under high pressure conditions. This method of CO_2 conversion increase its commercial value as it is converted to a valuable chemical product. Thus, in addition to getting the carbon cycle closed, the CO_2 could be valorised to valuable chemical products by adapting to this method of CO_2 storage and utilisation.

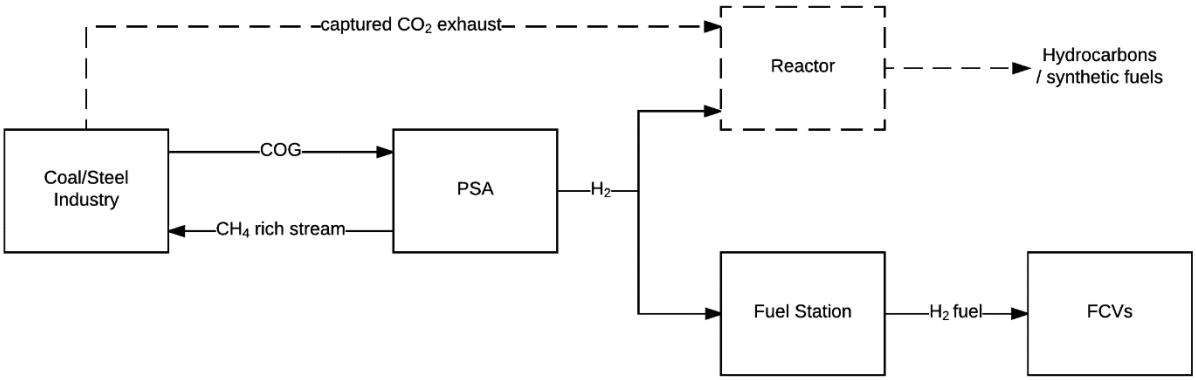

Figure 6.3 Captured CO_2 utilisation with H_2 produced through PSA process

The current techno-economic situation of renewable energy options, the large number of fossil fuel based power plants in operation and the availability of cheap and abundant coal make large scale deployment of renewable energy options prohibitively expensive in the near future.

As coal is certain to play a major role in the world's energy future due to its low cost and widespread distribution around the world, the study focused on developing a technology that will allow continued operation of coal, while improving its energy-efficiency by better utilization of its by-product i.e. coke oven gas by producing clean hydrogen fuel. Since, coal is the cheapest form of fossil fuel available, the large-scale hydrogen production from coke oven gas using the developed technology might possibly become the core competent to the current well-known method of hydrogen production from steam methane reforming (SMR) process in terms of production cost (as explained in the economic analysis section of previous chapter) as opposed to other energy intensive hydrogen production methods like electrolysis. The study concludes by proposing a long term vision of combining the developed hydrogen production concept with carbon capture technology for reducing the environmental impact of coal by CO_2 storage through an effective utilization in the form of hydrocarbon.

Appendices

Appendix A –Molecular mechanics Models

A.1. Strain Energy relation in Molecular modeling [49]

The molecular mechanics "energy" of a molecule is described in terms of a sum of contributions arising from distortions from "ideal" bond distances, bond angles and torsion angles together with contributions due to non-bonded interactions. It is commonly referred to as a "strain energy" meaning that it reflects the "strain" inherent to a "real" molecule relative to some ideal form.

$$E_A^{strain} = \sum_{A}^{bonds} E_A^{stretch} + \sum_{A}^{bond\ angles} E_A^{bend} + \sum_{A}^{torsion\ angles} E_A^{torsion} + \sum_{AB}^{non-bonded\ atoms} E_{AB}^{non-bonded}$$

The first three summations in the above equation are overall bond distances, bond angles and torsion angles respectively. The last summation is the overall pairs of atoms which are not bonded.

Stretch and bond terms are given in terms of quadratic Hooke's law form:

$$E^{stretch}(r) = \frac{1}{2} k^{stretch}(r - r^{eq})^2$$

$$E^{bend}(\alpha) = \frac{1}{2} k^{bend}(\alpha - \alpha^{eq})^2$$

where

r	-bond distance
α	-bond angle
r^{eq}	-ideal equilibrium bond distance
α^{eq}	-ideal equilibrium bond angle
$k^{stretch}$	-stretch force constant
k^{bend}	-bend force constant

Torsional term is described by a simple functional form,

$$E^{torsion}(\omega) = k^{torsion}[1 - \cos(\omega - \omega^{eq})]$$

where

ω -torsion angle

ω^{eq} -ideal torsion angle

$k^{torsion}$ -torsion parameter

Non-bonded interactions typically involve a sum of Van der Waals and Coulombic interactions.

$$E^{non-bonded}(r) = E^{VdW}(r) + E^{coulombic}(r)$$

Additional non-bonded terms may be included to account explicitly for such interactions as hydrogen bonding.

Van der Waals interactions are represented as a sum of repulsive and attractive terms.

$$E^{VdW}(r) = \varepsilon\left[\left(\frac{r^o}{r}\right)^{12} - 2\left(\frac{r^o}{r}\right)^{6}\right]$$

where

r -non-bonded distance

ε, r^o -Van der Waals parameters

The Coulombic term takes account of the interaction of charges.

$$E^{coulombic}(r) = \frac{qq'}{r}$$

where

r -non-bonded distance

q -atomic charges

A.2. Merck Molecular Force Field (MMFF)

The primary advantage of molecular mechanics models over quantum chemical models is their simplicity. Except for very small systems, computation cost is completely dominated by calculation of non-bonded van der Waals and Coulombic terms, the number of which is given by the square of the number of the atoms. However, the magnitude of these terms falls off rapidly with increasing interatomic distance and, in practice, computation cost scales linearly with molecular size for sufficiently large molecules. Molecular mechanics calculations may easily be performed on molecules comprising several thousand atoms. Additionally, molecular mechanics calculations are sufficiently rapid to permit extensive conformational searching on molecules containing upwards of 100-200 atoms. Conformational analysis is perhaps the single most important application of molecular mechanics. The fact that molecular mechanics models are parameterized may also be seen as providing an advantage over quantum chemical models. It is possible, at least in principle, to construct molecular mechanics models which will accurately reproduce known experimental data, and hopefully will anticipate (unknown) data on closely-related systems [49].

There are important limitations of molecular mechanics models. First, they are limited to the description of equilibrium geometries and equilibrium conformations. Because the mechanics "strain energy" is specific to a given molecule, strain energies cannot be generally used in thermochemical calculations. Second, molecular mechanics calculations reveal nothing about bonding or, more generally, about electron distributions in molecules. In many situations, information about electron distributions is key to modeling chemical reactivity and selectivity. There are, however, important situations where purely steric effects are responsible for trends in reactivity and selectivity, and here molecular mechanics would be expected to be of some value. Third, currently available force fields have not been parameterized to handle non-equilibrium forms, in particular, reaction transition states. Finally, it needs to be noted that molecular mechanics is essentially an interpolation scheme, the success of which depends not only on good parameters, but also on systematics among related molecules [49].

A.3. Building and optimisation procedures followed for modeling of adsorbent molecules needed for research using Spartan Molecular Mechanics model

A.3.1. Activated carbon

A basic benzene ring is used to build a hexagonal layer of carbon atoms. Hydrogen atoms at the periphery of the plane are removed/replaced with functional groups shown in **Figure 2.5**. Micropores are made in the carbon layer by removal of few carbon atoms. The usefulness of activated carbon as an adsorbent is mainly derived from its micropore and mesopore volumes. After the activated carbon layer is modelled, molecular mechanics (MMFF) method is used to calculate the equilibrium geometry. The resulting twisted chain of defective carbon layer with functional groups bound to the periphery of the plane are shown in **Figure 2.7**.

Now, each of the gas components (H_2, CH_4, CO, CO_2, N_2 and O_2) present in coke oven gas are placed in contact with different number of activated carbon layers at different possible positions such as on the carbon surface, near the functional group, in the gap between two/three activated carbon layers and in the pores.

The models are simulated with molecular mechanics to find the resulting equilibrium geometries for each of the gas molecule's interaction with activated carbon. Energy profiles are calculated by setting distance constraints to identify the lowest energy position for each of the gas molecules on the adsorbent surface. The resulting binding sites of different gas components on the activated carbon adsorbent surface are shown in **Figure 2.8**. The change in strain energy (E) due to the physisorption of gas molecules on carbon surface are calculated using equation (2.7) which gives the isosteric heat of adsorption values.

A.3.2. Zeolite 13X (LiX)

A basic faujasite (FAU) structure made of silicon and oxygen atoms is taken from the International Zeolite Association (IZA) database. Using Mercury (CSD product) [50] which is a program for visualising crystal structures in three dimensions, the FAU structure is packed to form a 1x1x1 unit cell and converted to a file type that is accessible by Spartan. Now, using Spartan software aluminium atoms are added in place of silicon atoms in order to bring the ratio of Si:Al to 1:1 required for LiX zeolite type. Bronsted acidic sites are generated due to the replacement of Si which has a formal valence of four with Al which has a formal valence of three. This is compensated by the attachment of lithium cations to the oxygen atom connecting the Si and Al atom thereby resulting in a chemically stable structure.

Since a unit cell of faujasite has too many atoms (>2000 atoms), the computational time involved in the simulation of the whole unit cell is very high. Therefore, in order to improve the speed of computation the FAU unit cell is broken down to its three basic building units i.e. sodalite, hexagonal prism and super-cage structures as shown in **Figure 2.9**. Molecular mechanics (MMFF) is used to calculate the equilibrium geometries of each of the basic structure and the resulting geometries are shown as tube models in **Figure 2.11**.

Now, each of the gas components (H_2, CH_4, CO, CO_2, N_2, and O_2) present in coke oven gas are placed in contact with the three different basic building units of faujasite. The models are simulated with molecular mechanics to find the resulting equilibrium geometries for each of the gas molecule's interaction with the different building units of faujasite.

Energy profiles are calculated by setting distance constraints to identify the lowest energy position for each of the gas molecules on the three different adsorbent surfaces. The resulting preferred binding sites of different gas components on zeolite adsorbent surface (super-cage structure) are shown in **Figure 2.12**. The change in strain energy (E) due to the physisorption of gas molecules on zeolite surface are calculated using equation (2.7) which gives the isosteric heat of adsorption values.

Appendix B –Experimental Adsorption Isotherm data

The experimental adsorption isotherm data required for the calculation of adsorption equilibrium parameters are taken from literature [15] and are summarised in **Table B.0.1** - **Table B.0.12**

Table B.0.1 Experimental Adsorption Isotherm for H_2 on activated carbon

T=293K		T=308K		T=323K	
P (bar)	**q_{exp} (mol.kg^{-1})**	**P (bar)**	**q_{exp} (mol.kg^{-1})**	**P (bar)**	**q_{exp} (mol.kg^{-1})**
0.000	0.000	0.000	0.000	0.000	0.000
0.993	0.062	0.969	0.051	0.978	0.044
1.020	0.063	1.000	0.051	1.010	0.045
1.350	0.079	1.340	0.065	1.350	0.055
1.690	0.095	1.690	0.077	1.690	0.064
2.020	0.111	2.030	0.090	2.040	0.073
2.350	0.126	2.370	0.102	2.380	0.082
2.690	0.142	2.710	0.115	2.730	0.092
3.020	0.157	3.050	0.127	3.070	0.100
3.360	0.171	3.400	0.139	3.420	0.109
3.700	0.186	3.740	0.150	3.770	0.118
4.030	0.202	4.080	0.162	4.110	0.128
4.370	0.217	4.420	0.174	4.460	0.136
4.710	0.231	4.770	0.186	4.800	0.145
5.050	0.247	5.110	0.199	5.150	0.155
5.380	0.261	5.450	0.210	5.490	0.163
5.720	0.276	5.790	0.222	5.840	0.172
6.060	0.290	6.130	0.234	6.190	0.182
6.400	0.304	6.480	0.246	6.530	0.189
6.730	0.319	6.820	0.257	6.870	0.199
7.070	0.332	7.160	0.269	7.220	0.207
7.410	0.347	7.500	0.280	7.560	0.215
7.740	0.360	7.850	0.291	7.910	0.223
8.080	0.374	8.190	0.303	8.250	0.232
8.420	0.387	8.530	0.315	8.600	0.241
8.760	0.401	8.870	0.326	8.940	0.248
9.090	0.415	9.210	0.338	9.290	0.257

Table B.0.2 Experimental Adsorption Isotherm for CH_4 on activated carbon

T=293K		T=308K		T=323K	
P (bar)	**q_{exp} ($mol.kg^{-1}$)**	**P (bar)**	**q_{exp} ($mol.kg^{-1}$)**	**P (bar)**	**q_{exp} ($mol.kg^{-1}$)**
0.000	0.000	0.000	0.000	0.000	0.000
0.083	0.189	0.081	0.095	0.079	0.060
0.150	0.311	0.172	0.193	0.156	0.116
0.224	0.433	0.258	0.278	0.242	0.177
0.344	0.600	0.347	0.361	0.332	0.240
0.468	0.749	0.431	0.436	0.421	0.300
0.593	0.883	0.530	0.519	0.505	0.354
0.719	1.004	0.615	0.589	0.596	0.411
0.847	1.116	0.745	0.699	0.688	0.468
0.957	1.211	0.873	0.799	0.742	0.499
1.060	1.291	0.996	0.885	0.830	0.592
1.340	1.476	1.100	0.956	0.950	0.658
1.620	1.647	1.240	1.019	1.070	0.721
1.910	1.798	1.520	1.156	1.370	0.864
2.200	1.940	1.800	1.279	1.670	0.993
2.500	2.067	2.090	1.421	1.970	1.115
2.800	2.187	2.380	1.546	2.280	1.224
3.110	2.298	2.690	1.664	2.590	1.328
3.410	2.398	2.990	1.773	2.910	1.425
3.720	2.497	3.300	1.876	3.220	1.520
4.350	2.673	3.920	2.063	3.860	1.691
4.670	2.753	4.230	2.148	4.180	1.771
4.990	2.827	4.540	2.224	4.500	1.844
5.310	2.901	4.860	2.301	4.820	1.920
5.620	2.971	5.180	2.370	5.150	1.989
5.950	3.032	5.500	2.435	5.470	2.056
6.270	3.097	5.830	2.497	5.800	2.118
6.590	3.156	6.150	2.550	6.130	2.183
6.920	3.217	6.480	2.605	6.460	2.240
7.240	3.272	6.800	2.658	6.790	2.297
7.570	3.324	7.130	2.709	7.120	2.351
7.900	3.374	7.460	2.754	7.450	2.405
8.220	3.427	7.790	2.801	7.780	2.458
8.550	3.468	8.120	2.844	8.110	2.507
8.880	3.513	8.450	2.885	8.440	2.554
9.210	3.558	8.780	2.924	8.770	2.601
		9.110	2.961	9.110	2.646
		9.440	2.999		

Table B.0.3 Experimental Adsorption Isotherm for CO on activated carbon

T=293K		T=308K		T=323K	
P (bar)	**q_{exp} (mol.kg^{-1})**	**P (bar)**	**q_{exp} (mol.kg^{-1})**	**P (bar)**	**q_{exp} (mol.kg^{-1})**
0.000	0.000	0.000	0.000	0.000	0.000
0.098	0.069	0.101	0.051	0.080	0.031
0.190	0.129	0.182	0.091	0.154	0.058
0.301	0.198	0.315	0.151	0.241	0.089
0.372	0.240	0.375	0.177	0.407	0.143
0.478	0.298	0.468	0.217	0.555	0.189
0.594	0.359	0.522	0.239	0.721	0.238
0.657	0.390	0.620	0.279	0.791	0.259
0.740	0.431	0.691	0.306	0.880	0.282
0.839	0.476	0.772	0.337	0.934	0.295
0.975	0.535	0.848	0.365	1.070	0.335
1.100	0.593	0.910	0.387	1.390	0.422
1.410	0.710	1.040	0.434	1.710	0.497
1.710	0.818	1.350	0.535	2.030	0.572
2.020	0.922	1.660	0.627	2.360	0.641
2.330	1.019	1.980	0.717	2.680	0.708
2.650	1.108	2.290	0.802	3.010	0.775
2.960	1.192	2.620	0.880	3.340	0.832
3.280	1.270	2.940	0.953	3.660	0.891
3.910	1.414	3.580	1.094	4.320	1.000
4.240	1.480	3.910	1.155	4.650	1.052
4.560	1.543	4.230	1.217	4.980	1.101
4.880	1.601	4.560	1.277	5.320	1.149
5.200	1.662	4.890	1.334	5.650	1.197
5.530	1.714	5.220	1.388	5.990	1.241
5.850	1.768	5.550	1.440	6.320	1.281
6.180	1.819	5.880	1.492	6.660	1.323
6.510	1.863	6.210	1.539	7.000	1.361
6.830	1.912	6.540	1.586	7.340	1.402
7.160	1.958	6.880	1.629	7.670	1.438
7.490	2.001	7.210	1.674	8.010	1.475
7.820	2.042	7.540	1.714	8.350	1.511
8.150	2.079	7.870	1.750	8.680	1.545
8.480	2.120	8.210	1.790	9.020	1.578
8.810	2.157	8.540	1.827		
9.140	2.193	8.880	1.859		
		9.210	1.895		

Table B.0.4 Experimental Adsorption Isotherm for CO_2 on activated carbon

T=293K		T=308K		T=323K	
P (bar)	**q_{exp} (mol.kg^{-1})**	**P (bar)**	**q_{exp} (mol.kg^{-1})**	**P (bar)**	**q_{exp} (mol.kg^{-1})**
0.000	0.000	0.000	0.000	0.000	0.000
0.098	0.657	0.088	0.389	0.067	0.208
0.190	1.040	0.183	0.686	0.145	0.398
0.284	1.347	0.295	0.966	0.233	0.577
0.372	1.590	0.379	1.144	0.327	0.747
0.468	1.820	0.467	1.311	0.429	0.907
0.549	1.994	0.559	1.470	0.533	1.058
0.657	2.203	0.654	1.619	0.643	1.200
0.747	2.362	0.753	1.762	0.756	1.337
0.839	2.511	0.829	1.865	0.870	1.463
0.927	2.650	0.930	1.993	0.975	1.573
1.010	2.762	1.020	2.102	1.020	1.621
1.140	2.934	1.170	2.265	1.190	1.772
1.280	3.100	1.320	2.422	1.350	1.917
1.420	3.262	1.480	2.573	1.530	2.060
1.570	3.418	1.640	2.719	1.710	2.194
1.730	3.567	1.820	2.860	1.890	2.325
1.900	3.714	2.000	2.998	2.090	2.451
2.070	3.853	2.180	3.129	2.290	2.573
2.250	3.988	2.370	3.256	2.490	2.691
2.440	4.118	2.570	3.380	2.700	2.805
2.630	4.241	2.770	3.497	2.910	2.914
2.830	4.361	2.980	3.612	3.130	3.020
3.040	4.476	3.190	3.722	3.360	3.122
3.250	4.585	3.410	3.828	3.580	3.221
3.700	4.790	3.870	4.029	4.060	3.410
3.930	4.886	4.100	4.125	4.300	3.499
4.160	4.978	4.340	4.215	4.550	3.586
4.400	5.066	4.580	4.303	4.800	3.669
4.650	5.149	4.830	4.387	5.050	3.749
4.900	5.229	5.080	4.470	5.310	3.827
5.150	5.306	5.340	4.547	5.570	3.901
5.410	5.378	5.600	4.623	5.830	3.973
5.680	5.447	5.860	4.695	6.100	4.042
5.950	5.514	6.130	4.765	6.370	4.109
6.220	5.576	6.400	4.830	6.640	4.175
6.490	5.636	6.670	4.895	6.920	4.237
6.770	5.694	6.950	4.956	7.200	4.297
7.050	5.748	7.230	5.016	7.480	4.355
7.330	5.800	7.510	5.074	7.760	4.412
7.620	5.850	7.790	5.129	8.050	4.465
7.910	5.897	8.080	5.182	8.340	4.518

8.200	5.943	8.370	5.233	8.630	4.568
8.500	5.986	8.660	5.282	8.930	4.616
8.790	6.026	8.960	5.330	9.220	4.664
9.090	6.065	9.250	5.375	9.520	4.709
9.390	6.103	9.550	5.419	9.810	4.753
9.690	6.137	9.850	5.461	10.110	4.795
9.990	6.171	10.150	5.502		

Table B.0.5 Experimental Adsorption Isotherm for N_2 on activated carbon

T=293K		**T=308K**		**T=323K**	
P (bar)	**q_{exp} ($mol.kg^{-1}$)**	**P (bar)**	**q_{exp} ($mol.kg^{-1}$)**	**P (bar)**	**q_{exp} ($mol.kg^{-1}$)**
0.000	0.000	0.000	0.000	0.000	0.000
0.098	0.050	0.109	0.040	0.114	0.031
0.188	0.095	0.208	0.076	0.224	0.061
0.280	0.139	0.311	0.112	0.330	0.089
0.371	0.180	0.412	0.146	0.437	0.116
0.462	0.220	0.512	0.178	0.542	0.142
0.554	0.259	0.610	0.209	0.644	0.166
0.646	0.296	0.707	0.239	0.746	0.191
0.736	0.332	0.802	0.267	0.849	0.214
0.827	0.366	0.896	0.294	0.945	0.236
0.915	0.399	0.981	0.319	1.040	0.256
0.992	0.425	1.020	0.329	1.320	0.316
1.030	0.439	1.280	0.399	1.590	0.374
1.280	0.520	1.550	0.467	1.880	0.430
1.530	0.599	1.820	0.532	2.160	0.484
1.780	0.674	2.090	0.595	2.450	0.535
2.040	0.745	2.370	0.655	2.740	0.585
2.300	0.815	2.650	0.713	3.030	0.634
2.560	0.881	2.930	0.768	3.330	0.681
2.830	0.945	3.210	0.823	3.620	0.727
3.100	1.007	3.490	0.876	3.920	0.771
3.370	1.066	3.780	0.927	4.220	0.813
3.650	1.123	4.070	0.976	4.520	0.856
4.210	1.231	4.660	1.069	5.130	0.938
4.500	1.282	4.950	1.114	5.430	0.976
4.780	1.332	5.250	1.158	5.740	1.014
5.070	1.381	5.550	1.200	6.050	1.051
5.360	1.428	5.840	1.242	6.350	1.086
5.650	1.474	6.140	1.282	6.660	1.121
5.950	1.518	6.450	1.321	6.970	1.155
6.240	1.561	6.750	1.359	7.290	1.188
6.540	1.602	7.050	1.396	7.600	1.220
6.840	1.644	7.360	1.432	7.910	1.252

7.130	1.682	7.670	1.467	8.220	1.284
7.440	1.721	7.970	1.503	8.540	1.313
7.740	1.758	8.280	1.536	8.850	1.343
8.040	1.794	8.600	1.569	9.170	1.372
8.340	1.831	8.900	1.600	9.480	1.401
8.650	1.865	9.220	1.631	9.800	1.429
8.950	1.899	9.530	1.663	10.120	1.457
9.260	1.932	9.840	1.693		
9.560	1.964	10.160	1.723		
9.870	1.996				
10.180	2.026				

Table B.0.6 Experimental Adsorption Isotherm for O_2 on activated carbon

T=293K		**T=308K**		**T=323K**	
P (bar)	**q_{exp} (mol.kg^{-1})**	**P (bar)**	**q_{exp} (mol.kg^{-1})**	**P (bar)**	**q_{exp} (mol.kg^{-1})**
0.000	0.000	0.000	0.000	0.000	0.000
0.119	0.056	0.120	0.042	0.124	0.032
0.228	0.106	0.235	0.080	0.243	0.062
0.337	0.154	0.349	0.117	0.358	0.091
0.443	0.199	0.461	0.153	0.470	0.119
0.551	0.244	0.570	0.187	0.582	0.145
0.654	0.285	0.677	0.220	0.690	0.171
0.757	0.325	0.783	0.252	0.794	0.195
0.856	0.362	0.887	0.282	0.899	0.219
0.947	0.399	0.982	0.311	0.997	0.239
1.030	0.430	1.030	0.323	1.050	0.250
1.290	0.520	1.310	0.401	1.340	0.314
1.560	0.611	1.590	0.475	1.640	0.377
1.830	0.696	1.880	0.550	1.940	0.439
2.110	0.777	2.160	0.619	2.240	0.497
2.390	0.858	2.450	0.688	2.540	0.555
2.670	0.935	2.740	0.754	2.840	0.610
2.950	1.011	3.040	0.818	3.140	0.666
3.230	1.084	3.330	0.879	3.450	0.719
3.520	1.154	3.630	0.940	3.760	0.771
3.800	1.222	3.930	0.999	4.060	0.821
4.390	1.352	4.530	1.112	4.680	0.917
4.680	1.415	4.830	1.168	4.990	0.965
4.970	1.476	5.130	1.223	5.300	1.010
5.270	1.534	5.440	1.273	5.400	1.060
5.560	1.593	5.740	1.325	5.610	1.100
5.860	1.650	6.050	1.374	6.240	1.150
6.160	1.704	6.350	1.421	6.550	1.190
6.460	1.758	6.660	1.470	6.870	1.230

6.760	1.810	6.970	1.516	7.190	1.270
7.070	1.860	7.280	1.561	7.500	1.310
7.370	1.912	7.590	1.605	7.820	1.350
7.670	1.958	7.900	1.649	8.140	1.380
7.980	2.006	8.210	1.690	8.460	1.420
8.280	2.052	8.520	1.731	8.770	1.460
8.590	2.095	8.830	1.773	9.090	1.500
8.900	2.141	9.150	1.814	9.410	1.530
9.210	2.184	9.460	1.854	9.730	1.570
9.510	2.226	9.780	1.892		
9.820	2.269	10.090	1.931		
10.130	2.308				

Table B.0.7 Experimental Adsorption Isotherm for H_2 on zeolite 13X

T=293K		T=308K		T=323K	
P (bar)	**q_{exp} (mol.kg^{-1})**	**P (bar)**	**q_{exp} (mol.kg^{-1})**	**P (bar)**	**q_{exp} (mol.kg^{-1})**
0.000	0.000	0.000	0.000	0.000	0.000
1.070	0.060	1.090	0.056	1.090	0.055
1.410	0.070	1.430	0.064	1.430	0.061
1.750	0.079	1.770	0.070	1.780	0.067
2.090	0.086	2.120	0.079	2.130	0.075
2.420	0.097	2.460	0.087	2.470	0.082
2.760	0.104	2.800	0.094	2.820	0.088
3.100	0.111	3.140	0.102	3.160	0.094
3.440	0.119	3.480	0.110	3.510	0.102
3.780	0.129	3.830	0.116	3.860	0.108
4.120	0.138	4.170	0.125	4.200	0.113
4.460	0.144	4.510	0.133	4.550	0.122
4.800	0.153	4.850	0.142	4.900	0.130
5.140	0.162	5.200	0.148	5.240	0.137
5.480	0.167	5.540	0.155	5.590	0.145
5.820	0.176	5.890	0.162	5.940	0.150
6.160	0.185	6.230	0.171	6.280	0.158
6.500	0.193	6.570	0.177	6.630	0.165
6.840	0.201	6.910	0.185	6.980	0.171
7.180	0.209	7.250	0.193	7.320	0.177
7.520	0.219	7.590	0.202	7.670	0.185
7.860	0.227	7.940	0.209	8.010	0.193
8.200	0.236	8.280	0.216	8.360	0.200
8.540	0.244	8.620	0.223	8.700	0.207
8.880	0.250	8.960	0.228	9.050	0.215
9.220	0.259	9.310	0.238		

Table B.0.8 Experimental Adsorption Isotherm for CH_4 on zeolite 13X

T=293K		T=308K		T=323K	
P (bar)	**q_{exp} (mol.kg^{-1})**	**P (bar)**	**q_{exp} (mol.kg^{-1})**	**P (bar)**	**q_{exp} (mol.kg^{-1})**
0.000	0.000	0.000	0.000	0.000	0.000
0.096	0.130	0.131	0.126	0.132	0.086
0.190	0.259	0.226	0.206	0.258	0.162
0.290	0.367	0.339	0.293	0.386	0.233
0.395	0.466	0.456	0.374	0.513	0.298
0.502	0.556	0.572	0.448	0.639	0.358
0.613	0.641	0.690	0.517	0.766	0.416
0.725	0.719	0.804	0.581	0.875	0.466
0.836	0.790	0.908	0.634	0.985	0.511
0.937	0.850	1.010	0.686	1.090	0.552
1.040	0.906	1.270	0.802	1.360	0.653
1.290	1.033	1.530	0.909	1.640	0.744
1.540	1.151	1.800	1.007	1.920	0.831
1.800	1.257	2.080	1.098	2.210	0.912
2.080	1.356	2.360	1.185	2.500	0.987
2.350	1.447	2.640	1.266	2.790	1.058
2.630	1.534	2.930	1.341	3.090	1.126
2.920	1.614	3.220	1.412	3.390	1.191
3.200	1.689	3.520	1.480	3.700	1.252
3.790	1.825	4.120	1.603	4.310	1.363
4.090	1.887	4.430	1.658	4.620	1.415
4.390	1.946	4.730	1.712	4.940	1.465
4.690	2.001	5.040	1.763	5.250	1.513
5.000	2.053	5.360	1.812	5.570	1.559
5.310	2.102	5.670	1.858	5.890	1.601
5.620	2.150	5.980	1.903	6.200	1.642
5.930	2.195	6.300	1.943	6.520	1.681
6.240	2.237	6.620	1.982	6.840	1.718
6.560	2.277	6.940	2.020	7.170	1.756
6.870	2.315	7.260	2.055	7.500	1.790
7.190	2.352	7.580	2.091	7.820	1.822
7.510	2.387	7.900	2.124	8.150	1.855
7.830	2.420	8.230	2.156	8.470	1.885
8.150	2.451	8.550	2.185	8.800	1.914
8.480	2.482	8.880	2.213	9.130	1.941
8.800	2.510	9.200	2.241		
9.130	2.537				

Table B.0.9 Experimental Adsorption Isotherm for CO on zeolite 13X

T=293K		T=308K		T=323K	
P (bar)	**q_{exp} (mol.kg^{-1})**	**P (bar)**	**q_{exp} (mol.kg^{-1})**	**P (bar)**	**q_{exp} (mol.kg^{-1})**
0.000	0.000	0.000	0.000	0.000	0.000
0.045	0.474	0.035	0.201	0.073	0.250
0.089	0.672	0.075	0.429	0.111	0.382
0.153	0.838	0.135	0.602	0.190	0.532
0.233	0.977	0.212	0.750	0.283	0.660
0.328	1.097	0.303	0.875	0.387	0.768
0.432	1.201	0.404	0.981	0.500	0.861
0.542	1.293	0.515	1.073	0.621	0.943
0.657	1.374	0.631	1.154	0.741	1.012
0.777	1.447	0.751	1.225	0.867	1.075
0.885	1.507	0.859	1.282	0.979	1.127
0.996	1.562	0.968	1.333	1.090	1.175
1.100	1.613	1.080	1.382	1.370	1.273
1.370	1.719	1.350	1.483	1.650	1.357
1.640	1.814	1.630	1.572	1.940	1.434
1.920	1.898	1.910	1.654	2.240	1.503
2.210	1.974	2.210	1.727	2.540	1.567
2.500	2.044	2.500	1.793	2.840	1.626
2.790	2.110	2.800	1.854	3.150	1.680
3.090	2.168	3.110	1.912	3.460	1.732
3.700	2.278	3.730	2.016	4.090	1.825
4.010	2.328	4.040	2.065	4.410	1.867
4.320	2.373	4.360	2.108	4.730	1.908
4.640	2.418	4.670	2.151	5.040	1.947
4.950	2.460	4.990	2.191	5.370	1.983
5.270	2.499	5.310	2.229	5.690	2.020
5.590	2.537	5.630	2.267	6.010	2.053
5.910	2.574	5.960	2.302	6.330	2.086
6.220	2.607	6.280	2.335	6.660	2.118
6.550	2.640	6.610	2.367	6.990	2.148
6.870	2.671	6.930	2.400	7.320	2.178
7.190	2.700	7.260	2.429	7.650	2.205
7.520	2.729	7.580	2.458	7.980	2.231
7.840	2.758	7.910	2.485	8.310	2.258
8.170	2.785	8.240	2.513	8.640	2.282
8.500	2.811	8.570	2.537	8.970	2.306
8.830	2.834	8.900	2.563	9.300	2.332
9.160	2.859	9.230	2.588		

Table B.0.10 Experimental Adsorption Isotherm for CO_2 on zeolite 13X

T=293K		T=308K		T=323K	
P (bar)	**q_{exp} (mol.kg^{-1})**	**P (bar)**	**q_{exp} (mol.kg^{-1})**	**P (bar)**	**q_{exp} (mol.kg^{-1})**
0.000	0.000	0.000	0.000	0.000	0.000
0.005	1.058	0.010	1.745	0.021	1.269
0.007	1.317	0.020	1.949	0.037	1.462
0.010	1.574	0.036	2.145	0.061	1.642
0.015	1.827	0.059	2.330	0.096	1.810
0.025	2.077	0.090	2.504	0.139	1.965
0.041	2.317	0.128	2.669	0.191	2.110
0.061	2.550	0.174	2.824	0.252	2.244
0.087	2.775	0.227	2.967	0.319	2.367
0.119	2.990	0.287	3.103	0.394	2.482
0.156	3.196	0.354	3.229	0.474	2.587
0.199	3.390	0.427	3.344	0.560	2.683
0.249	3.573	0.507	3.449	0.651	2.772
0.306	3.746	0.592	3.544	0.745	2.852
0.371	3.905	0.684	3.630	0.843	2.925
0.444	4.050	0.779	3.707	0.937	3.004
0.524	4.180	0.870	3.790	1.030	3.078
0.613	4.299	0.963	3.867	1.260	3.232
0.707	4.404	1.060	3.935	1.510	3.367
0.807	4.496	1.300	4.077	1.770	3.482
0.900	4.568	1.550	4.197	2.040	3.584
0.995	4.635	1.820	4.300	2.320	3.674
1.100	4.695	2.100	4.386	2.610	3.753
1.350	4.815	2.390	4.463	2.910	3.823
1.610	4.915	2.680	4.529	3.210	3.884
2.180	5.068	3.300	4.639	3.840	3.990
2.480	5.130	3.610	4.686	4.150	4.035
2.780	5.180	3.930	4.728	4.470	4.076
3.090	5.226	4.250	4.765	4.790	4.115
3.400	5.264	4.570	4.802	5.120	4.151
3.720	5.296	4.900	4.834	5.440	4.183
4.040	5.327	5.220	4.863	5.770	4.213
4.360	5.354	5.550	4.891	6.100	4.240
4.680	5.376	5.880	4.915	6.430	4.266
5.010	5.397	6.210	4.939	6.770	4.290
5.330	5.416	6.540	4.961	7.100	4.312
5.660	5.432	6.880	4.981	7.440	4.334
5.990	5.445	7.210	5.002	7.770	4.353
6.320	5.456	7.540	5.018	8.110	4.372
6.650	5.466	7.880	5.036	8.450	4.391
6.980	5.473	8.210	5.053	8.790	4.409
7.310	5.481	8.550	5.066	9.120	4.424

7.640	5.485	8.890	5.079	
7.980	5.488	9.220	5.096	
8.310	5.492			
8.650	5.493			
8.980	5.494			
9.310	5.493			

Table B.0.11 Experimental Adsorption Isotherm for N_2 on zeolite 13X

T=293K		**T=308K**		**T=323K**	
P (bar)	**q_{exp} (mol.kg^{-1})**	**P (bar)**	**q_{exp} (mol.kg^{-1})**	**P (bar)**	**q_{exp} (mol.kg^{-1})**
0.000	0.000	0.000	0.000	0.000	0.000
0.083	0.129	0.129	0.119	0.137	0.078
0.189	0.256	0.232	0.199	0.267	0.148
0.294	0.358	0.351	0.279	0.400	0.210
0.407	0.450	0.474	0.352	0.533	0.267
0.522	0.531	0.599	0.417	0.668	0.320
0.639	0.604	0.725	0.477	0.804	0.369
0.761	0.670	0.852	0.532	0.928	0.410
0.875	0.723	0.970	0.579	1.050	0.446
0.990	0.775	1.090	0.622	1.340	0.528
1.100	0.822	1.370	0.716	1.630	0.603
1.370	0.923	1.650	0.797	1.930	0.672
1.650	1.010	1.940	0.874	2.230	0.734
1.940	1.092	2.240	0.940	2.540	0.795
2.230	1.163	2.540	1.005	2.850	0.849
2.530	1.231	2.840	1.063	3.160	0.899
2.830	1.291	3.150	1.119	3.480	0.948
3.130	1.351	3.460	1.169	3.790	0.993
3.440	1.403	3.780	1.218	4.110	1.037
4.060	1.502	4.410	1.307	4.760	1.116
4.370	1.546	4.730	1.348	5.080	1.152
4.690	1.586	5.050	1.388	5.400	1.187
5.000	1.627	5.370	1.426	5.730	1.220
5.320	1.665	5.690	1.463	6.050	1.253
5.640	1.703	6.020	1.497	6.380	1.285
5.960	1.738	6.340	1.531	6.710	1.316
6.280	1.772	6.670	1.563	7.040	1.344
6.600	1.804	6.990	1.594	7.380	1.374
6.920	1.836	7.320	1.624	7.710	1.401
7.250	1.866	7.650	1.653	8.040	1.426
7.570	1.895	7.980	1.681	8.370	1.454
7.900	1.923	8.310	1.708	8.710	1.478
8.220	1.952	8.640	1.734	9.040	1.504
8.550	1.974	8.970	1.758		

8.880 9.210	1.999 2.025	9.300	1.785	

Table B.0.12 Experimental Adsorption Isotherm for O_2 on zeolite 13X

T=293K		T=308K		T=323K	
P (bar)	**q_{exp} (mol.kg^{-1})**	**P (bar)**	**q_{exp} (mol.kg^{-1})**	**P (bar)**	**q_{exp} (mol.kg^{-1})**
0.000	0.000	0.000	0.000	0.000	0.000
0.132	0.017	0.137	0.014	0.133	0.011
0.254	0.032	0.264	0.027	0.256	0.021
0.377	0.047	0.387	0.039	0.378	0.032
0.495	0.061	0.509	0.051	0.499	0.041
0.609	0.075	0.628	0.063	0.618	0.051
0.724	0.089	0.746	0.075	0.732	0.061
0.833	0.103	0.859	0.086	0.848	0.070
0.934	0.115	0.962	0.097	0.953	0.078
1.020	0.126	1.010	0.102	1.000	0.081
1.310	0.161	1.310	0.132	1.310	0.107
1.600	0.196	1.620	0.161	1.620	0.132
1.890	0.231	1.920	0.190	1.930	0.156
2.180	0.265	2.220	0.219	2.250	0.180
2.480	0.299	2.520	0.248	2.560	0.205
2.770	0.333	2.830	0.276	2.870	0.229
3.060	0.366	3.130	0.304	3.190	0.253
3.360	0.399	3.440	0.332	3.500	0.277
3.650	0.432	3.740	0.360	3.810	0.301
3.950	0.463	4.040	0.388	4.130	0.324
4.540	0.527	4.660	0.441	4.760	0.370
4.840	0.559	4.970	0.467	5.070	0.394
5.130	0.590	5.270	0.495	5.390	0.416
5.430	0.620	5.580	0.521	5.710	0.439
5.730	0.651	5.890	0.547	6.030	0.462
6.030	0.680	6.200	0.573	6.340	0.484
6.330	0.711	6.510	0.599	6.660	0.506
6.630	0.740	6.820	0.625	6.980	0.527
6.930	0.769	7.130	0.650	7.290	0.549
7.230	0.798	7.440	0.675	7.610	0.570
7.540	0.826	7.750	0.699	7.930	0.591
7.840	0.855	8.060	0.724	8.250	0.612
8.140	0.882	8.370	0.748	8.560	0.632
8.450	0.910	8.680	0.772	8.880	0.652
8.750	0.938	8.990	0.795	9.200	0.672
9.050	0.964	9.300	0.819	9.520	0.692
9.360	0.990	9.620	0.842	9.840	0.713
9.660	1.016	9.930	0.866	10.150	0.732
9.970	1.042				

References

[1] T. W. Kienlen, *The Future of Coal*, vol. 10, no. 4. 2007.

[2] IEA, "Key World Energy Statistics 2009," *Statistics (Ber).*, p. 82, 2009.

[3] B. R. Singh and O. Singh, "Global Trends of Fossil Fuel Reserves and Climate Change in the 21st Century," *Foss. Fuel Environ.*, pp. 167–192, 2012.

[4] J. M. Bermudez, A. Arenillas, R. Luque, and J. A. Menendez, "An overview of novel technologies to valorise coke oven gas surplus," *Fuel Process. Technol.*, 2013.

[5] G. . Austin, "Shreve's Chemical Process Industries," 1984.

[6] R. Razzaq, C. Li, and S. Zhang, "Coke oven gas: Availability, properties, purification, and utilization in China," *Fuel*, vol. 113, pp. 287–299, 2013.

[7] A. Products, "New-Methods-for-Hydrogen-Purity-Analysis.Pdf," no. January, pp. 3–4, 2011.

[8] Y. P. Z. Oliver, "Comparison of finite difference and finite volume methods Development of an educational tool for the Fixed - bed gas adsorption problem," 2011.

[9] Linde, "Hydrogen Recovery by Pressure Swing Adsorption," *Engineering*, pp. 4–8, 2010.

[10] C. a. Grande, "Advances in Pressure Swing Adsorption for Gas Separation," *ISRN Chem. Eng.*, vol. 2012, pp. 1–13, 2012.

[11] T. Lipman, "An Overview of Hydrogen Production and Storage Systems with Renewable Hydrogen Case Studies," *Clean Energy States Alliance*, p. 32, 2011.

[12] J. A. Delgado, V. I. Águeda, M. A. Uguina, J. L. Sotelo, P. Brea, and C. A. Grande, "Adsorption and Diffusion of H 2 , CO, CH 4 , and CO 2 in BPL Activated Carbon and 13X Zeolite: Evaluation of Performance in Pressure Swing Adsorption Hydrogen Purification by Simulation," *Ind. Eng. Chem. Res.*, vol. 53, no. 40, pp. 15414–15426, 2014.

[13] K. Wright, "Coke Oven Gas Treatment," *Most*, pp. 221–257, 2001.

[14] R. Yang, *Gas Separation by Adsorption Processes*, vol. 2. 1988.

[15] Y. Park, D. K. Moon, Y. H. Kim, H. Ahn, and C. H. Lee, "Adsorption isotherms of CO2, CO, N2, CH4, Ar and H2 on activated carbon and zeolite LiX up to 1.0 MPa," *Adsorption*, vol. 20, no. 4, pp. 631–647, 2014.

[16] G. Narin, V. F. D. Martins, M. Campo, A. M. Ribeiro, A. Ferreira, J. C. Santos, K. Schumann, and A. E. Rodrigues, "Light olefins/paraffins separation with 13X zeolite binderless beads," *Sep. Purif. Technol.*, vol. 133, pp. 452–475, 2014.

[17] T. Y. Zakharian and S. R. Coon, "Evaluation of Spartan semi-empirical molecular modeling software for calculations of molecules on surfaces: CO adsorption on Ni(111)," *Comput. Chem.*, vol. 25, no. 2, pp. 135–144, 2001.

[18] "Spartan 14 (product of Wavefunction Inc, Irvine, CA; www.wavefun.com)." .

[19] W. Hehre, A. J. Shusterman, and J. E. Nelson, “The Molecular Modeling Workbook For Organic Chemistry.” p. 310, 1998.

[20] Ralph T. Yang, *Adsorbents: Fundamentals and applications*. 1993.

[21] Z. Al-Qodah and R. Shawabkah, “Production and characterization of granular activated carbon from activated sludge,” *Brazilian J. Chem. Eng.*, vol. 26, no. 1, pp. 127–136, 2009.

[22] C. T. Campbell and J. R. V Sellers, “The entropies of adsorbed molecules,” *J. Am. Chem. Soc.*, vol. 134, no. 43, pp. 18109–18115, 2012.

[23] H. Sellers and J. Gislason, “Adsorption and desorption rate constants for small molecules on metal surfaces: An example of Trouton’s rule,” *Surf. Sci.*, vol. 426, no. 2, pp. 147–153, 1999.

[24] C. Baerlocher, L. McCusker, and D. Olson, *Atlas of zeolite framework types*, vol. 12. 2007.

[25] J. C. Jansen, M. Stocker, H. G. Karge, and J. Weitkamp, *Advanced Zeolite Science and Applications*, vol. 85. 1994.

[26] M. C. Georgiadis, J. R. Banga, and E. N. Pistikopoulos, *Process Systems Engineering*. .

[27] M. B. Donald, *Introduction to Chemical Engineering.*, vol. 6, no. 4–5. 1957.

[28] Y. J. Kim, Y. S. Nam, and Y. T. Kang, “Study on a numerical model and PSA (pressure swing adsorption) process experiment for CH4/CO2 separation from biogas,” *Energy*, vol. 91, pp. 732–741, 2015.

[29] D. Nikolic, A. Giovanoglou, M. C. Georgiadis, and E. S. Kikkinides, “Generic Modeling Framework for Gas Separations Using Multibed Pressure Swing Adsorption Processes,” *Ind. Eng. Chem. Res.*, vol. 47, no. 9, pp. 3156–3169, 2008.

[30] R. Haghpanah, A. Majumder, R. Nilam, A. Rajendran, S. Farooq, I. a Karimi, and M. Amanullah, “Multi-objective Optimization of a 4-step Adsorption Process for Post-combustion CO2 Capture Using Finite Volume Technique,” *Ind. Eng. Chem. Res.*, 2013.

[31] D. D. Do, *Adsorption Analysis: Equilibria and Kinetics*, vol. 2, no. Imperial College Press. 1998.

[32] B. E. Poling, M. Prausnitz, and J. P. O’Connell, “The Properties of Gases and Liquids,” *Library (Lond).*, vol. 23, no. 3, pp. 1–11, 2006.

[33] L. I. Berger, M. Frenkel, C. A. Koh, P. E. Bradley, J. R. Fuhr, W. H. Koppenol, and T. J. Bruno, *Handbook of chemistry and physics*. 2014.

[34] T. M. Alsoudani, “DISCONTINUITIES IN MATHEMATICAL MODELLING : ORIGIN , DETECTION AND RESOLUTION,” no. March, 2016.

[35] L. Lin, “Numerical Simulation Of Pressure Swing Adsorption Process,” no. August, 1997.

[36] P. Biswas, S. Agrawal, and S. Sinha, “Modeling and Simulation for Pressure Swing Adsorption System for Hydrogen Purification,” *Chem. Biochem. Eng. Q.*, vol. 24, no. 4, pp. 409–414, 2010.

[37] S. Cavenati, C. Grande, and A. Rodrigues, “Layered Pressure Swing Adsorption for

Methane Recovery from CH4/CO2/N2 Streams," *Adsorption*, vol. 11, no. 1, pp. 549–554, 2005.

[38] K. Warmuziński and M. Tańczyk, "Multicomponent pressure swing adsorption Part I. Modelling of large-scale PSA installations," *Chem. Eng. Process. Process Intensif.*, vol. 36, no. 2, pp. 89–99, 1997.

[39] J.-G. Jee, M.-B. Kim, and C.-H. Lee, "Adsorption Characteristics of Hydrogen Mixtures in a Layered Bed: Binary, Ternary, and Five-Component Mixtures," *Ind. Eng. Chem. Res.*, vol. 40, pp. 868–878, 2001.

[40] J. Yang and C. Lee, "Adsorption dynamics of a layered bed PSA for H2 recovery from coke oven gas," *AIChE J.*, vol. 44, no. 6, pp. 1325–1334, 1998.

[41] C. R. S. Franco, "Pressure Swing Adsorption for the Purification of Hydrogen," p. 94, 2014.

[42] R. S. Todd, J. He, P. a. Webley, C. Beh, S. Wilson, and M. a. Lloyd, "Fast Finite-Volume Method for PSA/VSA Cycle Simulation - Experimental Validation," *Ind. Eng. Chem. Res.*, vol. 40, no. 14, pp. 3217–3224, 2001.

[43] S. Jain, A. S. Moharir, P. Li, and G. Wozny, "Heuristic design of pressure swing adsorption: A preliminary study," *Sep. Purif. Technol.*, vol. 33, no. 1, pp. 25–43, 2003.

[44] D. Ruthven, S. Farooq, and K. Knaebel, "Pressure Swing Adsorption." p. 352, 1993.

[45] D. M. Ruthven, "Principles of Adsorption and Adsorption processes." .

[46] "Caldic." [Online]. Available: http://www.caldic.com/en/contact.

[47] J. Van der Veen, "Coke oven gas as source for hydrogen production," p. 52, 2013.

[48] National Hydrogen Association, "Hydrogen and fuel cells The U. S. Market Report," 2010.

[49] W. J. Hehre, *A Guide to Molecular Mechanics and Quantum Chemical Calculations*. 2003.

[50] "Mercury (CSD product) http://www.ccdc.cam.ac.uk/solutions/csd-system/components/mercury/." .